UNIVERSITY
OF TRENTO - Italy

Doctoral School in Materials Science and Engineering – XXV cycle

Structural Defects in Nanotechnology
Production – Characterisation – Applications

"Transport Properties in Mechanically Ground Nanocrystalline Ceramics & Hydrogen Storage in Metallic Hydrides"

Mahmoud Abdellatief

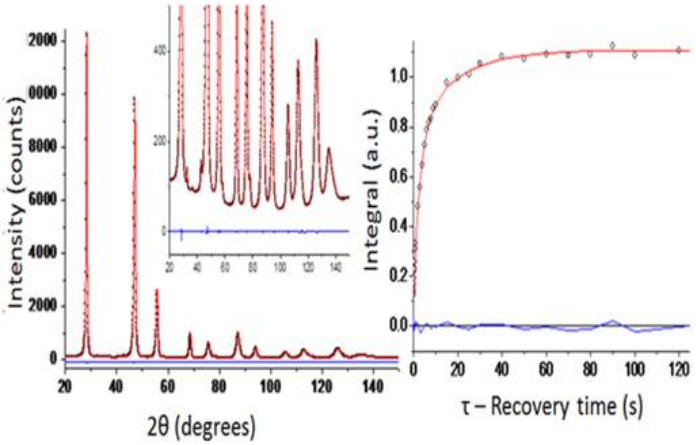

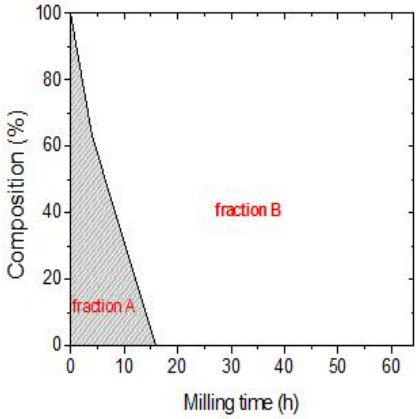

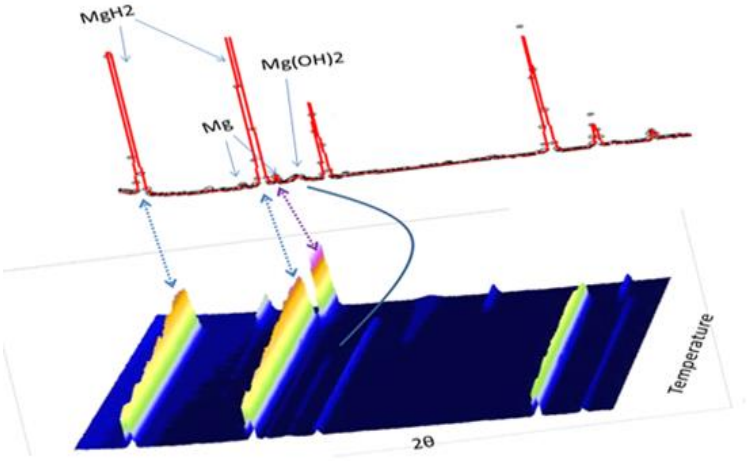

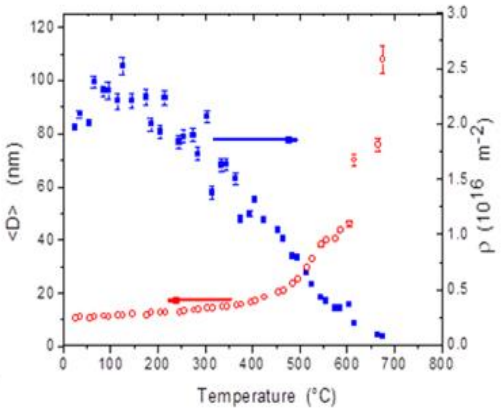

April 2013

Structural Defects in Nanotechnology
Production – Characterisation – Applications

"Transport Properties in Mechanically Ground Nanocrystalline Ceramics & Hydrogen Storage in Metallic Hydrides"

Mahmoud Abdellatief

Approved by:
Professor Paolo Scardi, Advisor
Department of Civil, Environmental and Mechanical Engineering
University of Trento, Italy

Doctor Andrea Lausi
MCX beamline – Sincrotrone di Trieste (ELETTRA)
AREA Science Park, Basovizza, Trieste Italy

Doctor Jasper Rikkert Plaisier
MCX beamline – Sincrotrone di Trieste (ELETTRA)
AREA Science Park, Basovizza, Trieste Italy

University of Trento,
April 2013

Dedicated to Prof. Klaus Müller

"Quantum physics thus reveals a basic oneness of the universe"

Erwin Schrodinger

Acknowledgments

Firstly, I would like to give my sincere appreciations and thanks to Prof. Klaus Muller who suddenly passed away on April the 1st 2011. I could work under his supervision for only one year in which I could appreciate his help and kind personality, while he strongly contributed to the early stages of this work. Truly, I can still feel his inspirations around me.

I would like also to express my deep gratitude and appreciations to Prof. Paolo Scardi for all his support and help in all stages of my PhD. Although I spent two years of my PhD at the synchrotron ELETTRA in Trieste, he was always close to me especially in most difficult times of the thesis work. Actually, I am proud to be one of his students.

More thanks and friendships go to Prof. Matteo Leoni, whose sincere efforts coupled with his patience. Thank you very much Matteo, I am grateful for all your assistance.

I also wish to acknowledge Sincrotrone Trieste for the financial support to my PhD. Special thanks go to Doctor Andrea Lausi for his quiet supervision and his kind and appreciated hospitality during my stay in Trieste at MCX beamline (ELETTRA). My deep thanks also go to Doctor Jasper Plaisier for his friendship and assistance during my presence at ELETTRA.

I would like to kindly acknowledge Prof. Renzo Campostrini, as I enjoyed a lot collaborating with him for part of the thesis work. Thanks prof. Campostrini and I wish you all happiness.

Special thanks go to Dr. Mirco D'Incau for his assistance and teaching activity in passing me his experimental experience. Mirco is one who is always willing to help, thank you very much Mirco.

I would like to thank Matthias Abele for his collaboration and friendship. I enjoyed the work with him, and I wish full success in his career and happiness for his new little family.

Of course I cannot forget the honest and grateful technical help provided by Mr Giulio Zerauschek. He is a technician with amazing skills, always assisting in very expert way.

My deep thanks go to the Canadian scientist Jennifer Macleod for her hard work with the oven program.

My respect and appreciation goes to Prof. Karimat El-Sayed for her precious support to face and accept the challenges before and during my stay in Italy.

I would like to acknowledge the support and the very kind assistance of prof. A. Benedetti and prof. P. Riello from Venice University.

In addition to the previous acknowledgments, I would like to thank all my colleagues in Trento, Cristy L. Azanza Ricardo, M. Muller, L. Gelisio, A. Leonardo, K. Beyerlein, M. Ortolani and in Trieste X. Santarelli.

I am deeply and forever indebted to my parents for their encouragement, love and trust throughout my entire life. I could not achieve any success in my entire life without their support. I am also very grateful to my only sister Shimaa.

Finally, my heartfelt love goes to my wife Maha for her fresh feelings that always excite my curiosity and to my lovely daughter Mayar who put me in strong and nice emotions.

Contents

CHAPTER I

Introduction

Structural defects play a major role in nanotechnology as they influence most properties, thus largely motivating the special interest in studying materials at the nano scale. The present Thesis work contributes to this broad and diversified research field with emphasis on the characterization of nanocrystalline ceramic materials and their lattice defects. In particular, main efforts were addressed to develop new and more comprehensive approaches to the study of nanocrystalline powders, combining different techniques for a better and deeper understanding of materials.

The specific applications selected in this work are basically two: nanocrystalline fluorite as a promising ionic conductor and nanocrystalline magnesium hydride for hydrogen storage applications. Chapters II and III were dedicated to investigate nanocrystalline fluorite produced by two different methods: a bottom-up approach based on co-precipitation of Ca and F precursors yielding loosely bound nanocrystals, and a popular top-down approach, high energy ball milling, giving nanocrystals of comparable sizes but strongly agglomerated and densely populated with dislocations. As a major achievement reported in this part of the Thesis work, a new approach was proposed and tested for the simultaneous modelling of X-ray Diffraction (XRD) peak profiles and solid state NMR spin-lattice relaxation data. With the valuable support of Transmission Electron Microscopy (TEM), this work offers a new understanding of the complex defect structure of nanocrystalline fluorite, and is also a demonstration of the power of combining different techniques in a consistent way.

One of the most debated aspects of nanotechnology concerns the stability of the nanostructure, and the mechanisms of defect annealing and grain growth with temperature. This topic was the object of chapter V, dedicated to study the influence of lattice defects on the grain growth kinetics of nanocrystalline fluorite. This chapter was preceded by chapter IV, on the furnace recently installed at the MCX beamline for in-situ high temperature fast data collection; besides providing useful details for the in-situ study on nanocrystalline fluorite shown in the following chapter, the activity reported in chapter IV is a tangible sign of the special involvement during the Thesis work in supporting standard operation as well as development of the ELETTRA beamline MCX. The growth kinetics was studied on two samples, among those discussed in Chapter III, with comparable crystalline domain size but drastically different lattice defect content, so to highlight the role lattice defects – dislocations in this case – in the growth process.

Last two chapters (chapter VI and VII) were dedicated to nanocrystalline magnesium hydride, and how the performance, in particular the hydrogen desorption kinetics, can be improved by adding a nanocrystalline tin oxide. Besides general aspects on phase composition of the system and hydrogen storage capability, the work also addressed the problem of obtaining activation energy values in the thermal decomposition of magnesium hydride powders, presenting an interesting review of results given by the most known and well-assessed TG-MS coupled measurements, with details on the use of different equations of the literature on thermal analysis.

Although research work can rarely be considered as finished, a sound conclusion of this Thesis work is toward the use of different characterization techniques, also within the same data analysis procedure, to support a better, and more reliable investigation of nanomaterial properties.

CHAPTER II

Solid State NMR and XRD Line Profile Analysis of Heavily Deformed Fluorite

M. Abdellatief , M. Abele, M. Leoni and P. Scardi

Part of this chapter has been published in:

Journal of Thin Solid Films, Volume 530, 2013, Pages 44-48

Abstract

The effect of high-energy ball milling on calcium fluoride was studied by X-ray Diffraction (XRD) Line Profile Analysis (LPA) and Solid State NMR spin-lattice relaxation. The latter technique is especially useful to detect the non-homogeneous effects of the early stages of mechanical grinding, but is also sensitive to the defect structure of the ball milled powders. When supported by Solid State NMR, XRD LPA unveils fine details of the milling effects on fluorite, in terms of increasing dislocation density and progressive refinement of the crystalline size down to the nanoscale.

2.1 Introduction

Fluorine based materials attract an increasing interest for their transport properties and stability. Specific fields of application concern energy conversion, as electrolytes for fuel cells, transparent electrodes for solar cells, and electrodes for aqueous batteries, in particular lithium batteries **(Amatucci & Pereira, 2007)**. Advanced fluorides are used in systems for clean energy storage, such as secondary ion batteries and fuel cells, as well as in chemical sensors **(Ruprecht, Wilkening, Feldhoff, Steuernagel, & Heitjans, 2009) (Chandra, 1981) (Niklasson & Granqvist, 2007)**. As a further promising area of development, nanostructured ionic materials **(Ruprecht, Wilkening, Feldhoff, Steuernagel, & Heitjans, 2009) (Heitjans & Indris, 2003) (Gleiter, 1989) (Siegel, Trigg, Immergut, & Vera, 1994) (Puina, Ramlau, Heitjans, & Maier, 2000)**are increasingly studied as new catalysts **(Ying & Sun, 1997)**. Energy storage of ionic conductors mainly depends on their ionic conductivity, which in turn is closely related to their microstructure: lattice defects have a direct influence, like vacancies as point defects in which ions can migrate, but line defects (dislocations) and planar defects (stacking faults, interfaces and grains boundaries) can also play an important role.

In this paper we study CaF_2 as an example of a typical ionic conductor with a simple and stable (fcc) crystal structure. High energy ball milling was used to prepare a series of CaF_2 powder samples with different types and content of lattice defects. The effects of the milling process were studied by X-Ray Diffraction (XRD) Line Profile Analysis (LPA) and by Solid state NMR spin lattice relaxation.

XRD-LPA, especially when supported by an advanced data analysis like Whole Powder Pattern Modelling (WPPM) **(Scardi & Leoni, 2002) (Scardi & Leoni, Diffraction Analysis of the Microstructure of Materials, 2004)**, can provide detailed information on the crystalline domain shape and size distribution and on the density of planar faults and dislocations. The latter, in particular, seem to be the most abundant lattice defects introduced by the ball milling of fluorite **(Giudici, Biddau, D'Incau, Leoni, & Scardi, 2005)**. Although other techniques like X-ray Topography and Transmission Electron Microscopy (TEM) **(Hull & Bacon, 1984) (Garcia, Leoni, & Scardi, 2009)** can be used to study dislocations, little or no quantitative evaluations can be made for the high density of defects caused by ball milling. Therefore, even if high resolution TEM pictures can show direct evidence of the extensive presence of dislocations in ball milled fluorite **(Giudici, Biddau, D'Incau, Leoni, & Scardi, 2005)**, quantification usually involves XRD-LPA methods **(Fiala & Snyder, 1999) (Klug & Alexander, 1974)**, which can be effective even for

dislocation densities as high as 10^{16}-10^{17} m^{-2} **(Garcia, Leoni, & Scardi, 2009)** **(Fiala & Snyder, 1999)**.

Even if XRD-LPA can be a valuable tool to study line defects, it gives an average density weighted over the dislocations population **(Scardi & Leoni, Diffraction Analysis of the Microstructure of Materials, 2004)**, and is inherently not too sensitive to the inhomogeneity that might come from the preparation procedure. Such effects and the non-uniformity of the ball milling process (as well as many other plastic deformation methods) require a complementary technique to make complete sense of the XRD-LPA results.

Solid state NMR is known for its sensitivity to the local electronic structure. The latter is connected to the local atomic coordination and bonding angles, which in turn is strongly affected by the presence of dislocations **(Eckert H. , 1996)**. Several examples can be found in literature, where the NMR spectroscopy was used to investigate structural defects and F^--mobility in different fluorides **(Ruprecht, Wilkening, Steuernagel, & Heitjans, 2008)** **(Jain P. , Kim, Youngman, & Sen, 2010)**. In the case of lithium containing ceramics ^7Li relaxometry proved to be a versatile tool to distinguish phases in heterogeneously structured nanocrystalline materials **(Heitjans & Wilkening, 2002)** **(Indris & Heitjans, 2002)**. As shown by our work, quite interesting correlations can be found between the results of XRD-LPA and Solid State NMR relaxometry. While the specific results concern ball milled fluorite, the general approach and use of these two techniques can easily extend to a much broader class of materials. An extension of this work, with finer details on the lattice defects generated by ball milling and their effect on the T_1 relaxometry are the object of the next Chapter of this Thesis.

2.2 Methodological background

The purpose of this section is to show some basic concepts the main techniques used in this and in the following chapter. More specifically, X-Ray Diffraction (XRD) methods of analysis and solid state Nuclear Magnetic Resonance (NMR).

2.2.1 Line Profile Analysis (LPA) by Whole Powder Pattern Modelling (WPPM)

Line profile analysis is a known and informative technique of crystallography **(Scardi & Leoni, 2006)** **(Vives, Gaffet, & Meunier, 2004)** **(Scardi & Leoni, 2006)**, more specifically in nanocrystalline materials where crystallite size and lattice defects have a crucial role and influence

properties and applications **(Scardi P. , Leoni, Lamas, & Cabanillas, 2005)** **(Mileva, Wilsonb, Kamali Kannangaraa, & Trana, 2008)**. Several theories and approaches are used to extract information from the line profiles, whether in the form profile width and shape or integrated intensity **(Scardi & Leoni, 2006)**. LPA is commonly used in structural refinement based on the Rietveld method **(Young, 1993)**, and Whole Powder Pattern Fitting WPPF **(Scardi, Leoni, & Dong, 2000)** is the most common approach. WPPF commonly relies on using an analytical function to perform non-linear least square fit of the diffraction profiles, from which structural and microstructural information is obtained. The best-fit parameters of WPPF then become a proxy of the real, observed experimental data: this is the main limitation (and arbitrariness) in this approach **(Scardi & Leoni, 2006)**. However, these traditional methods are quick, efficient and effective in many cases of study. The main limitation is in cases where the observed line profiles cannot be described by the analytical line profile, and forcing the interpretation based on an arbitrary (and inappropriate) line profile becomes a dangerous practice, which seriously limits the reliability of the LPA results. In recent years the Whole Powder Pattern Modeling (WPPM) **(Scardi & Leoni, 2002)** **(Scardi & Leoni, Whole Powder Pattern Modeling: theory and applications, 2004)** was introduced to reduce the arbitrariness in LPA and make it a more robust technique. The WPPM approach is based on physical models of the microstructure and effect of the most frequently occurring lattice defects. Models parameters optimized by non-linear least squares are now physical parameters with a more direct and clear meaning than the profile parameters of WPPF. **Figure 2.1** shows the basic strategy underlying the LPA-WPPM **(Scardi & Leoni, 2002)** **(Scardi & Leoni, Whole Powder Pattern Modeling: theory and applications, 2004)** approach, stressing in particular the direct optimization of parameters of physical models based on the experimental diffraction pattern.

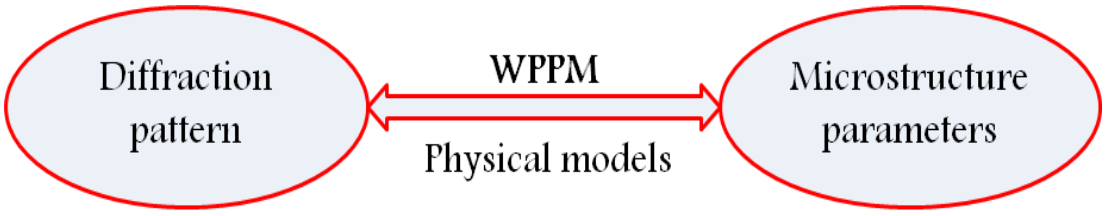

Figure 2.1 *Basic principle of the WPPM approach*

Each diffraction peak profile is considered as a convolution of microstructural contributions leading to the profile's final shape and broadening (**equation 2.1**). Then in the Fourier space, the convolution converts to a direct product which is more easily handled from the numerical point of view (**equation 2.2 and 2.3**).

$$I(s) = I^{IP}(s) \otimes I^{S}(s) \otimes I^{D}(s) \otimes I^{F} \otimes I^{APB}(s) \otimes \ldots. \quad (\mathbf{2.1})$$

where s is the reciprocal space variable, I^{IP} is the instrumental contribution, I^{S} is the crystallite size/shape contribution, I^{D} represents the lattice distortion (e.g. dislocation) contribution and I^{F} represents the contribution planar faulting. Other contributions (like Anti-Phase Boundaries, I^{APB}) can also be added by using the appropriate Fourier coefficients. The line profile can be represented as Fourier transform as

$$I(s) = k(s) \int C(L) \exp(2\pi i L s) dL \quad (\mathbf{2.2})$$

where K(s) is a group of constants and known functions of s (like Lorentz-Polarization factor), C(L) is the Fourier Transform (FT) of all broadening sources and L, the Fourier or correlation length, is the variable conjugate to s.

Some preliminary information on the sample, and possible microstructural features is therefore necessary to build model (C(L), and determine the main model parameters. For example, if the only two (main) broadening sources are crystallite size and dislocations, then C(L) can be written as **equation (2.3)**.

$$C(L) = A^{IP}(L) \,.\, A^{s}(L).\, A^{D}(L) \quad (\mathbf{2.3})$$

Equation 2.3 is the equivalent to **equation 2.1**, but in the Fourier space (**see figure 2.2**).

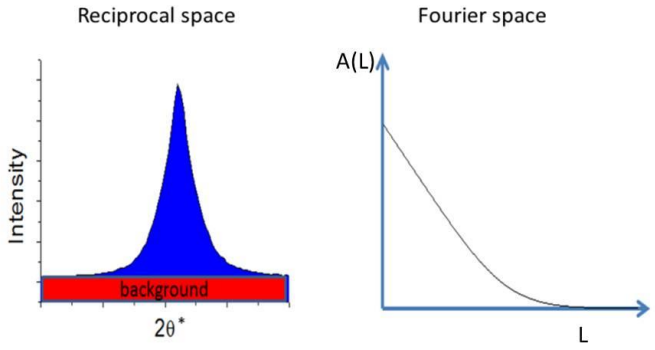

Figure 2.2 *XRD line profile in the reciprocal (left) and in Fourier space (right)*

In fact, $A^{IP}(L)$ is the Fourier transform of the instrumental profile model, $A^{s}(L)$ is FT of the finite-size crystalline domains, and $A^{D}(L)$ is the FT of the contribution of dislocations to the line

profile. PM2K **(Leoni, Confente, & Scardi, 2006)** is a software based on the WPPM approach, which allows one to create a full model of the line profiles, containing all sources of expected broadening for a specific case of study, to be used in a non-linear least square fitting procedure based on the Levenberg-Marquardt algorithm. The primary sources of broadening, in most cases, are the instrument, finite crystallite size and lattice distortions. The Instrumental component is directly related to simple expressions (in most cases, just a pseudoVoigt profile) parameterized by the so-called Caglioti's function, which accounts the full width at half maximum and the asymmetry of the instrumental profile using a standard material. The crystallite size/shape can be modelled in PM2K **(Leoni, Confente, & Scardi, 2006)** using several distribution functions, as lognormal and gamma, and when data quality is sufficiently high, by a free histogram. Also multimodal distribution can be considered. In case of a lognormal distribution function, the two refinable parameters are μ and σ, respectively lognormal mean and variance.

Dislocations, as a common defect resulted from grinding, can also be modelled based on the knowledge of the elastic properties (elastic tensor components) and geometrical features of the lattice defect, i.e., the main slip system(s) for the specific material. It is also possible to distinguish the character of the dislocation, typically in terms of edge and screw type. The specificity of the dislocation line broadening effect, and in particular the anisotropic (hkl-dependent) line broadening, are summarized in the so-called average contrast factor, which can be calculated once the above described information is known and used in the PM2K software **(Leoni, Confente, & Scardi, 2006)**. The contrast factor for dislocations in fluorite is well known from previous studies **(Muñoz, Rodriguez, & Castaing, 1994)**.

A selected example of PM2K result can be seen in the following figure for nanocrystalline ground CaF_2, starting from the initial model (**figure 2.3**) and the last refined model (**figure 2.4a)** when model's free parameters converge (**figure 2.4b)**. The main refined parameters were a Chebychev polynomial function for the background, μ and σ for the size distribution with a spherical shape assumption, average dislocation density (ρ), effective outer cut-off radius (R_e), and the unit cell parameter (a_o).

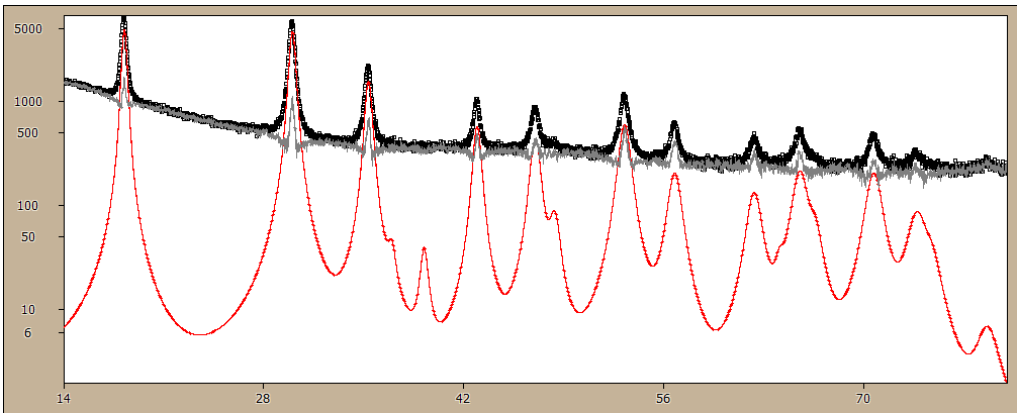

Figure 2.3 *The starting model for a ground CaF_2 sample*

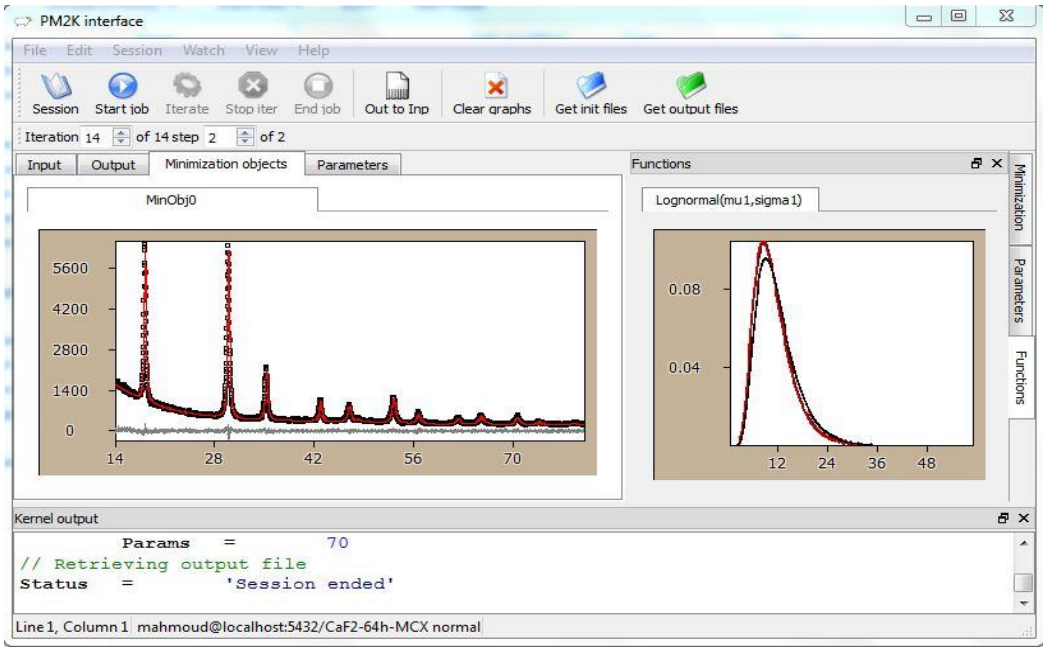

(a)

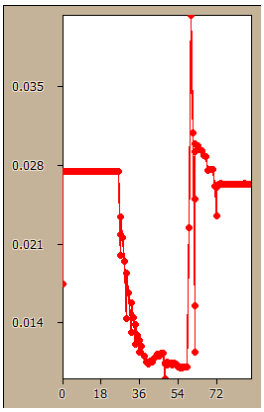

(b)

Figure 2.4 ***a)*** *The final model after refinement shows a good matching between model and pattern. The lognormal distribution on the right refers to the size (diameter) distribution.* ***b)*** *The convergence of the mean dislocation density parameters (in units of 10^{18} m^{-2})*

2.2.2 Solid State Nuclear Magnetic Resonance (NMR) Relaxometry

Nuclear Magnetic Resonance (NMR) is one of the major and effective techniques used in materials science to investigate crystal structure and lattice dynamics. The main principle of NMR spectroscopy is investigating the response of active atomic nuclei under magnetic field. All materials consist of atoms arranged in a specific environment, and each atom, in turn, consists of electrons, protons and neutrons, each one with a given spin. When atoms have non-zero spin quantum number I, they are NMR active nuclei as they are influenced by an external magnetic field. The values of the spin quantum number can be predicted based on the knowledge of the protons and neutrons' numbers inside the nucleus as tabulated in **table 2.1**.

Table 2.1 *The number of protons and neutrons in the nucleus vs. the spin quantum number I*

Number of protons	**Number of neutrons**	**I**
Even	Even	0
Odd	Odd	1 or 2 or 3 or …
Even	Odd	$\frac{1}{2}$ or $\frac{3}{2}$ or $\frac{5}{2}$ or …
Odd	Even	$\frac{1}{2}$ or $\frac{3}{2}$ or $\frac{5}{2}$ or …

Any nucleus with non-zero spin quantum number I can be represented as a bar magnet having a magnetic moment μ. When no external magnetic field is applied to the nuclei system, all atoms align randomly, producing null net magnetization; when an external magnetic field $\mathbf{B_o}$ is applied, then the nuclei turn to a specific alignment, thus causing a raise in the net magnetization along $\mathbf{B_o}$ (**Figure 2.5**).

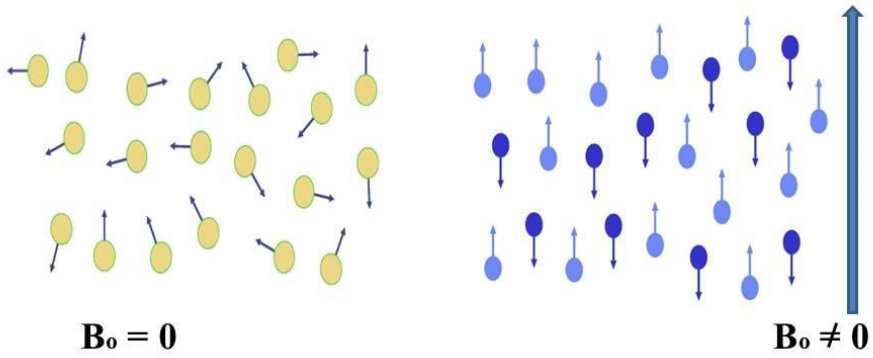

Figure 2.5 *Magnetic spin arrangement with and without external magnetic field*

As shown in **figure 2.5** when Bo is not zero, some of the nuclear magnetic moments align with the external field while others align against the external field. This can be explained by quantum mechanics in terms of magnetic energy levels under the applied field Bo, with the specific law that the number of energy levels is related to the I value and equals (2I+1). For example, if we have a spin system with I=½, then there is only one additional energy level that can be formed, and this means that only one energy transition is allowed (**figure 2.6**). From the energy point of view, the lowest energy level with spin quantum number m=½ is more preferred, and corresponds to magnetic moments aligned along the external filed. The magnetic moments in the higher energy level with m=-½ are aligned antiparallel to the external field.

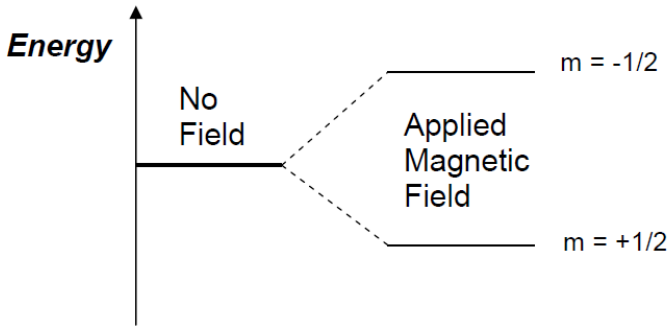

[1]**Figure 2.6** *Splitting in the magnetic spin energy state under external magnetic field*

The axis of rotation of a spinning nucleus under the influence of external magnetic field is not exactly along or against the direction of $\mathbf{B_o}$ but there is an angle between them (**figure 2.7**). The angular velocity depends on the strength of $\mathbf{B_o}$ and also on a constant called gyromagnetic ratio γ which is an intrinsic property for each nucleus (**equation 2.4**). This angular velocity of the spinning is also called Larmor frequency ω_L and in some cases denoted by ω_o and called the resonance frequency.

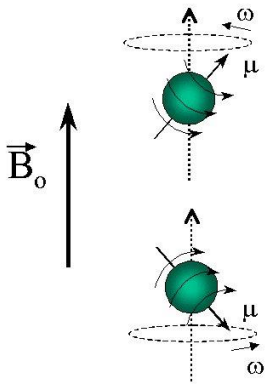

Figure 2.7 *Schematic representation of nucleus spin under magnetic field application*

[1] Figure reference: "http://www.process-nmr.com/nmr1.htm" website

$$\omega_o = \gamma B_o \quad \textbf{(2.4)}$$

where ω_o is the angular frequency, γ is the gyromagnetic ratio and $\mathbf{B_o}$ is the external magnetic field strength. The gyromagnetic ratio is a constant for each nucleus calculated from the ratio between the nuclear angular momentum and the magnetic moment according to **equation 2.5.**

$$\gamma = \frac{\boldsymbol{2\pi}\,\mu}{\boldsymbol{h\,I}} \quad \textbf{(2.5)}$$

where μ is the magnetic moment, h is Planck's constant (h = 6.6261 x 10^{-34} J.Sec) and I is the magnetic quantum number.

2.2.2.1 The resonance mechanisms

The resonance in the NMR experiment occurs when the frequency of the applied wave equals the frequency of transition between two energy states or what is known as Larmor frequency. The frequency of the applied wave in solid state NMR experiments lies in the radio frequency (rf) range. The resonance experiment is shown graphically in **figure 2.8** as made of three different stages as follows:

Stage I: more spins accommodate on the lowest energy state while less spins accommodate on the higher energy level. The magnetic system is only under the influence of the external magnetic field and no rf wave is applied yet, so there is a net magnetization along the external magnetic field.

Stage II: rf wave is switched on to the magnetic system and as consequence of that, some of the spins absorb rf energy and jump to the higher energy level; thus the net magnetization along the applied magnetic field tend to be zero.

Stage III: relaxation occurs in the spins system when the rf wave is switched off and so situation returns back to stage I. The relaxation process actually takes place in a certain time to reach the equilibrium state and this time can be obtained from the recovery signal of the magnetization along the external field.

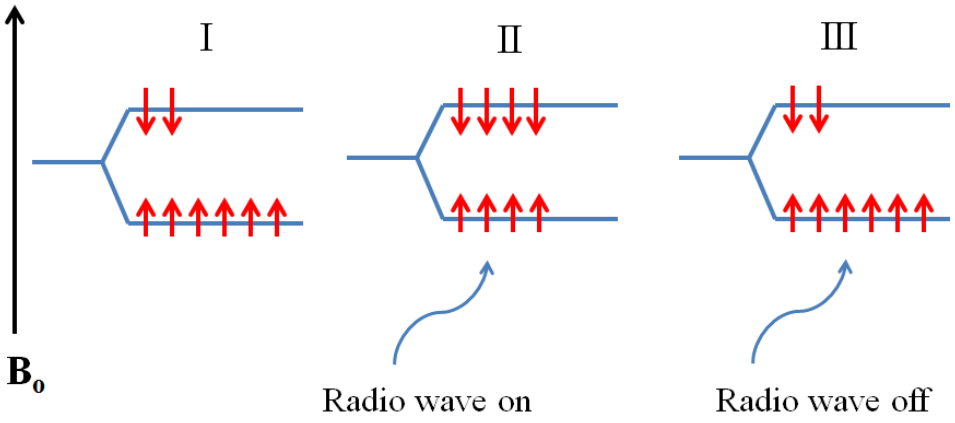

Figure 2.8 *Steps of spins transition during the NMR experiment*

There are two mechanisms of relaxations called longitudinal and transverse relaxation:

1. Longitudinal relaxation

This process of relaxation is coupled with a release of a certain amount of energy from the spin transition; this amount of energy is absorbed by the surrounding environment, which in the general meaning is called "lattice". This process is characterized by a time constant that measures the magnetization recovery process, called the spin lattice relaxation time, T_1, also called the longitudinal relaxation time. Main factors influencing the longitudinal relaxation are temperature and structural features.

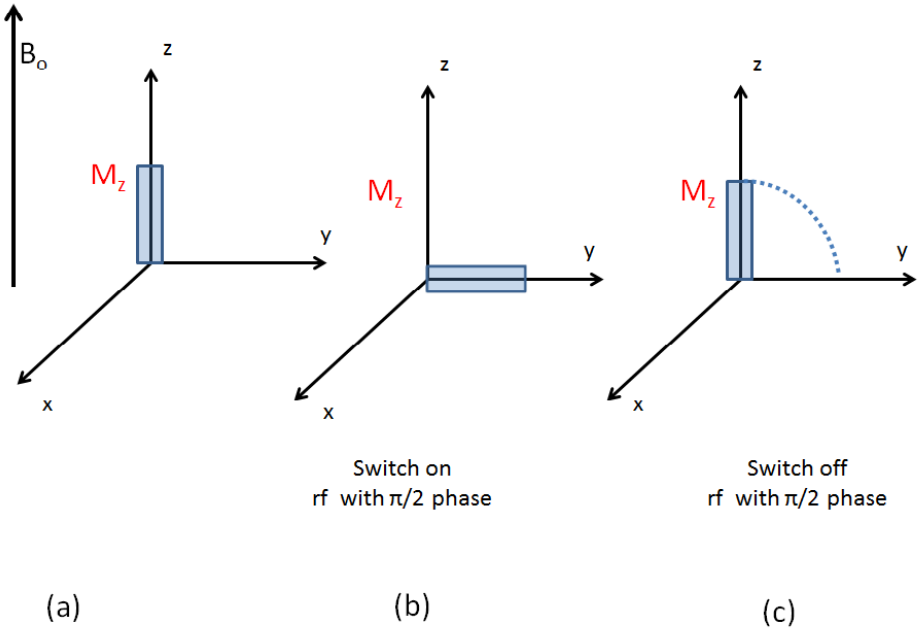

Figure 2.9 *The influence of an rf pulse on the M_z when it is switched on and off*

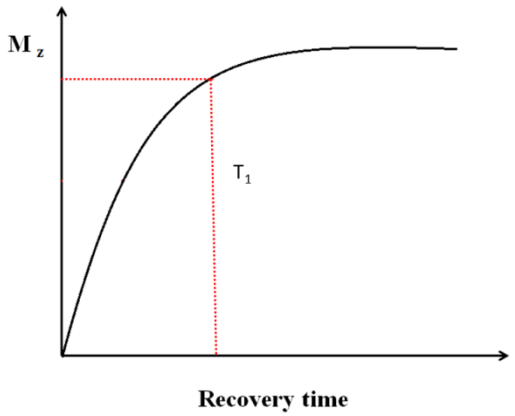

Figure 2.10 *The relaxation signal of Mz component*

Figure 2.9 shows a schematic representation for the NMR longitudinal relaxation sequences. When the rf wave B_1 with $\pi/2$ phase difference is applied to the magnetic spin system, the magnetization M_z along Z axis decays to zero since M_z is directly proportional to the difference between the number of spins in the two energy states. Switching off the rf pulse allows to recover M_z exponentially as shown in **figure 2.10**, satisfying **equation 2.6**.

$$M_z = M_o\,(1- e^{-\tau/T_1}) \qquad (\mathbf{2.6})$$

where M_o is the equilibrium magnetization. The shorter T_1 the faster lattice absorption of the spins transition energy and vice versa. As it was mentioned, the driving force of relaxation is the temperature factor or, in other terms, there is a correlation between the lattice thermal vibrational frequency and the nuclei spin frequency. The range of T_1 directly depends on the thermal properties of the lattice, even if such relation is not a simple one: as there is not a single thermal or vibrational frequency for all atoms, but actually there is a range of frequencies, only a limited number of atoms in the lattice play a role in the T_1 relaxation when they oscillate with a frequency equal of close to the Larmor frequency. Due to this fact, another parameter called the correlation time $\boldsymbol{\tau_C}$ can be defined to represent a quantitative measure of the molecular motion. Strictly speaking the molecular motion (translational and rotational) term is more appropriate in case of liquids, when molecules have a high degree of freedom in comparison with solids. Both T_1 and T_2 strongly depends on $\boldsymbol{\tau_C}$ as graphically shown in **figure 2.11,** moreover $\boldsymbol{\tau_C}$ has a wide range of values based on the material state, whether it is liquid or solid, and of course on the structural features. $\boldsymbol{\tau_C}$ is also an important factor in solids, as it is directly connected to ionic diffusions and dynamic properties more specifically used for ionic conductors and in solid electrolyte investigations.

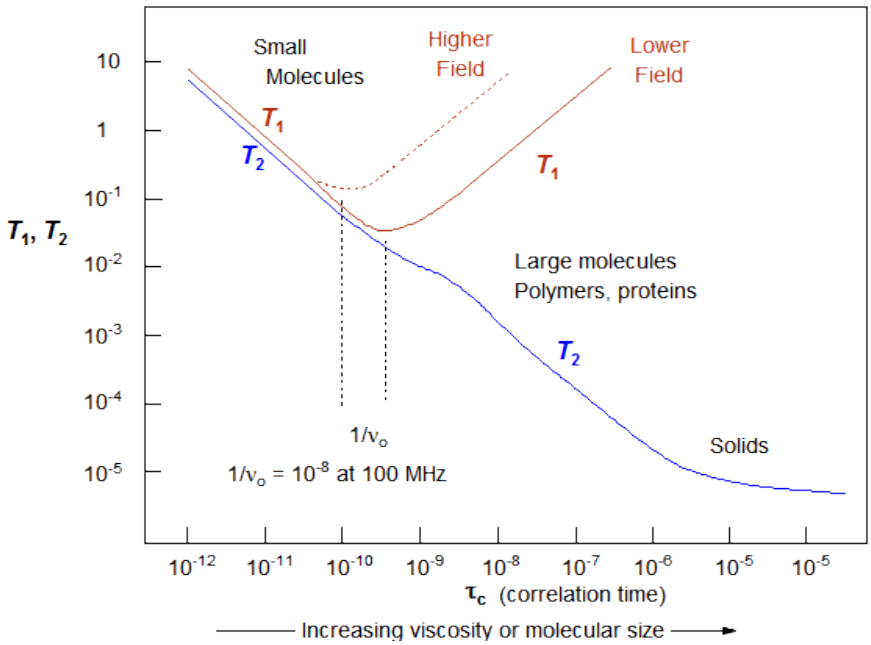

[2]***Figure 2.11*** *Correlation time dependence on molecular size*

2. Transverse relaxation

This relaxation process is related to energy exchange between spins, with no direct involvement of the lattice; it is an expression of the loss of phase coherence along the transverse magnetization M_x and M_y after the rf pulse is applied. The time characterizing this process of losing the phase among spins when rf is switched off is called spin-spin relaxation time, T_2, and it can be obtained from the full width at half maximum of the NMR spectrum (**figure 2.12**). The equations of magnetization rate in the x-y directions are:

$$\frac{dM_x}{dt} = -\frac{M_x}{T_2} \tag{2.7}$$

$$\frac{dM_y}{dt} = -\frac{M_y}{T_2} \tag{2.8}$$

[2] Figure reference: "http://www.chem.wisc.edu/areas/reich/nmr/08-tech-01-relax.htm" website

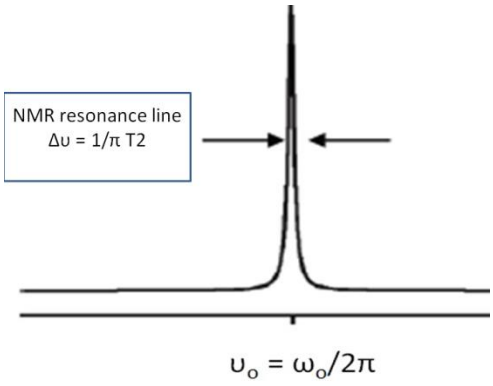

Figure 2.12 *Typical resonance line in NMR experiments*

2.2.2.2 NMR spectrometer

The NMR spectrometer (**figure 2.13**) has the following experimental components:

Magnet: is the source of the static magnetic field Bo on the sample which is the first step to perform NMR experiement.

Radio frequancy transmitter: is the source of applied radio frequancy pulse with Larmor frequancy.

Radio frequancy reciever: used to receive the radio frequancy signals when the sample relaxed and then the received signal is amplified to be analyised by computer programs

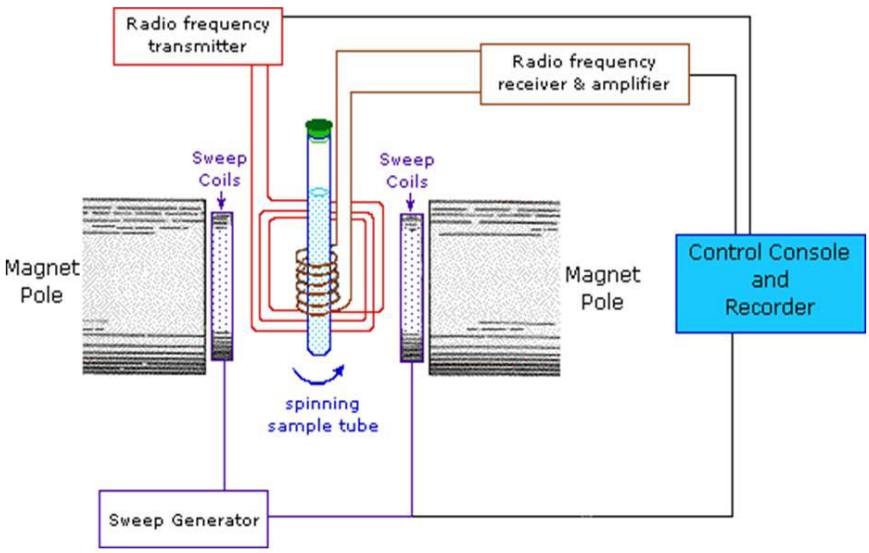

[3]**Figure 2.13** *A schematic representation of NMR spectrometer*

[3] Figure reference: "http://www2.chemistry.msu.edu/faculty/reusch/VirtTxtJml/Spectrpy/nmr/nmr1.htm" website

2.3 Experimental Details

A commercially available CaF_2 powder, containing a minor fraction (<1.5 % wt) of MgO, was selected as a starting material for milling experiments. A planetary mill (Fritsch Pulverisette 6) operating at high rotational speed (400 rpm) was used to prepare a series of ground powders. Both vial and balls were made of hardened chrome steel. One counter-rotating vial (45 ml nominal volume, 1/1 height/diameter ratio) and 12 balls (12 mm diameter) were used in all batches, with a powder weight of 2.11 ± 0.01 g of CaF_2 (including a 2 wt% of ethanol as lubricant), for a corresponding powder to balls ratio of 1:40. The milling time ranged from 4 h to 64 hours.

Diffraction data were collected by a Rigaku PMG/VH diffractometer using a long fine-focus copper tube operated at 40 kV and 30 mA. The machine setup (185 mm goniometer radius, 1° divergence slit, 2° primary and secondary Sollar slits, 1° antiscatter slit, 0.15 mm receiving slit, and a bent graphite monochromator) gives a narrow and symmetric instrumental profile over a 2θ range encompassing the whole pattern of fluorite. Data were collected with a fixed counting time of 30 s per step of 0.05°. Several reflections of the NIST SRM660a LaB_6 line-profile standard **(Cline, et al., 2000)** were collected over the whole accessible 2θ range to obtain a parametric representation of the instrumental profile **(Caglioti, Paoletti, & Ricci, Nucl. Instrum. and Meth. , 1958)**; Necessary for the WPPM evaluation **(Scardi & Leoni, 2002)** **(Scardi & Leoni, Diffraction Analysis of the Microstructure of Materials, 2004)**.

NMR experiments were performed on a Varian InfinityPlus NMR spectrometer operating at a ^{19}F NMR frequency of 376.09 MHz. The NMR spectra were acquired under magic-angle spinning (MAS) conditions using a 4-mm MAS probe at a spinning frequency of 16 kHz. All experiments have been performed at room temperature. The π pulse length was adjusted to be 5 μs. For all samples the spin-lattice relaxation time T_1 was determined by using a saturation recovery sequence to save experimental time compared to the commonly used inversion-recovery-sequence for samples with a long T_1. The data analysis was performed using the normalized signal integrals **(Wilkening, Indris, & Heitjans, 2003)**.

2.4 Results and discussion

The powder diffraction data were analysed by WPPM as a convenient way to simultaneously consider domain size and lattice strain broadening effects **(Scardi & Leoni, 2002)** **(Scardi & Leoni, Diffraction Analysis of the Microstructure of Materials, 2004)**. As suggested by previous studies, dislocations on the primary slip system of fluorite ({001} <110>) **(Muñoz, Rodriguez, & Castaing, 1994)** were considered as the major source of strain broadening. Based on

this information and on the knowledge of the fluorite single-crystal elastic constants **(Every & McCurdy, 1992)**, the dislocation contrast factor was calculated for both edge and screw dislocations **(Giudici, Biddau, D'Incau, Leoni, & Scardi, 2005)** **(Ungár, Dragomir, Révész, & Borbély, 1999)** **(Wilkens, 1970)** as: $C'_{edge} = 0.104228 + 0.388633\ H$ and $C'_{screw} = 0.126335 + 0.060745\ H$, with $H = (h^2k^2+h^2l^2+k^2l^2) / (h^2+k^2+l^2)^2$.

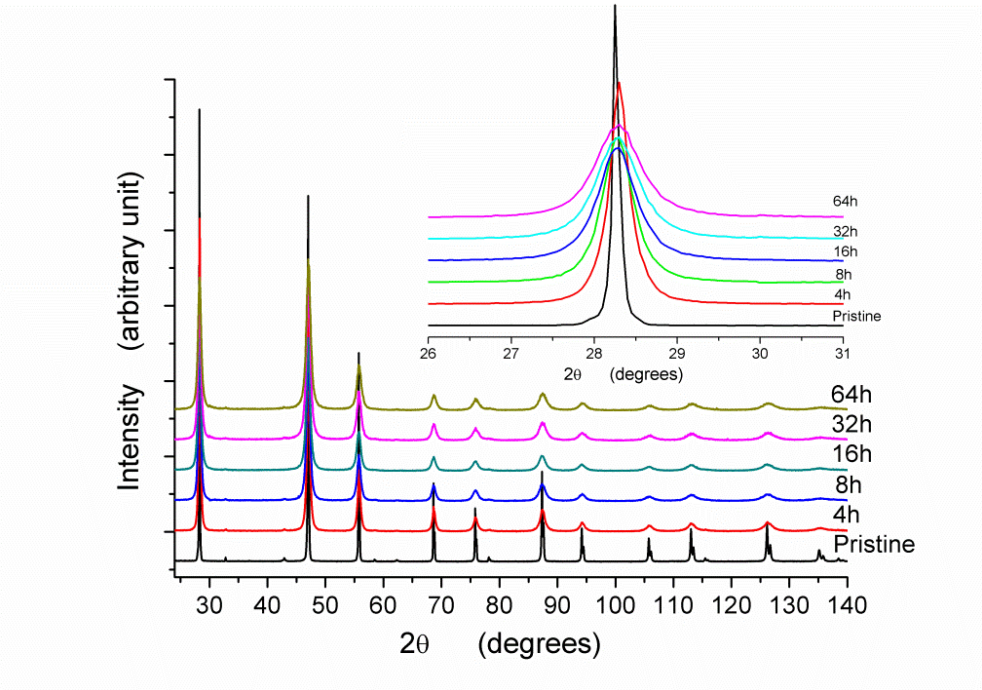

Figure 2.14 *XRD patterns of pristine and milled CaF_2 samples*

WPPM can provide the mean dislocation density (ρ) and the effective cut off radius (R_e) of the dislocation system; a further parameter was introduced to refine the relative fraction of edge (versus screw) dislocations. The domain size effect was modelled by a lognormal distribution (mean μ and variance σ) of spherical domains. All data were analyzed by the software PM2K **(Leoni, Confente, & Scardi, 2006)**, based on the WPPM approach **(Scardi & Leoni, 2002)** **(Scardi & Leoni, Diffraction Analysis of the Microstructure of Materials, 2004)**. In addition to the domain size and dislocations models, refined parameters included those of a chebyshev polynomial background and the unit cell parameter.

Although the milling process gives a progressive line broadening effect (**Figure 2.14**) as expected, the WPPM gave satisfactory results for long milling times (≥32 h) only. Up to 16 hours it seems likely that the powder is not sufficiently homogeneous to be modelled by a single phase. However,

a WPPM analysis with two fluorite phases is unstable, as the parameters of the two phases tend to correlate quite strongly.

A useful support is found in the Solid state NMR spin-lattice relaxation analysis. In general the relaxation time T_1 can be determined by fitting the data, obtained from the saturation recovery experiment, with a monoexponential function

$$M_z(\tau) = K + [1 - \exp(-\tau / T_1)] \qquad \textbf{(2.9)}$$

While K is the background term, $M_z(\tau)$ is the magnetization along the static magnetic field (z axis), τ is the recovery time and T_1 is the spin lattice relaxation time. For the pristine CaF_2 powder a long T_1 of 54.3 s is found, whereas the analysis after extensive milling reveals very short relaxation times, 0.038 s and 0.036 s, respectively for 32 h and 64 h. **Eq.(2.9)** seems not appropriate to model the relaxation data for samples milled for 4, 8 and 16 hours. At short milling times a biexponential function (**Eq. 2.10**) seems more effective:

$$M_z(\tau) = K + C\left[1 - \exp\left(-\tau / T_{1,B}\right)\right] + (1 - C)\left[1 - \exp\left(-\tau / T_{1,A}\right)\right] \qquad \textbf{(2.10)}$$

The expression above provides two relaxations times, $T_{1,A}$ and $T_{1,B}$, for as many fractions, C and (1-C), of fluorite. As shown in **Figure 2.15** for the 4h sample, **Eq.(2.10)** gives a much better fit than **Eq.(2.9)**.

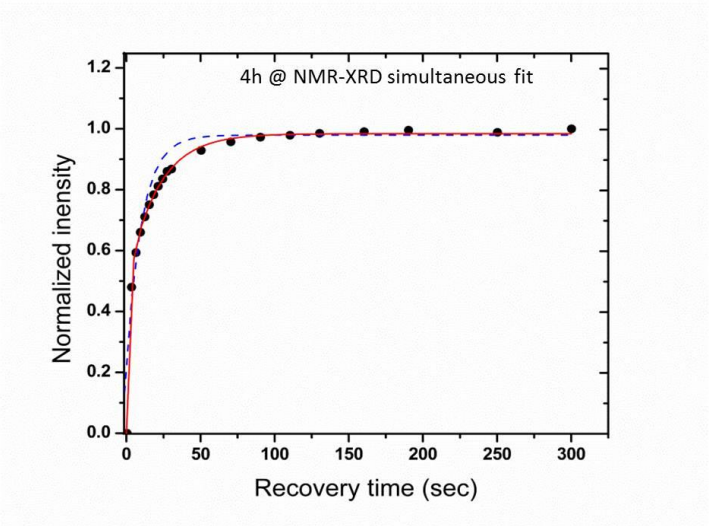

Figure 2.15 *Mono-exponential (dash line) vs. bi-exponential fitting (solid line) for NMR relaxation of CaF_2 milled for 4 h*

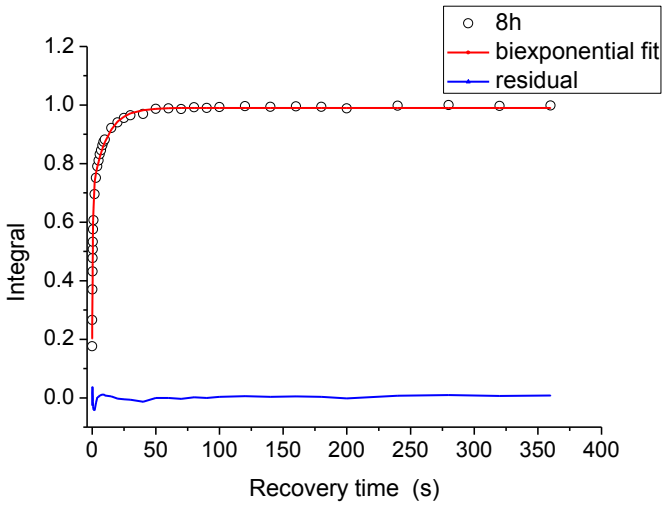

Figure 2.16 *Bi-exponential fitting (solid line) for NMR relaxation of CaF_2 milled for 8 h*

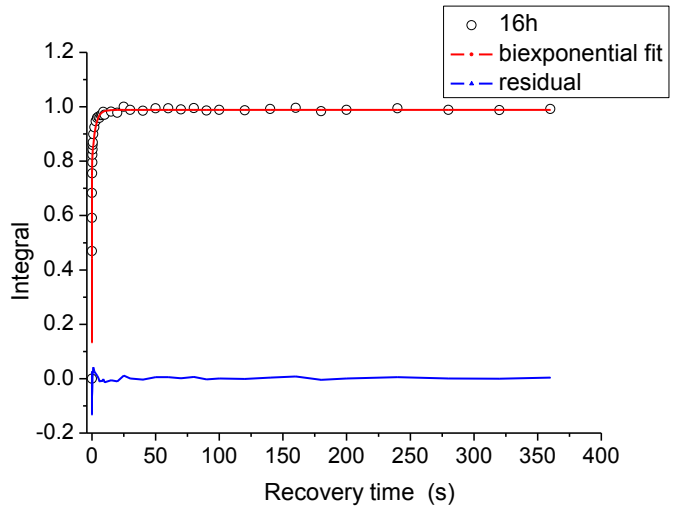

Figure 2.17 *Bi-exponential fitting (solid line) for NMR relaxation of CaF_2 milled for 16 h*

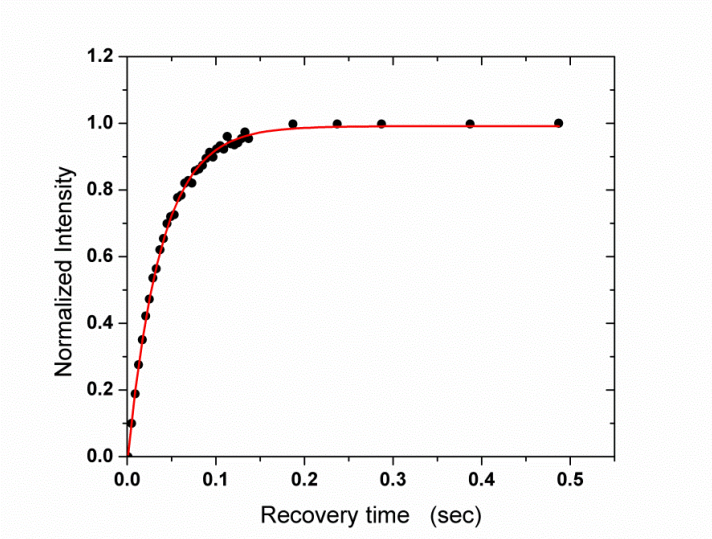

Figure 2.18 *Mono-exponential fitting for NMR relaxation of CaF_2 milled for 32 h*

Before any further consideration of the NMR results, the effect of possible contaminations from the milling process was studied. Steel jar and balls are in fact known to contaminate the powders by magnetic impurities. This is indeed confirmed by **Figure 2.19**, where the results of a UV/Vis photometry reveal a non-negligible iron contamination, linearly increasing with the ball milling time.

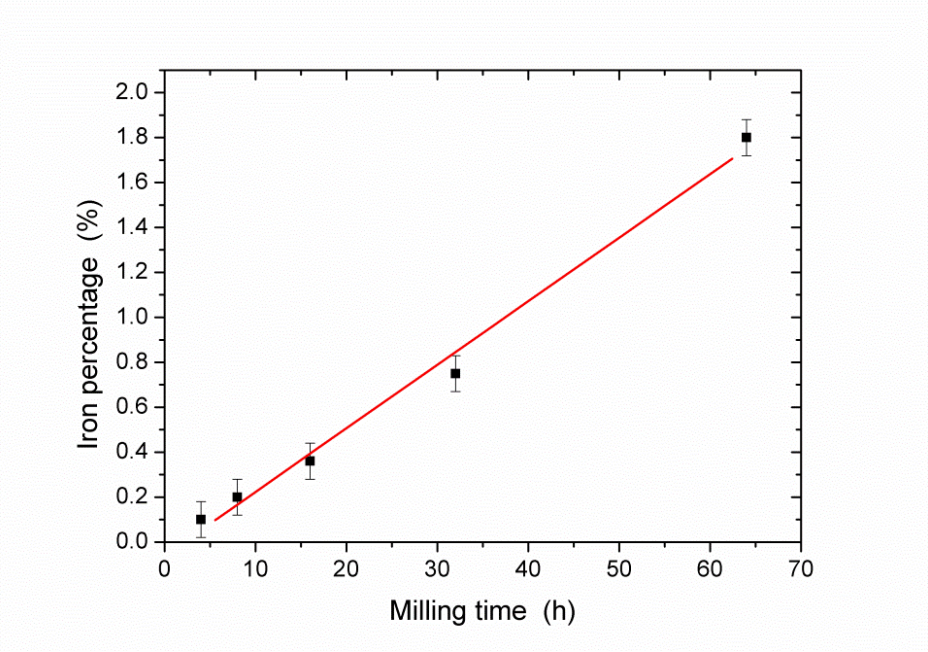

Figure 2.19 *Iron concentration with milling time*

It is worth mentioning that despite the increasing content of iron due to the contamination from the grinding media, the relaxation times and two-phase behaviour described above were not affected. To verify this point a further set of powders was prepared using WC jar and balls, thus introducing no metallic contaminations. The main effect was a shift in the absolute values in the spin-lattice relaxation analysis, but the T_1 values where confirmed within experimental error.

It is therefore demonstrated that, differently from XRD, the solid state NMR spin-lattice relaxation analysis gives a stable modelling of the recovery time, which strongly supports the hypothesis of the two phases for short milling times. After 4 hours of milling, one phase would correspond to a fraction of well ground powder, for which T_1 is much shorter ($T_{1,B}$=1.7(2) s) than in the starting powder; a second phase would consist of little ground fluorite crystals, for which the T_1 is much longer ($T_{1,A}$=20.5(9) s), although shorter than in the pristine material. The corresponding fractions of the two phases are 0.41(2) and 0.59(2), respectively for A and B. The two-phase behaviour is found for samples 4h, 8h and 16h, whereas for 32h and longer there is no convincing

evidence for a second phase. Under the present grinding conditions, 32 hours seem sufficient to achieve a complete homogeneity in the ground powder.

Given the stability of the spin-lattice relaxation analysis, and the marked sensitivity to inhomogeneity, the solid state NMR analysis with the biexponential relaxation behaviour was implemented in the PM2K algorithm **(Leoni, Confente, & Scardi, 2006)**, to perform a simultaneous XRD - solid state NMR modelling. According to the previous results, the parameters were set to model two phases, respectively containing (A) larger crystallites with lower dislocation density connected to a longer T_1, and (B) smaller crystallites with higher dislocation density connected to a shorter T_1. The weight scheme was such to make the fraction of the two phases strongly dependent on the NMR data (C parameter in **Eq.(2.10))**, so to constrain and properly steer the WPPM with the two phases. The result is a stable and robust modelling of both solid state NMR and XRD data. **Table 2** reports the main results of the combined modelling, whereas **Figure 2.20** shows the WPPM result for the 4h sample of **Figure 2.15**.

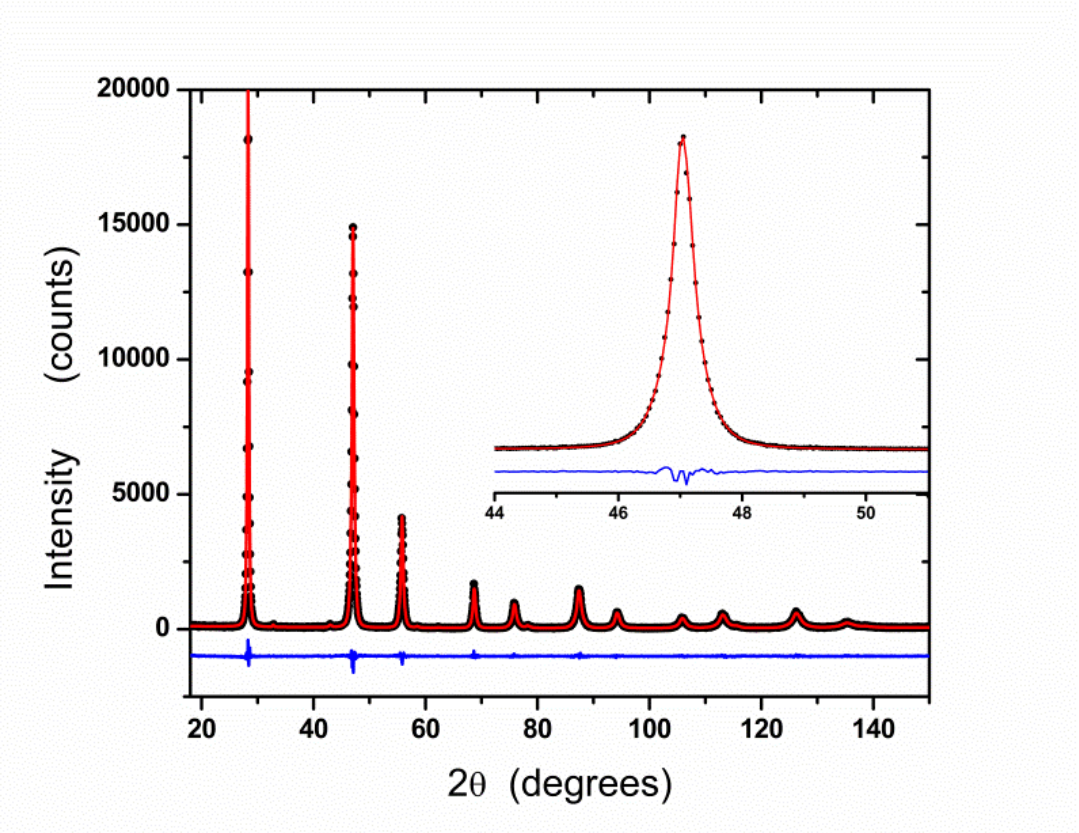

Figure 2.20 *XRD and NMR simultaneous fitting of CaF_2 milled for 4h*

Table 2. *Results of the combined modelling of XRD and Solid State NMR data for fluorite samples ground for an increasing time. Two phases (A,B), corresponding to two fraction of fluorite, were considered for 4, 8, and 16 hours.*

Milling time (h)		Unit cell parameter (nm)	Mean dislocation density (10^{15} m^{-2})	Effective outer cut-off radius (nm)	Mean domain size (nm)	Edge dislocation fraction	T_1 (s)	C (%)
Pristine powder		0.546399(1)			196(7)		54.3	100 @A
4	A	0.54653 (1)	1.2 (3)	24 (8)	61 (18)	0.90	20.5 (9)	41 (2)
	B	0.54658 (2)	8.2 (2)	20 (2)	25 (3)	0.81	1.7 (2)	59 (2)
8	A	0.54656 (2)	1.3(1)	30 **	14 (1)	0.93	11.1 (9)	39 (5)
	B	0.54657 (3)	12.1(6)	8 (1)	13 (2)	0.71	0.46 (2)	61(5)
16	A	0.54679 (3)	0.52*	30 **	12 (1)	1	2.6 (4)	22.4 (3)
	B	0.54682 (2)	11.9 (5)	5.8 (4)	11.29 (1)	0.78	0.038 (2)	77.6 (3)
32		0.54635 (2)	16.6(9)	2.5 (2)	10.7 (5)	0.80	0.038 (1)	100 @B
64		0.54625 (2)	37(5)	1.0 (2)	9.3 (4)	0.68	0.036 (1)	100 @B

Estimated standard deviations are reported in parentheses, referred to the last significant digits.

* The estimated error is very small ≈ (6.22×10^{-5}).

** Effective outer cut-off radius is unstable as the mean dislocation density is very small so it was fixed to a reasonable value to keep the stability of the model.

Phase A is only present in the early stages of grinding, and is characterized by a relatively low amount of dislocations and long relaxation time. After 4 hours of ball milling a large fraction of powder has still few dislocations and an average domain size above 60 nm. As also shown in **Figure 2.21** the percentage of phase A decreases with longer milling, until it disappears in the sample ground for 32 hours, where the powder is made 100% of phase B.

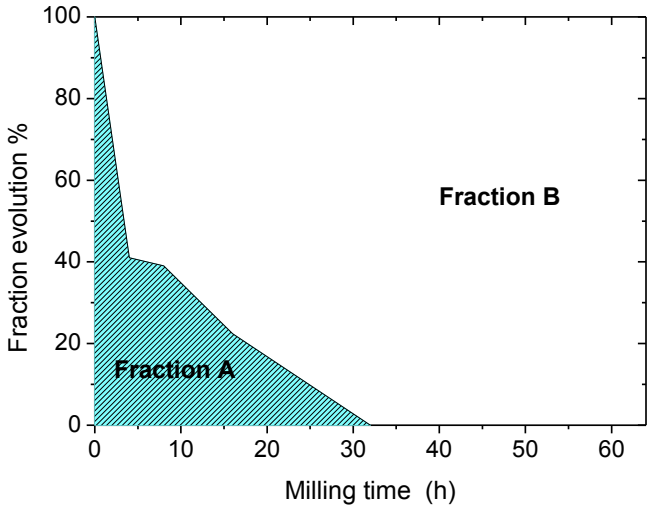

Figure 2.21 *The evolution of fraction B with milling time*

Phase B has a high dislocation density and a small domain size since the early stages of milling: it can be considered as the fraction of most effectively ground powder, where a true nanocrystalline state is reached. It is worth noting that while the mean domain size saturates to ≈10 nm after 8 hours, the dislocation density keeps growing for longer grinding times. At the same time the relaxation time drastically drops to values which are four orders of magnitude smaller than in the starting powder. A decrease in T_1 is also observed in phase A, where despite a relatively unchanged dislocation density, the domain size tends to decrease with the milling time.

Both effects, the decreasing domain size and increasing dislocation density, have an effect on shortening the spin-lattice relaxation time. **Figure 2.22** shows the overall decay of T_1 with the grinding time. While it is well known the effect of small sizes, which involves an increase in the surface to volume ratio and consequent reduction of T_1 **(Scholz, Doerfel, Heidemann, Feist, & Stoesser, 2006)**, it is quite apparent from our results that the lattice distortion caused by dislocations can be even more effective. Dislocations, which appear to be prevalently edge type (an observation compatible with previous results and TEM studies **(Giudici, Biddau, D'Incau, Leoni, & Scardi, 2005)**), become the main factor controlling the spin-lattice relaxation time.

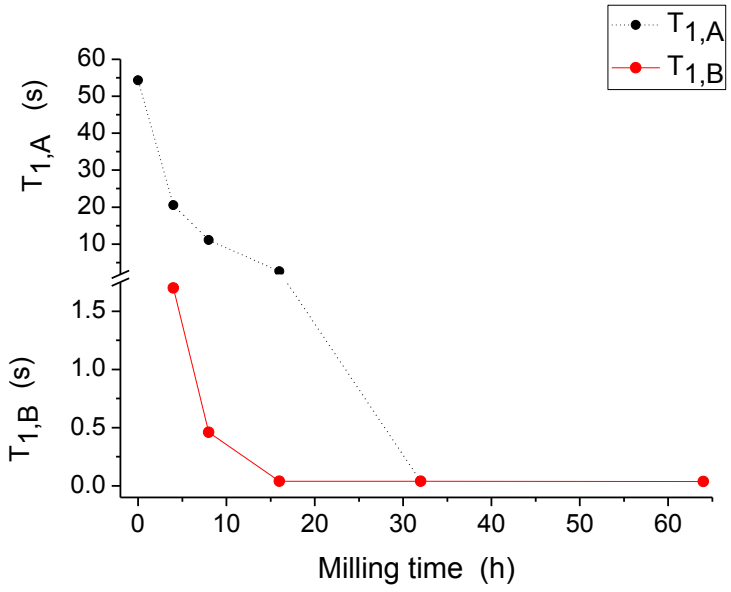

Figure 2.22 *Fractions A and B relaxation times dependence with milling time*

The T_1 tends to saturate to 40 ms or slightly less after 16 hour (phase B) and longer (32 and 64 h) milling times. In the latter three cases, while the dislocation density increases, the effective outer cut-off radius decreases, giving a Wilkens factor ($M = R_e\sqrt{\rho}$) in the range 0.25÷0.6.

According to the theory **(Scardi & Leoni, 2002)** **(Scardi & Leoni, Diffraction Analysis of the Microstructure of Materials, 2004)**, such small values of M (<1) can result from an increasing interaction among dislocations, as in dipoles or in domain walls and nanocrystal grain boundary regions, in such a way that the overall lattice distortion effect tends to saturate, in accordance with the nearly constant spin-lattice relaxation time measured in the most extensively ground powders.

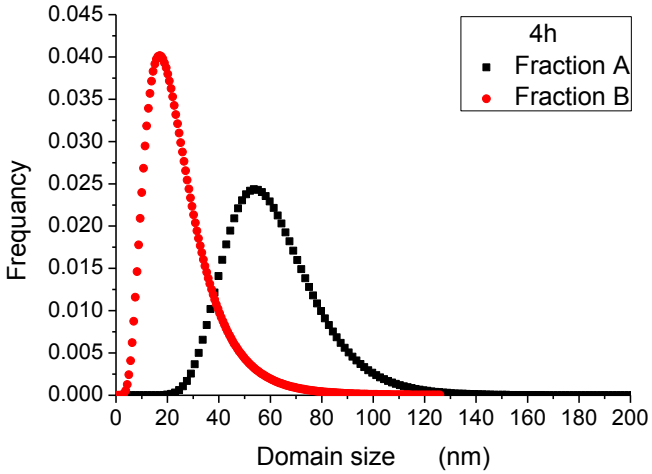

Figure 2.23 *The size distribution for each fraction after 4 hours*

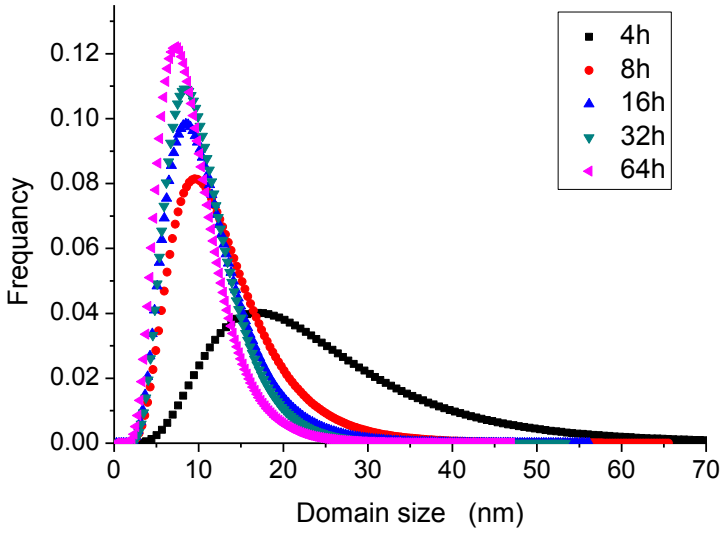

Figure 2.24 *The progress in the size distributions of fraction B with milling*

2.5 Conclusions

The present work shows the positive combination of Solid State NMR relaxometry and X-ray Diffraction in the description of high energy grinding of fluorite. NMR and XRD data were simultaneously refined according to known theoretical expressions, respectively a biexponential function for the T_1 relaxation and the WPPM algorithm for the XRD Line Profile Analysis.

The combined use of the two techniques is especially useful in dealing with the inhomogeneity of powders ground for short milling times. Results suggest the presence of two phases (i.e., two fluorite fractions): phase A, containing larger crystallites with a low dislocation density, is a fraction of powder relatively unaffected by milling; phase B, with much smaller crystalline domains and an ever increasing dislocation density, is the fraction of material efficiently ground by the milling process. The two phases evolve, for ball milling times of 32 h and longer, in a single nanocrystalline phase where the spin-lattice relaxation time decays to quite small values (less than 40 ms), while domain size and dislocation density, as provided by LPA, respectively decrease to ≈10 nm and increase to $\approx 37 \times 10^{15}$ m^{-2}, with a rather high dislocation interaction.

Fraction B with higher defected and smaller crystallite size leads to shorter T_1 compared to fraction A but the full picture of T1/WPPM relationship is not completely understood at this stage, in particular whether size or lattice distortion (e.g. dislocations) give the principal contribution to T_1. Therefore, a further investigation to separate the size and dislocations contributions to T_1 will be discussed in the next chapter.

CHAPTER III

Correlations of Lattice Strain/Domain Size with Spin-Lattice Relaxation Time in Nanocrystalline CaF_2

M. Abdellatief , M. Abele, M. Leoni and P. Scardi

Part of this chapter has been submitted in:

Journal of Applied Crystallography, (2013) submitted

Abstract

Nanocrystalline CaF_2 powder specimens were produced both by co-precipitation of $CaCl_2$ and NH_4F and by ball milling of a coarse powder. The specimens homogeneity and a detailed picture of the lattice defects can be assessed by the simultaneous analysis of the powder diffraction pattern and of the solid state ^{19}F MAS NMR T_1 relaxometry data. While diffraction line profiles provide information on domain size distribution and content of dislocations, T_1 relaxometry is more sensitive to inhomogeneity of the powder (large defect free grains versus defective small ones). After extensive milling, it is possible to obtain fluorite domains of comparable size as the chemically synthesized CaF_2 (ca 10-12 nm), but with a marked difference in lattice defect types and content. It is then proved that surface defects (related to domain size), line defects (dislocations) and point (Frenkel) defects have quite e different effect on the powder pattern as well as on the T_1 spin-lattice relaxation time.

3.1 Introduction

Lattice defects are of interest in many applications of nanostructured materials, as they influence most of the technologically relevant properties. As an example, dislocations and stacking faults have a dramatic effect on the transport properties of ionic conductors **(Niklasson & Granqvist, 2007)**. Fluorite (CaF_2) is one of the simplest and most common ionic conductors, easy to produce, with a cubic (*fcc*) crystal structure and an NMR active nucleus (^{19}F). It is known that the conductivity of the material is enhanced by temperature, but also by the reduction of the grain size to the nanometric range **(Ruprecht, Wilkening, Steuernagel, & Heitjans, Anion diffusivity in highly conductive nanocrystalline BaF2: CaF2 composites prepared by high energy ball milling, 2008)**, which enhances the effect of grain boundaries, dislocations and point defects. It is therefore important to produce nanostructured materials with controlled variety and amount of lattice defects, as well as to develop reliable methods to study and quantify their presence.

Two industrially scalable processes are commonly used to obtain nanostructured materials: high energy grinding (e.g. ball milling) as a cost effective top down route, and chemical synthesis, as a usually more expensive but more flexible bottom up approach. The major differences between the two are in the minimum size that can be obtained, and in the possibility to control type and density of defects. While the bottom up approach can potentially give particles of any size and shape with a rather controlled (usually low) density of defects, high energy grinding has a minimum size limit (which depends on the specific material and milling conditions **(Suranarayana, 2001)**) and usually introduces a quite high density of lattice defects. As a clear example of these two different routes, ball milled fluorite can reach domain sizes of 10-12 nm with quite high dislocation density (~10^{16} m^{-2} and above **(De Giudici, Biddau, D'Incau, Leoni, & Scardi, 2005)**), whereas a co-precipitation can yield nearly defect-free nanocrystals, with a comparable or smaller size (**(Wang, Fan, Pi, & Wang, 2005)** **(Omolfajr, Nasser, & Mahmood, 2011)**).

Transmission Electron Microscopy (TEM) is a reference technique for the study of nanostructured materials, providing direct evidence about size, shape and defects, albeit at the cost of being local, i.e. not always representative for the whole specimen under analysis. X-ray diffraction (XRD) is ideally complementary to TEM as it is sensitive (especially in the peak profiles) to the coherent scattering domains and to atomic displacements, and the information is usually averaged over a large volume (several mm^3) of specimen. State of the art methods of Line Profile Analysis, like Whole Powder Pattern Modelling (WPPM) **(Scardi & Leoni, 2002)** **(Scardi & Leoni, Whole Powder Pattern Modeling: theory and applications, 2004)** can be rather informative when applied to nanocrystalline and heavily deformed materials. Based on a nonlinear

least squares minimization procedure applied to powder diffraction data, WPPM refines the values of a few significant parameters which describe the nanostructure, among which domain shape and size distribution, and concentration of defects, like dislocations and stacking faults (**(Scardi & Leoni, 2002)**, **(Scardi P. , 2008)**).

Investigating nanocrystalline materials by a combination of TEM and XRD/WPPM is nowadays a routine, for homogeneous specimens. Although this is frequently true of chemically synthesised materials with not too small (and "non exotic"[4]) shapes, it is not always verified for mechanically ground materials. Even if high energy impacts cause fragmentation and extended plasticity, the early stages of the process usually leave fractions of less or totally not affected material. If not fully recognised by previous knowledge (e.g. microscopy) and/or unsatisfactory quality of the WPPM results, this condition can lead to wrong estimates of domain size and defect content; if data quality is sufficiently good, advanced methods can possibly be used, like refining a free histogram distribution **(Leoni & Scardi, 2004)**, as an attempt to model a bimodality in the specimen microstructure **(De Giudici, Biddau, D'Incau, Leoni, & Scardi, 2005)** **(Leoni, De Giudici, Biddau, D'Incau, & Scardi, 2006)**. However, as a matter of fact, powder diffraction is not suitable to analyze non-homogeneous samples, even if simply made of just two fractions: the main structural features might be too similar (i.e. Bragg spots are coincident) that a reliable separation of the fractions is not possible.

Quite surprisingly, solid state Nuclear Magnetic Resonance (ss-NMR) spectroscopy can help solving the non-homogeneity problem. Traditionally employed for structural analysis, this technique shows in fact intensity variations and broadening of the (NMR) peaks for nanocrystalline or highly defective powders. This is related to the sensitivity of NMR to the local environment of the nuclei (and thus bond angles and atomic environment), strongly influenced by size effects and by the presence of disorder like that caused by the strain field of dislocations **(Eckert H. , 2008)**. However, the most frequent applications in this field refer to point defects (see, e.g. the applications of ^{19}F NMR spectroscopy to study point defects and F^- mobility in fluorites **(Ruprecht, Wilkening, Steuernagel, & Heitjans, 2008)** **(Jain P. , Kim, Youngman, & Sen, 2010))**.

In the previous chapter **(Abdellatief, Abele, Leoni, & Scardi, 2013)**, we proposed to combine solid state ^{19}F MAS NMR T_1 relaxometry and XRD/WPPM to study different stages of fluorite ball

[4] non-crystallographic (e.g. icosahedral, decahedral) nanocrystals are not considered here as the analysis of the corresponding diffraction pattern calls of alternative techniques such as the Debye scattering equation ((Debye, 1915), (Vogel, Rosner, & Tesche, 1993), (Cervellino, Giannini, & Guagliardi, 2003), (Cervellino, Giannini, & Guagliardi, 2006), (Gelisio, Azanza Ricardo, Leoni, & Scardi, 2010))

milling. Although the paramagnetic contamination of the steel jar caused systematic decrease of T_1, relaxometry proved to be sensitive to inhomogeneity, and in particular to correctly steer the XRD/WPPM of two-fraction models (respectively for ground and not (or little) ground powder). This approach is further developed in the present work, with a much deeper insight in the mechanisms affecting T_1 relaxometry of fluorite, to unveil the role of different lattice defects. The comparison between nanocrystalline fluorite produced by the two processes described above with comparable domain sizes but quite different defectivity, shows that the effect of decreasing domain size (i.e., increasing surface and grain boundaries), increasing dislocation density and point (Frenkel) defects are quite different. Remarkable agreement and complementarity between T_1 relaxometry and XRD/WPPM results is demonstrated.

3.2 Experimental

A commercial CaF_2 powder (98.5 % purity) was ground using a Fritsch Pulverisette 6 high-energy planetary mill. The machine was operated at high rotational speed (400 rpm) using tungsten carbide balls and vial: the counter-rotating vial (45 ml nominal volume, 1/1 height/diameter ratio) was loaded with 1.88 ± 0.01 g of CaF_2 powder, 0.04 ± 0.01 g (2 wt%) of ethanol as lubricant and 10 balls (total ball weight 75 g), for a corresponding powder-to-ball weight ratio of 1:40. Milling times ranged from 4 to 64 hours.

Nanocrystalline fluorite was also prepared by a direct co-precipitation method, as a product of the exchange reaction between $CaCl_2$ and NH_4F. A 0.1 molar solution of $CaCl_2$ in ethanol (0.1 mol/L $CaCl_2$) was firstly prepared. According to previous studies, the dissociation rate of $CaCl_2$ strongly depends on the solvent concentration **(Wang, Fan, Pi, & Wang, 2005)** **(Omolfajr, Nasser, & Mahmood, 2011)**: the higher the concentration, the higher the time required having a clear solution (corresponding to complete dissociation of $CaCl_2$ in ethanol). An appropriate amount of NH_4F (0.02 mol) was then added to the solution which was then stirred for at least 16 hours at room temperature (a few days are needed for the specimen in pure ethanol, before any sign of change is evident). The white precipitate obtained during the stirring was then separated from the solution by high speed centrifugation (5000 rpm), and then rinsed several times in distilled water and in ethanol to remove undesired ions. Finally, the precipitate was dried in air at room temperature and softly ground in an agate mortar to break up larger aggregates.

XRD data were collected on a Rigaku PMG/VH diffractometer, using CuK_α radiation from a long fine-focus tube operated at 40 kV and 30 mA. Optical components and instrumental set-up (185 mm goniometer radius, 1° divergence slit, 2° primary and secondary Soller slits, 1° antiscatter slit, 0.15 mm receiving slit, and a bent graphite monochromator) were such to produce narrow and symmetric

instrumental profiles over the 2θ range of interest **(Caglioti, Paoletti, & Ricci, 1958)** **(Scardi, Ortolani, & Leoni, WPPM: microstructural analysis beyond the Rietveld method, 2010)**. Diffraction data were collected from 20 to 150 deg 2θ at 0.05° steps with a fixed counting time of 30 s per point. Reflections of the NIST SRM660a LaB_6 line-profile standard were collected over the whole accessible 2θ range under the same conditions used for the fluorite samples. In this way a parametric representation of the instrumental profile was obtained, to correct the fluorite line profiles according to a well-established, simple and sufficiently accurate procedure **(Caglioti, Paoletti, & Ricci, 1958)** **(Scardi, Ortolani, & Leoni, WPPM: microstructural analysis beyond the Rietveld method, 2010)**.

All XRD patterns were analysed with the PM2K program **(Leoni, Confente, & Scardi, 2006)**, implementing the Whole Powder Pattern Modelling (WPPM) approach **(Scardi & Leoni, 2002)** **(Scardi & Leoni, Whole Powder Pattern Modeling: theory and applications, 2004)**. Besides the instrumental component, line profiles were modelled considering size effect from a lognormal distribution of equiaxed (i.e. spherical on average) domains, and strain effect due to dislocations. The latter were assumed to lay on the primary slip system of fluorite **(Muñoz, Domingguez-Rodriguez, & Kasstaing, 1994)**, for which the average contrast factor for edge and screw dislocations ($\overline{C}_{edge} = 0.104228 + 0.388633H$, $\overline{C}_{screw} = 0.126335 + 0.060745H$, respectively **(Leoni, De Giudici, Biddau, D'Incau, & Scardi, 2006)**, **(Scardi & Leoni, 2002)** **(Scardi & Leoni, Whole Powder Pattern Modeling: theory and applications, 2004)**) parameterised on $H = \left(h^2k^2 + k^2l^2 + h^2l^2\right) \Big/ \left(h^2 + k^2 + l^2\right)^2$ provides a description of the anisotropic line broadening effect. In addition to peak intensities and a Chebychev polynomial background function, refined parameters were lognormal mean (μ) and variance (σ) of the distribution, average dislocation density (ρ), effective outer cut-off radius (R_e), fraction of edge dislocations (f_E) and unit cell parameter (a_0).

The NMR spectra were collected on a Varian InfinityPlus NMR spectrometer operating at the ^{19}F NMR frequency of 376.09 MHz. Room temperature magic-angle spinning (MAS) spectra were collected using a 4-mm MAS probe at a spinning frequency of 16 kHz, and a π/2 pulse length adjusted to 5 μs. The spin-lattice relaxation time T_1 was determined for all studied samples: instead of the commonly used inversion-recovery sequence, a saturation recovery sequence was used. This resulted in a reduction of the data collection time for the shortly milled samples, characterized by a long T_1. Data analysis was made on normalized signal integrals **(Wilkening, Indris, & Heitjans, 2003)**.

3.3 Results and discussion

3.3.1 Extensively ground CaF_2: combined WPPM/NMR analysis

Figure 1 shows an example of the ^{19}F NMR spectra of ball milled fluorite. Independently of the milling time, all spectra consist of a broad resonance with strong spinning side bands, still present at rather high spinning rates, thus revealing the high Chemical Shift Anisotropy (CSA) found for these samples **(Smith & Burum, 1989)**. The employed MAS probe does not allow the identification of possible multiple fluorine sites, even at its top spinning rate (28 kHz); on the other hand, the literature shows that the resolution increase obtained by spinning above 30kHz would be insufficient to separate the strong signal overlapping **(Ruprecht, Wilkening, Steuernagel, & Heitjans, 2008)**.

For comparison, **Figure 3.1** also shows the ^{19}F NMR spectrum of fluorite ball milled in steel vials. While the isotropic chemical shift is the same in both spectra, the CSA is strongly affected by the different grinding environment. The samples milled in steel show more spinning side bands with strongly increased intensities, as an effect of the paramagnetic contribution of iron contamination to the CSA. This contribution cannot be easily separated from those of the microstructure **(Abdellatief, Abele, Leoni, & Scardi, 2013)**(see chapter 2), which can be more reliably studied in the samples of the present study, ground in WC.

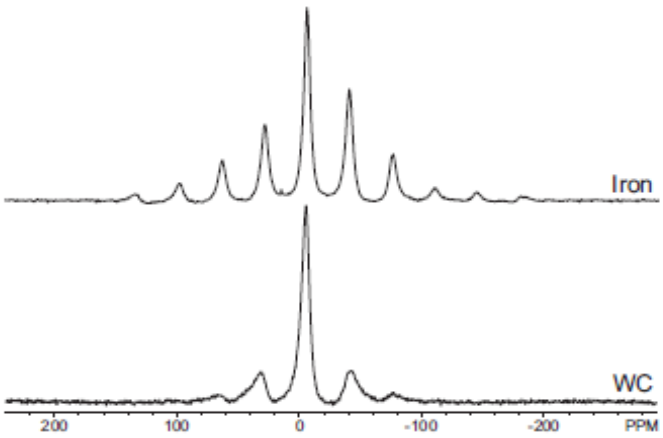

Figure 3.1 *^{19}F MAS NMR spectra recorded at a spinning rate of 16 kHz for two samples milled for 16 h with balls and jar respectively made of WC (bottom) and hardened chromium steel (top). The larger noise in the WC spectrum is caused by a lower number of signal accumulations.*

More interesting than MAS spectra alone is definitely the ^{19}F spin-lattice relaxation time T_1 i.e. the rate of recovery of the longitudinal magnetization component, M_z. It is well known that the local structure has a major effect on the relaxation time. **Figure 3.2** shows a typical series of MAS spectra recorded for different recovery times.

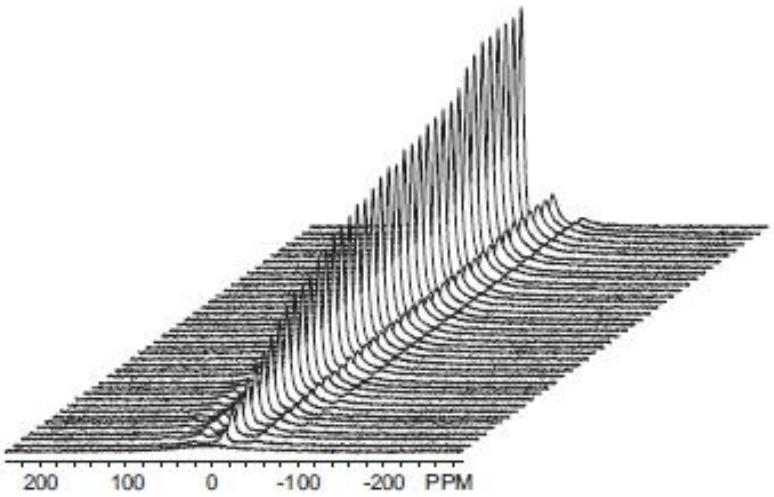

Figure 3.2 *^{19}F MAS NMR spectra for a CaF_2 sample milled for 64 h, as recorded at a spinning rate of 16 kHz with the saturation-recovery sequence for recovery times between 0 and 16 s*

To determine the spin-lattice relaxation time for a certain sample, the integrals of all spectra (proportional to M_z) are extracted and plotted against the recovery time, as shown in **Figure 3.3** for the samples milled for 8 and 64 h. The data are then modelled with a function:

$$M_z(\tau) = K + C\left[1 - \exp\left(-\tau/T_1\right)\right] \qquad (\mathbf{3.1})$$

where τ is the (known) recovery time, C is the maximum amplitude, T_1 is the spin-lattice relaxation time and K is a background term. This procedure works well for the pristine fluorite powder (T_1 = 54.3 s) and for the extensively ground samples, 16 h (T_1 = 0.54 s), 32 h (T_1 = 0.79 s) and 64 h (T_1 = 0.31 s), but is not suitable for samples milled for 4 h and 8 h. **Figure 3**, shows for instance that **eq. (3.1)** does not match the experimental data for the sample milled for 8 h. For the samples ground for 4 and 8 h, a different approach is therefore needed in order to describe the relaxation process.

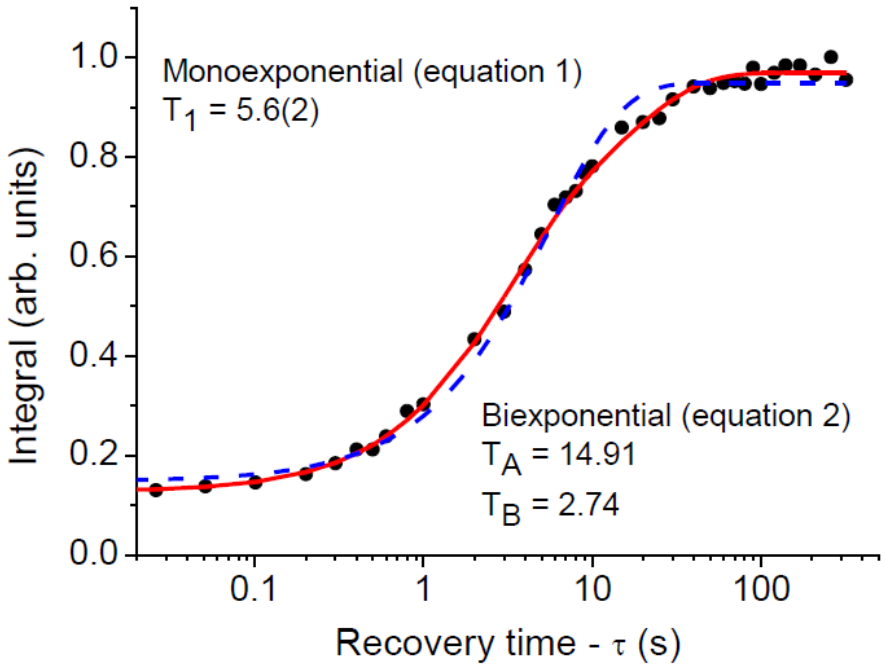

(3.3a)

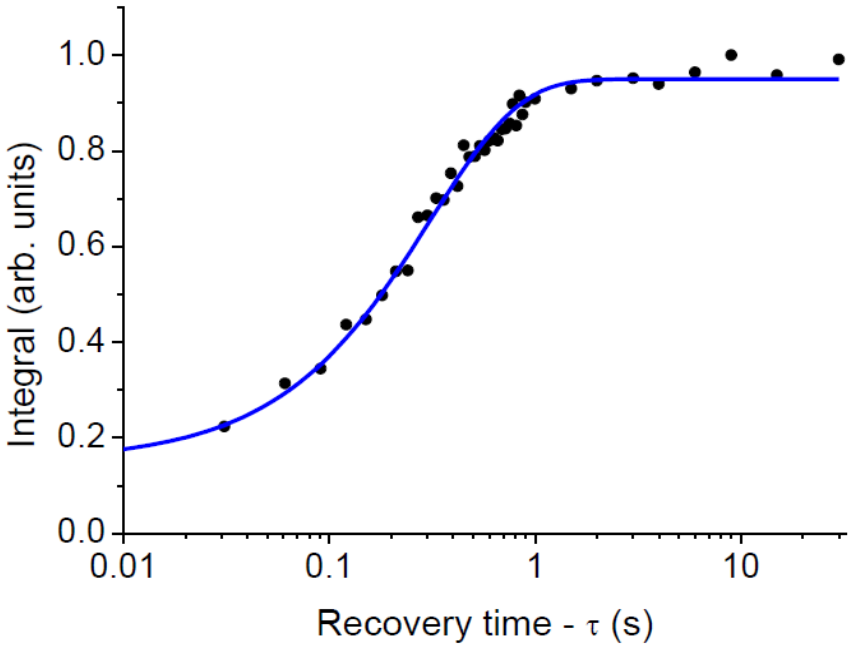

(3.3b)

Figure 3.3 *(a) Relaxation data for the fluorite sample ball-milled for 8 h. Best fit results are shown for eq.(3.1) (dash) and eq.(3.2) (line). (b) Relaxation data for the fluorite sample ball-milled for 64 h. The line is the best fit using eq. (3.1).*

Starting from the consideration that a short milling time does not produce a homogeneously ground powder, we can adopt a simple model based on the presence of two fluorite fractions (or components) A and B. According to this model, data as those of **Figure 3.3** can be modelled by a biexponential curve **(Abdellatief, Abele, Leoni, & Scardi, 2013)**:

$$M_z(\tau) = K + C\left[1-\exp\left(-\tau/T_{1,B}\right)\right] + (1-C)\left[1-\exp\left(-\tau/T_{1,A}\right)\right] \quad (3.2)$$

where C is the amplitude of component B, and where $T_{1,B}$ and $T_{1,A}$ are, respectively, the relaxation times of component B and A. **Figure 3.3** shows the fitting result for the 8 h sample in comparison with the single exponential approach of **eq. (3.1)**. A more robust convergence with an R factor close to unity is found, leading to two relaxation times of 14.9 and 2.74 s.

It is worth underlying that this is just a simplified model, based on the consideration that not all grains are effectively ground within the first 8 h milling. The two components could therefore represent the ball milled fraction and the pristine (not milled or little milled) residual fraction, respectively. A more accurate description involving a continuous distribution of differently ground fractions would be rather impractical, and probably too complex to extract from the limited NMR relaxation data. Although the two fraction model is realistic **(Heitjans & Indris, 2003)**, NMR relaxometry data alone is insufficient to univocally support this interpretation. For example, the observed trend for short milling times could be related to the presence of two different fluorine sites, distinguishable by their relaxation behaviour **(Jain P. , Kim, Youngman, & Sen, 2010)**. The two component relaxation behaviour could also be related to the different local atomic environment of grain bulk and surface atoms, effect enhanced in nanomaterials.

The use of an independent technique is the best solution to validate the NMR result. As shown in **Figure 3.4**, XRD is very sensitive to the effects of grinding, which visibly changes the diffraction line profiles. A search match followed by a quantitative phase analysis identifies minor a contamination by MgO (<1.5 wt%), already in the pristine powder. The WPPM analysis can provide a detailed picture of the microstructure in terms of crystalline domain size distribution and density of dislocation, the major lattice defects in ball milled fluorite **(Leoni, De Giudici, Biddau, D'Incau, & Scardi, 2006)**.

A WPPM run considering just one CaF_2 and one MgO phase works well for highly milled samples (16 h or more), but is unsatisfactory for shortly milled ones. In fact, as shown e.g. in a recent paper **(Abdellatief, Abele, Leoni, & Scardi, 2013)**, XRD (and WPPM as a consequence) is rather weak

in distinguishing different fractions of the same fluorite phase, i.e. an inhomogeneity of the specimen. As a consequence, the WPPM of the patterns of samples 4h and 8h with two separate fluorite fractions is highly unstable, and does not lead to univocal results: even if the line profiles from the pristine powder fraction are much narrower than those of the ground fraction, the main structural parameters are the same. Therefore, Bragg peaks fall at nearly identical positions, causing a strong correlation between the parameters of the two fractions.

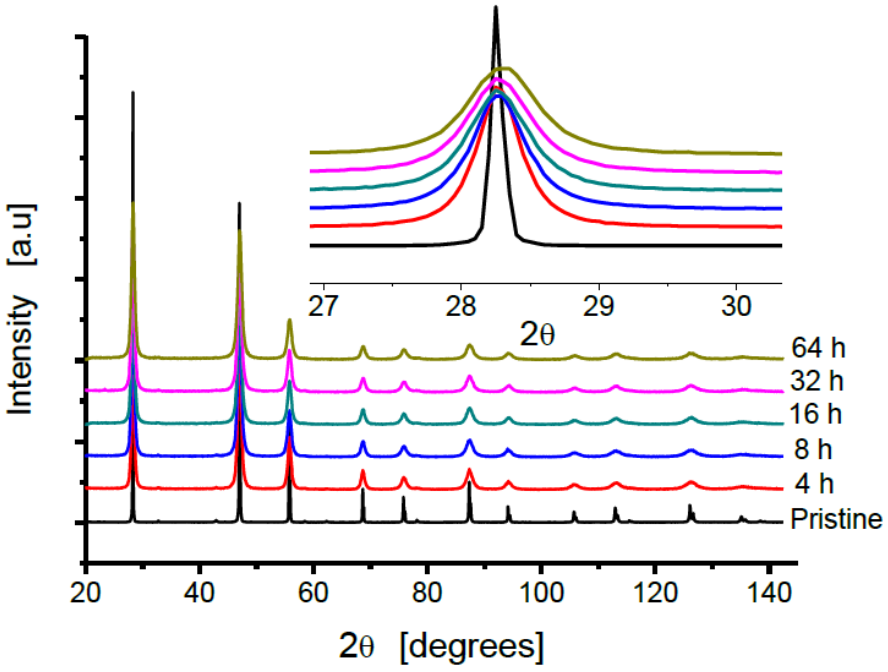

Figure 3.4 *XRD patterns for fluorite samples ball milled for different time. The inset shows the progressive broadening effect of grinding on the (111) peak.*

To overcome this problem we can use the NMR relaxation data to stabilize the WPPM analysis: in particular, we can simultaneously fit both the NMR relaxation and the XRD data on the same model using the minimization algorithm supported by the PM2K software **(Leoni, Confente, & Scardi, 2006)**. In practice, the two fluorite components for samples 4h and 8h are considered as two separate but structurally identical phases, whose relative fractions are determined by the refined values of C and (1 - C) from **eq. (2)**. The WPPM analysis then provides domain size and dislocation parameters for the two fractions A and B i.e., respectively, the fraction of specimen less affected (long T_1) and more affected (short T_1) by grinding. Given the high sensitivity to inhomogeneity

demonstrated by the NMR analysis, the same total weight was simultaneously refined from relaxometry and powder diffraction data, in order to steer the WPPM toward the best solution.

As clearly demonstrated in **Figure 3.5** for the 8h sample, the simultaneous modelling of XRD and NMR relaxometry is remarkably good. Analogous results are obtained for the 4h sample. Beyond the visual quality of the agreement between data and model, the important point here is the stability of the procedure, which results from the simultaneous modelling of the two independent data sets. The other (homogeneous) samples were modelled considering one CaF_2 fraction only: consistently with the two-fraction model, the pristine powder can be considered as fraction A, whereas samples ball milled for 16 h, 32 h, and 64 h are labelled as fraction B.

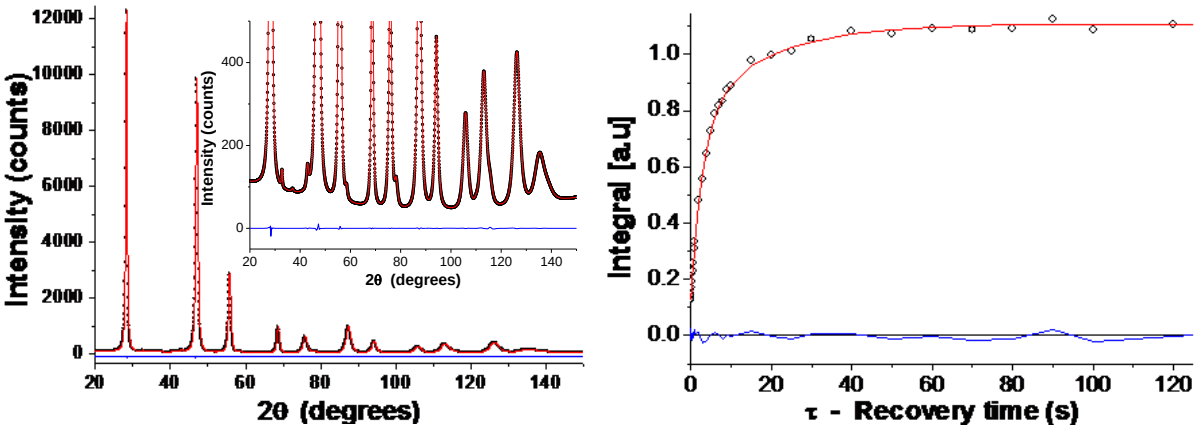

Figure 3.5 *Simultaneous modelling of XRD powder pattern and NMR relaxation data for sample 8h. Experimental data (circle) and refined model (line). Difference plot is shown below. The inset shows a detail of the peak tail region. See text for details.*

Table 3.1 summarizes the most significant results of the combined modelling. Starting from the pristine powder, we note the large domain size (at the upper sensitivity limit of the technique) and an absence (or density below detection limit) of dislocations, corresponding to a long T_1 (54 s). Consistently with the two-fraction model introduced above, 4 and 8 h milling yields fractions A and B: the former has a low dislocation density, relatively long effective outer cut-off radius, large (but still nanometre scale) domain size and long T_1 (around 20 s). Fraction B, instead, has a higher dislocation density, shorter R_e, smaller domain size, and a correspondingly short T_1. The features of

fraction B are preserved in specimens milled for 16 h and longer. The relative fractions of A and B and the corresponding T_1 trends as a function of milling time are shown in **Figure 3.6**.

Table 3.1 *Main results of the combined WPPM of XRD patterns and Solid State NMR relaxometry data. The two-fraction (A,B) model was adopted for samples 4, 8, 16 h.*

Milling time (h)		**Lattice parameter (Å)**	**Mean dislocation density (10^{15} m^{-2})**	**Effective cutoff radius (nm)**	**Average domain size (nm)**	**Fraction of edge dislocations**	**T_1 (s)**	**CC %**
Pristine	A	5.46399(1)			196(7)		54.3	
	B							None
4	A	5.4658(1)	2.2(1)	60(12)	25(2)	0.7(1)	20.6(4)	63.4
	B	5.4649(3)	13.8(1)	22(3)	19(10)	0.7(1)	2.6(1)	36.6
8	A	5.4665(2)	1.39(4)	50	20(7)	1	15(4)	41.3
	B	5.4649(3)	16(1)	1(1)	16(8)	0.7(1)	3(5)	58.7
16	A							None
	B	5.4648(1)	12(1)	3.3(2)	13(1)	0.7(1)	0.54(1)	100
32	A							None
	B	5.4646(1)	17(1)	2.2(2)	11(5)	0.5(1)	0.79(2)	100
64	A							None
	B	5.4645(2)	31(7)	1.2(3)	11(4)	0.4(1)	0.31(1)	100

Estimated standard deviations, reported in parentheses, refer to the last significant digit.

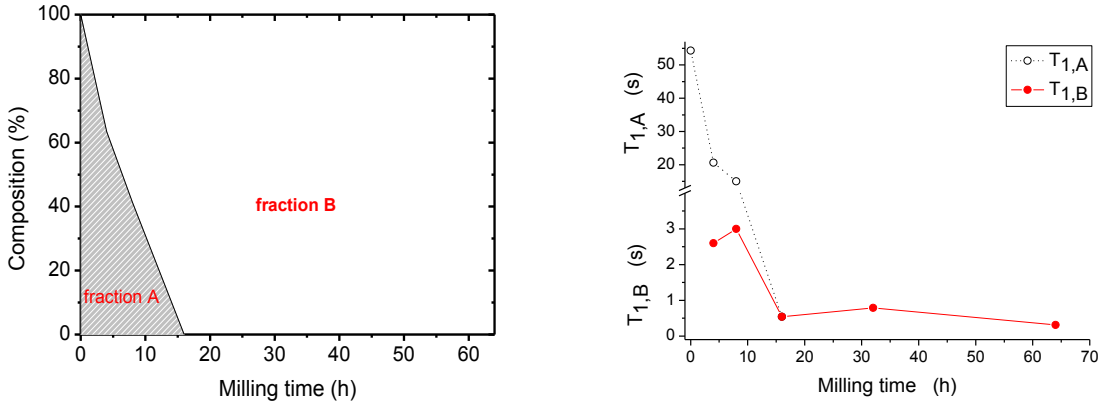

(a) (b)

Figure 3.6 *Percentages of fluorite fractions A and B (a) and corresponding T_1 values (b) as a function of the ball milling time.*

These results suggest the following description of the milling process. The starting CaF_2 powder is a microcrystalline material with a relatively low dislocation density. In the first stages of milling just a small fraction of the material is ground with sufficient efficiency. Two fractions therefore start to effectively coexist, differing in domain size and defectivity: lightly ground grains (fraction A) and more heavily processed grains (fraction B) showing a smaller size and a higher dislocation density induced by the more intense mechanical force they have been exposed to. It takes at least 8 h of milling before the system reaches a homogeneous condition, corresponding to a minimum domain size of 12-13 nm. From this point on, further ball milling only causes an increase of the dislocation density which should also saturate for very long milling times, as an effect of the dynamic recovery mechanisms typical of high energy mechanical grinding.

It seems worth noting that changing the grinding set e.g. from WC to iron does not alter the qualitative result shown here. Besides possible effects related to the lower specific weight and higher thermal conductivity of iron (influencing the specific energy during the milling), an important difference comes from the effect of contamination which led to about one order of magnitude smaller T_1 values **(Abdellatief, Abele, Leoni, & Scardi, 2013)**.

Despite the detailed picture emerging from the results shown so far, the correlation between microstructural parameters and NMR relaxation time is still unknown in the literature. Both dislocation density and crystalline domain size are however expected to affect the spin-lattice relaxation mechanism. The domain size reduction to the nanoscale directly increases the surface/volume ratio which, in turn, strongly affects the shielding of the nuclei (the coordination of bulk and surface atoms is clearly different). Since the relaxation time is strongly influenced by the

local atomic environment, this causes a decrease of the relaxation time **(Rabbani & Edmonds, 1994)**. However, a similar effect can originate from the distortion caused by lattice defects, like dislocations, which activate additional relaxation modes **(Scholz, Dorfel, Heidemann, Feist, & Stosser, 2006)**.

3.3.2 Chemically synthesized CaF_2: combined WPPM/NMR analysis and TEM observations:

The study of chemically synthesized nanocrystalline CaF_2 provides further useful insights to separate size and lattice distortion effects in T_1 relaxometry. Co-precipitation in ethanol/water solution **(Wang, Fan, Pi, & Wang, 2005)** **(Omolfajr, Nasser, & Mahmood, 2011)** should yield fine fluorite nanocrystals with a low concentration of defects: this is verified either by the WPPM analysis, which suggests size broadening effects only (figure 3.7), and by TEM observations.

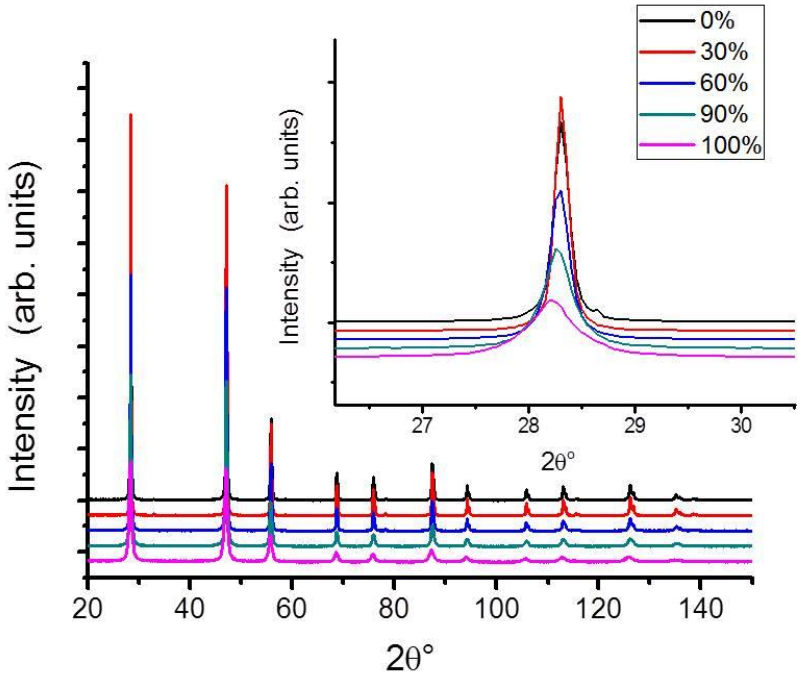

Figure 3.7 *XRD patterns for chemically synthesized fluorite in different solvent concentration (x=100%, 90%, 60%, 30%, 0% ethanol content, from below)*

- **Samples 0%, 30% and 60 %**

With a low ethanol content (x ranging from 0 to 60%), relatively large and faceted nanocrystals are formed, in a size range between 20 and 100 nm, with evidence of a minority fraction of very fine (<10nm) nanocrystals. T_1 values are in the range 5-8 s, and using a biexponential function to model the relaxometry data gives no better results than using a single exponential.

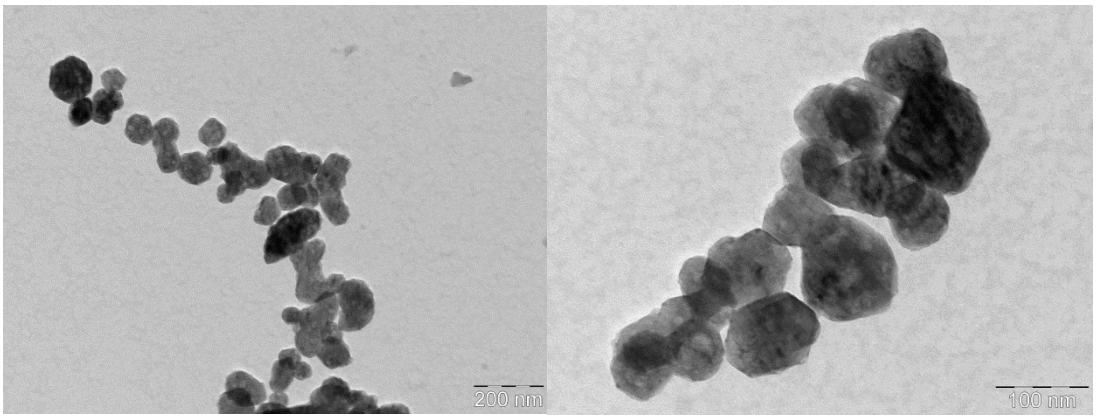

Figure 3.8 *TEM micrographs of CaF_2 synthesized in pure distilled water (x = 0%)*

The WPPM analysis of the x=0% sample, performed using one fluorite phase only as in a homogeneous sample, seems insufficient to obtain a good fit (WSS = 7730) and gives an average crystallite size of 17.9(12) nm. More importantly, the standard deviation is 13.8(9), which means a very wide size distribution. TEM gives a different result. As shown in **figure 3.8**, it is evident the presence of the particles larger particles, many of which appear as single (faceted) crystals, clearly larger than indicated by WPPM, with an additional fraction of much finer particles. According to this observation, two phases were used in the WPPM model, thus leading to a sensibly improved fitting quality (WSS = 6660). The average crystallite size is now 42(22) and 11(2) nm, for the larger and smaller size fractions, respectively (**figure 3.9**). The larger size is responsible for about 75 % of the diffraction signal, as resulted from a free parameter refined to model the relative intensity ratio of the two phases. Nonetheless, NMR relaxation fit does not show any improvement with a bi-exponential model. The best fit using mono-exponential function produces a T_1 of 4.9(2) sec with R^2 0.9965 (**figure 3.10**).

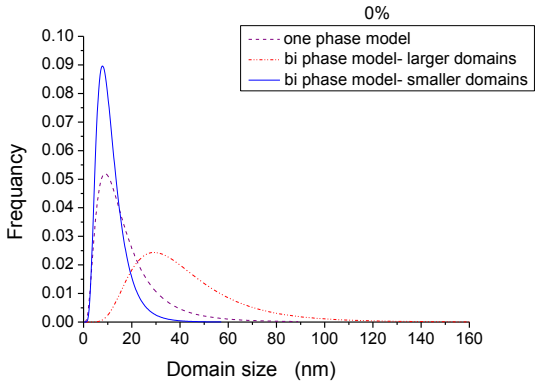

Figure 3.9 *Lognormal size distributions for 0% sample using one or two fractions in the WPPM*

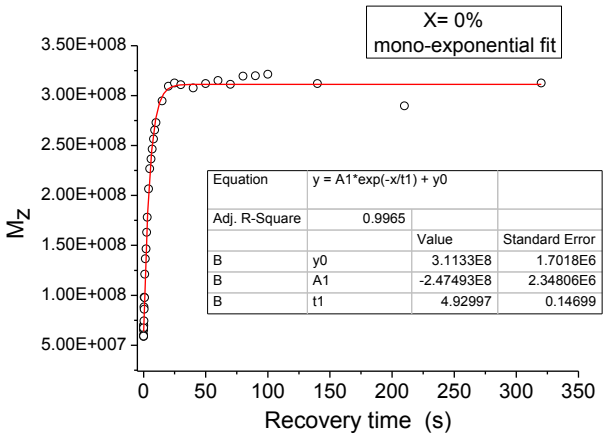

Figure 3.10 *NMR recovery signal fitted by mono-exponential function*

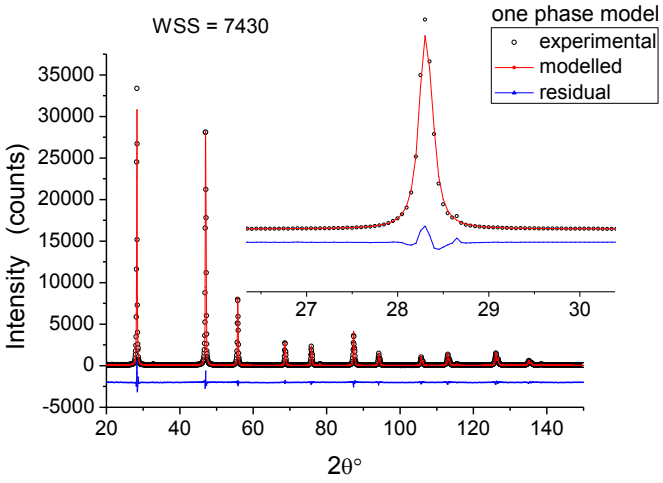

(a)

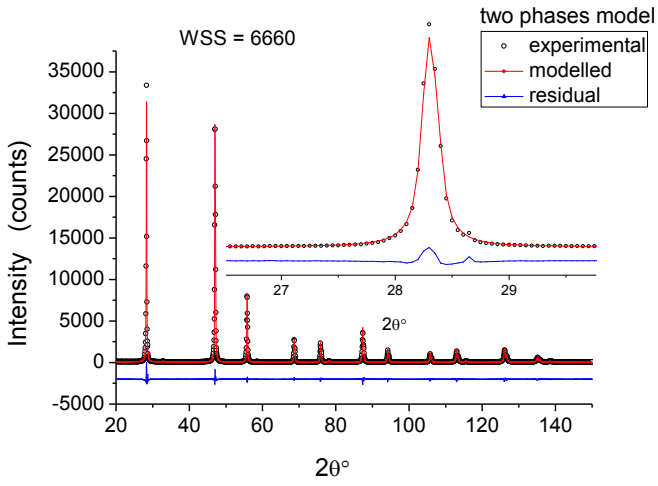

(b)

Figure 3.11 *WPPM results for 0% sample, using one (a) or two (b) fluorite fractions. Experimental (open circle) and model (line) with residual (line below)*

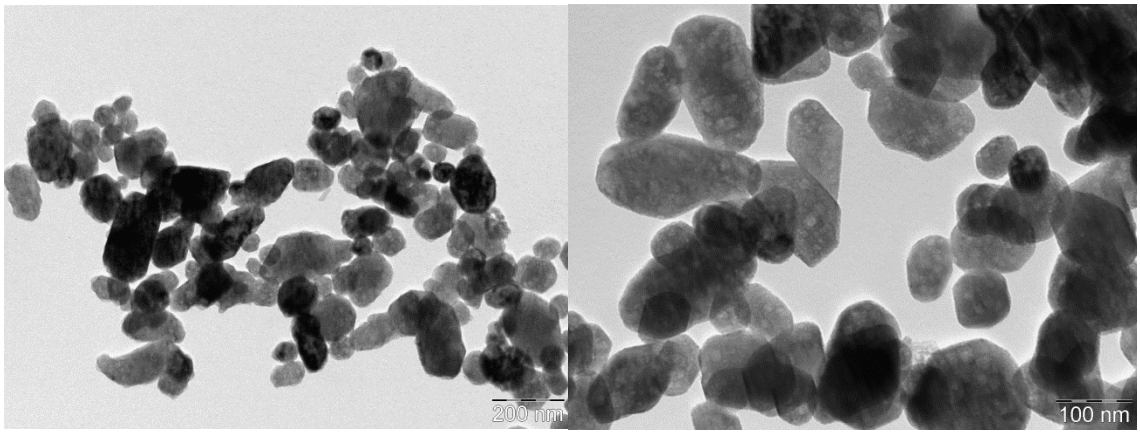

Figure 3.12 *TEM micrographs for CaF_2 synthesized in ethanol/water (x = 30%)*

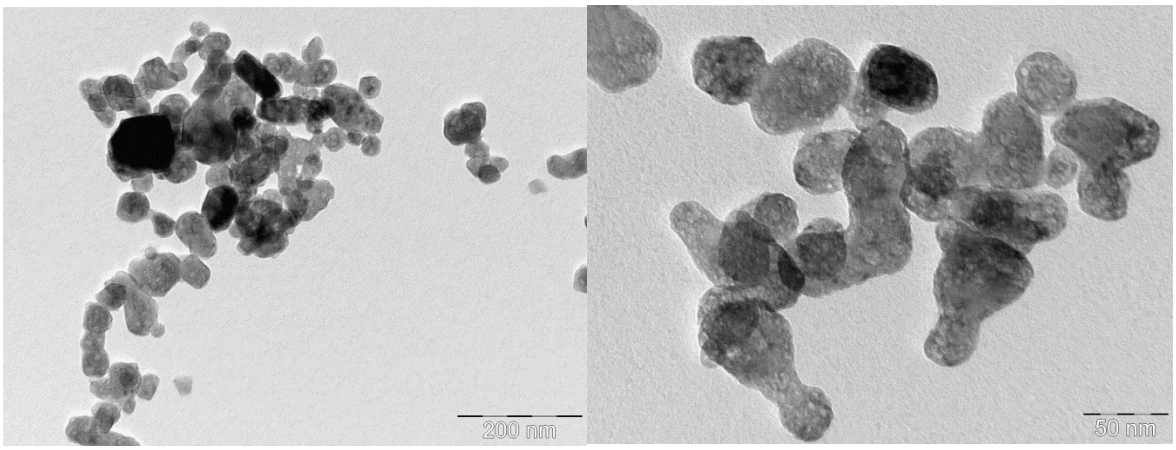

Figure 3.13 *TEM micrographs for CaF_2 synthesized in ethanol/water (x = 60%)*

TEM images for both x = 30% and 60% (**figures 3.12, 3.13**) show also a wide range of sizes, as in the x = 0 sample, therefore their corresponding powder diffraction patterns were analysed by WPPM using a two-phase model. For comparison with one phase WPPM, microstructural results for both conditions are tabulated in **table 3.2**. As an example of good quality fitting of NMR data, **figures 3.14** shows mono-exponential fitting for x=30% and 60%.

Table 3.2 *Main WPPM/NMR results for samples x= 0%, 30% and 60% with two fluorite fractions (left) or a single fluorite phase (right).*

X %		Lattice parameter (nm)	Avg. Domain size (nm)	WSS	percentage %		Lattice parameter (nm)	Avg. Domain size (nm)	WSS		T_1 (sec)
0	A	0.546593(4)	42(22)	6660	75		0.546614(3)	17.9(11)	7430		4.9(2)
	B	0.54671(2)	11(2)		25						
30	A	0.546527(2)	30(3)	5638	98		0.546514(2)	22.8(17)	5766		8.3(3)
	B	0.5496(1)	2(2)		2						
60	A	0.54666(1)	24(4)	4690	89		0.546683(4)	11.6(6)	5665		5.1(2)
	B	0.5471(1)	1.5(2)		11						

Estimated standard deviations, reported in parentheses, refer to the last significant digit

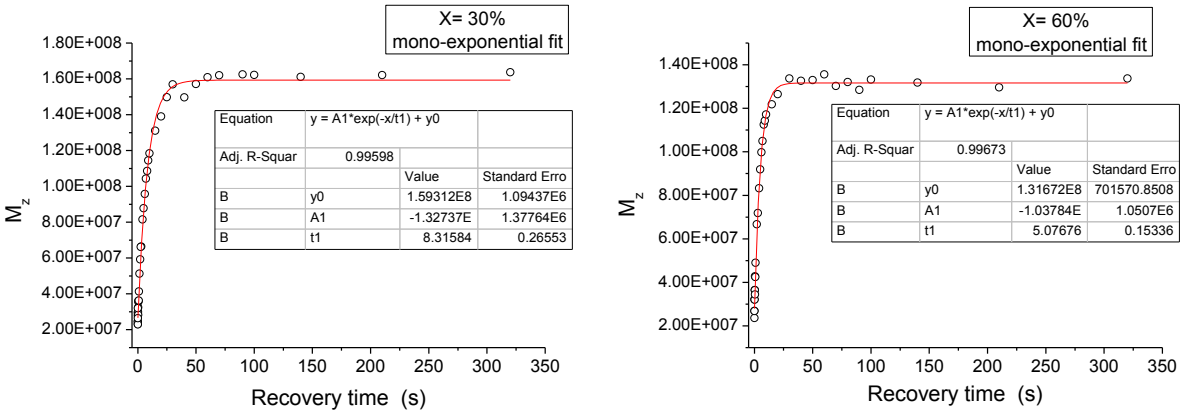

Figure 3.14 *Mono-exponential best fit of NMR data for x = 30% (left) x = 60% (right) samples*

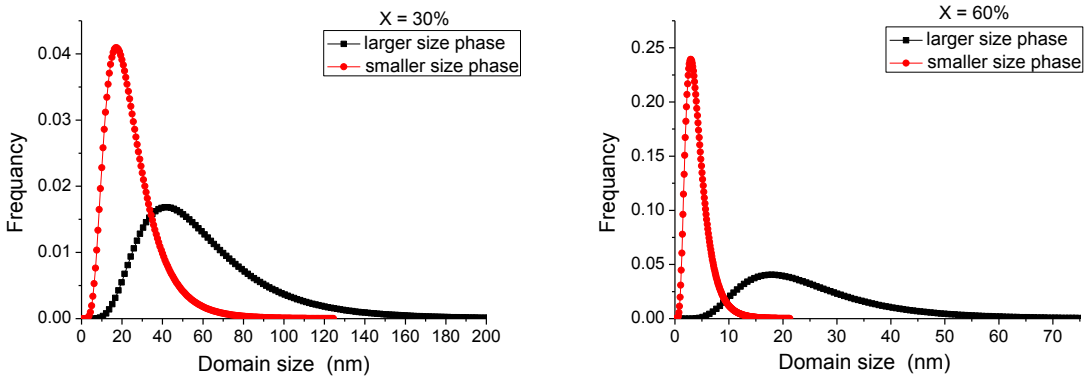

Figure 3.15 *Lognormal distributions of larger and smaller domains resulting from two-phase WPPM analysis for x=30% (left) and x=60% (right) samples*

- **Samples 90%, 100%**

For x = 90% and 100% (pure ethanol), the average domain size of the nanocrystals drops to about 10 nm and below, a feature also confirmed by TEM (**Figure 3.16**). The x = 90% sample is mostly made of crystals which, according to WPPM, are about 13(2) nm (standard deviation 7(1) nm), i.e., as small as fluorite powders ground for 16 or more hours; same size but, quite evidently, absence of lattice defects. The x = 90% sample is then an ideal case of study to compare size effects alone with size + dislocation effect, with the latter typical of the ball milled powders. As a comparison with a ball milled powder, the lognormal size distributions provided by the WPPM analysis of two samples, chemically synthesized with x=90% and ball milled for 64 h, are shown in **figure 3.17.** It is interesting to note that the two distributions are quite similar – same domain sizes – even if the two samples have drastically different content of lattice defects. NMR relaxometry for the x = 90% sample (**Figure 3.18**) gives a much longer T_1 of 5.7(2) s, as compared with the T_1 varying from 0.3 to 0.8 s for powders ground 16 h and longer. Based on this, if domain size effects are important in decreasing T_1 of fluorite, they seem not as effective as dislocations. The steep decrease of T_1 with the milling time depicted in **Figure 3.6** can then be ascribed to a high density of dislocations (10^{16} m^{-2} and more) in a homogeneously ground fluorite phase.

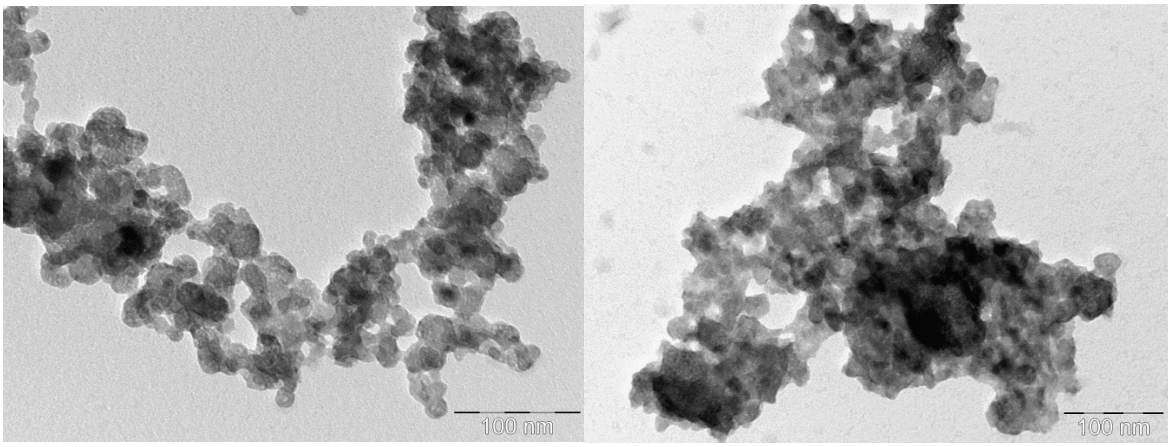

(a) (b)

Figure 3.16 *Agglomerated fine particles from TEM images of CaF_2 synthesized in a) ethanol/water (x = 90%), b) in pure ethanol (x=100%)*

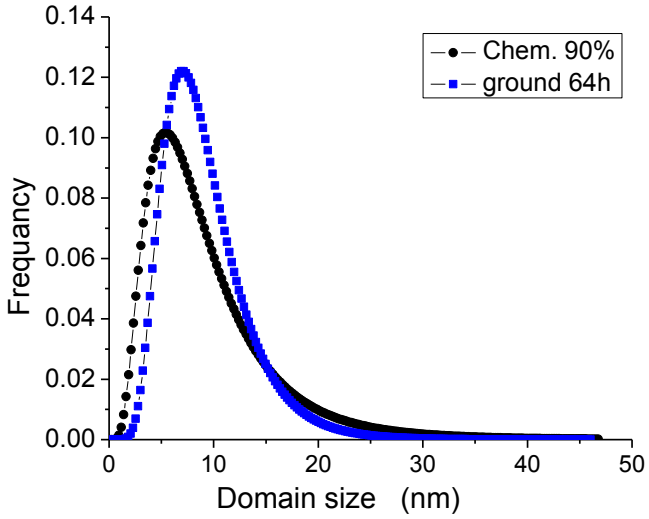

Figure 3.17 *Comparison between lognormal size distribution for 90% ethanol (chemically synthesized) and 64h (ball milled) fluorite samples*

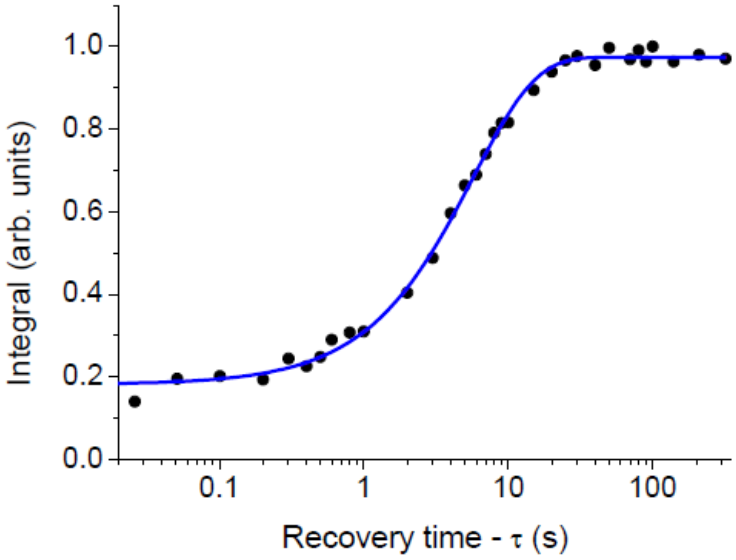

Figure 3.18 *Extracted relaxation data for the x = 90% co-precipitated nanocrystalline fluorite. The line is the best fit using a monoexponential fit*

Domain sizes down to 12-13 nm (in clusters of agglomerated nanoparticles) seem to give a lesser contribution to depress T_1. The spin-lattice relaxation, which in ionic crystals is known to be related to the interaction of the nuclear quadrupole moment with the fluctuations in the local electric

field gradient **(van Kranendonk, 1954)**, is deeply affected by the strain field of the dislocations, with T_1 decreasing as an effect of the creation of additional relaxation channels **(Scholz, Dorfel, Heidemann, Feist, & Stosser, 2006)**.

The sample prepared in pure ethanol (x = 100%) is also interesting, as it gives a rather short T_1 of 0.46(1) s. TEM micrographs (e.g. **figure 3.16b**) show fine, variously agglomerated nanoparticles which the XRD-WPPM analysis quantifies as equiaxed domains with a mean diameter of 6.2(2) nm and a relatively narrow distribution (standard deviation 3.7(1) nm). As an important difference with respect to all other (chemically synthesised and ball milled) fluorite samples, the ^{19}F MAS NMR spectrum of the x = 100% sample (**Figure 3.19**) shows a small additional resonance at a chemical shift of ca. -30 ppm. This feature has been already observed in the literature, and attributed to the presence of a vacancy-interstitial pair (Frenkel defect) on the cubo-octahedral interstitial site in the unit cell **(Jain P. , Kim, Youngman, & Sen, 2010)**.

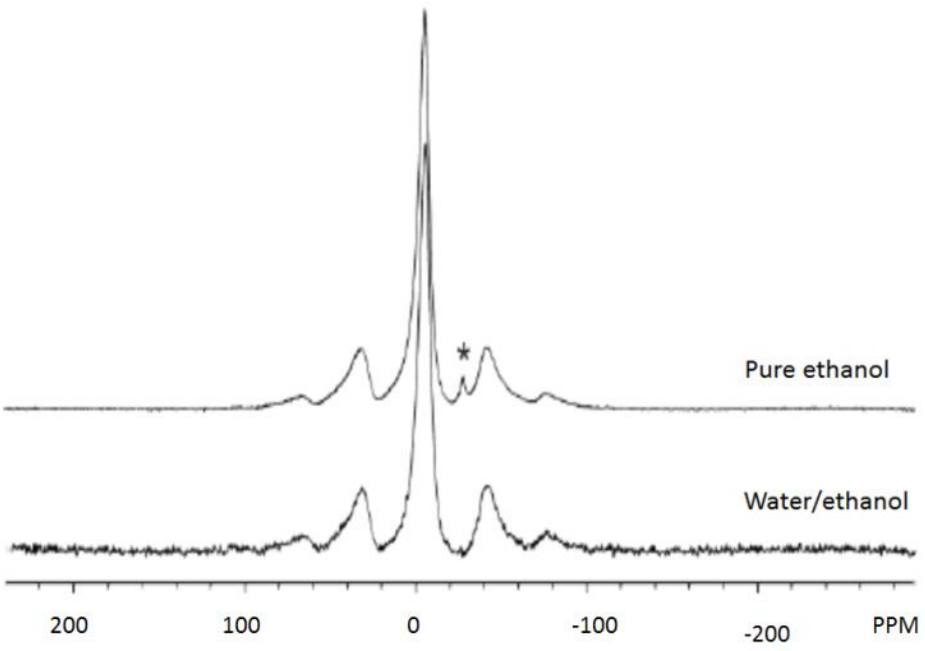

Figure 3.19 *^{19}F MAS spectra of chemically synthesized fluorite powders with x = 90% (below) and x = 100% (pure ethanol, above)*

The small size and, especially, the occurrence of Frenkel defects are clearly related to the strong decrease of T_1. Like in the dislocation-rich ball milled powders, this is also an effect of lattice distortion. In fact, the vacancy-interstitial pairs bring along an intense local strain field, and a general expansion of the crystal lattice. The latter feature is confirmed by the average unit cell

parameter, which is 0.54764(1) nm for the x = 100% sample, as compared to values around 0.5465 nm for the water/ethanol preparations (**figure 3.20**).

We might further speculate on the reason for the presence of Frenkel defects in the x = 100% sample only. Besides the different chemical environment, this could be most likely related to the small domain size yielded by co-precipitation in pure ethanol: as the Frenkel defects are most favourably hosted by the surface region **(Ruprecht, Wilkening, Steuernagel, & Heitjans, 2008)**, their concentration might become relevant for very small domain sizes only. Chemical synthesis in water/ethanol does not lead to sizes smaller than 10-12 nm, and also with ball milling, even for the most extensive treatment (64 h), domain sizes saturate to 12-13 nm, as an effect of the self-annealing process typical of high energy grinding **(Koch, 1997)**.

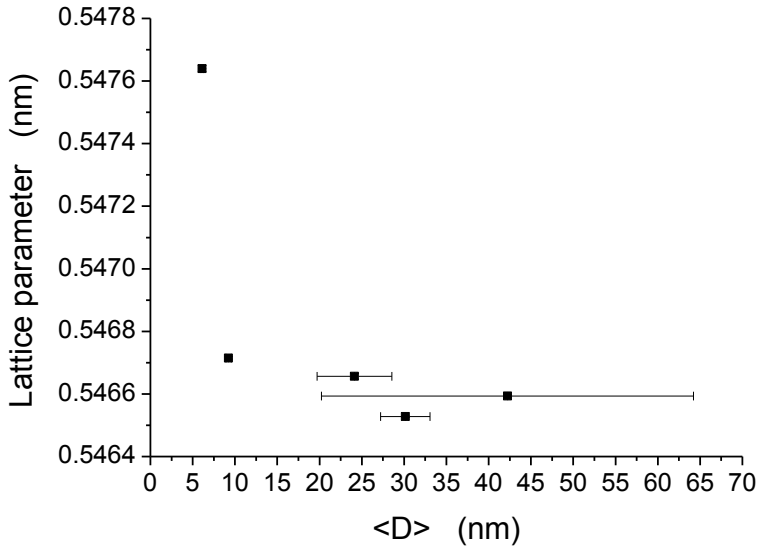

Figure 3.20 *Evolution of unit cell parameter with average domain size for chemically synthesized fluorite*

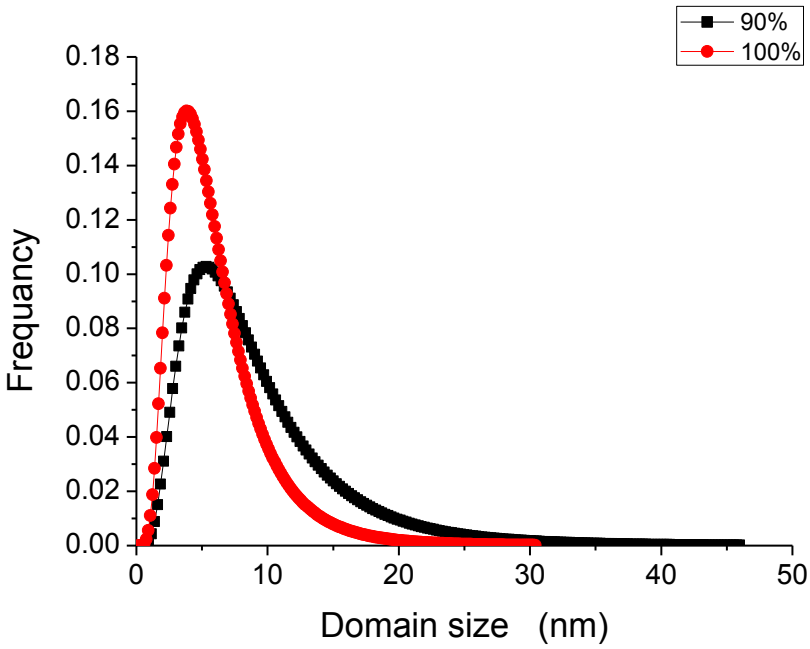

Figure 3.21 *Size distribution for nanocrystalline fluorite obtained by co-precipitation in x = 90% and 100% ethanol solutions*

These results show that the size effect alone only can reduce the relaxation time down to the range of seconds (5-8 s in samples prepared in water/ethanol). Any further decrease has to be related to the influence of distortions present in the lattice, e.g. dislocations present in the crystal structure. This interpretation is confirmed by the very low T_1 found for the sample produced in pure ethanol and hosting Frenkel defects leading to a drop of T1 down to 0.46(1) s (**figure 3.22**). Moreover, the explanation is also consistent with the ball-milling results, where only the phases characterized by a high defect concentration and a small mean domain size reveal relaxation times below one second. For samples milled 16 h and longer, only a further increase of the dislocation density can lead to an additional reduction of the relaxation times, while the mean domain size is not further affected by milling. In other words, the influence of the dislocations causes a further decrease down to some tenths of a second, e.g. 0.31 s for the sample milled for 64 h.

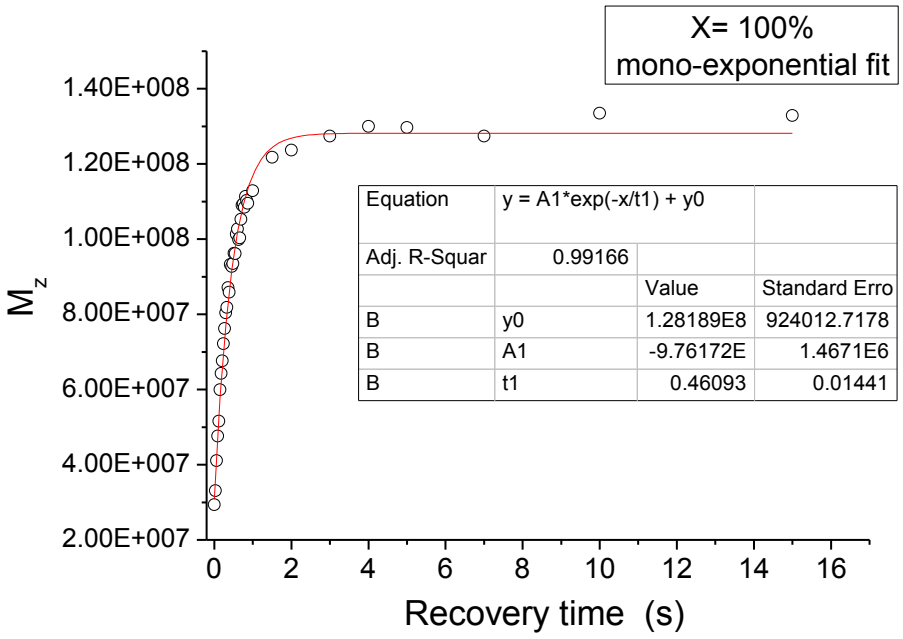

Figure 3.22 *Mono-exponential best fit of NMR data for the x = 100% sample*

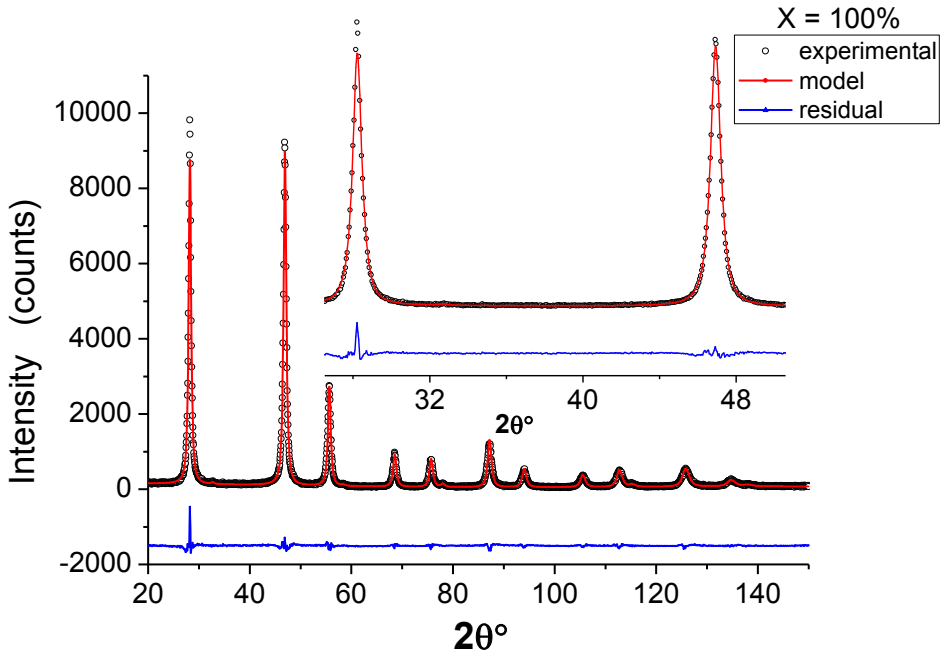

Figure 3.23 *WPPM of x =100% sample (one phase). Experimental (open circle) and model (line) with residual (line below)*

Table 3.3 *Main results of WPPM and NMR relaxometry for sample 90% and 100%.*

X %	Lattice parameter (nm)	<D> (nm)	T_1 (sec)
90	0.54671(1)	9.2(3)	5.7(2)
100	0.54764(1)	6.1(2)	0.46(1)

Estimated standard deviations, reported in parentheses, refer to the last significant digit

Finally, it is also worth noting that the influence of the homogeneously distributed iron, as discussed in recent study **(Abdellatief, Abele, Leoni, & Scardi, 2013)**, can strongly reduce the relaxation times by up to another order of magnitude (e.g. 0.036 s for samples ground in steel vials for 64 h).

3.4 Conclusions

High energy ball milling of fluorite leads to a finely divided phase with a strong lattice distortion caused by dislocations. Although this final result is common to most mechanical grinding procedures, the evolution is not straightforward: during the early stages of milling the powder is inhomogeneous, as it contains grains which experienced a quite different degree of damaging. Neither the state of the art X-ray Powder diffraction LPA methods - such as the Whole Powder Pattern Modelling – nor electron microscopy alone are able to give a detailed picture of the powder.

Solid State NMR T_1 relaxometry can indeed provide information on the homogeneity of the ground powder. Under the assumption that the ball milled powder can be considered as made of two fractions – one lightly affected by grinding, the other strongly deformed and reduced to nanometre size – T_1 relaxometry data support a modelling with a biexponential function, providing two different T_1 values for the two fluorite fractions.

Combined XRD / NMR T_1 relaxometry analysis is a robust tool for a quantitative description of the effects of high energy grinding on the microstructure of fluorite. While the domain size decreases and dislocation density increases with ball milling time, T_1 strongly decreases. This feature is much sensitive to the grinding environment: same effects are observed in fluorite ground

in steel vials, but the paramagnetic contribution of iron shifts downward all T_1 values by one order of magnitude (this might be a useful comment / distinction with respect to chapter two studies)

The comparison of the milled powder with an analogous nanocrystalline powder free of defects showed univocally that dislocations are the main responsible for the reduction of T_1; domain size is less effective in this. Point defects, present in fluorite in the prevailing form of Frenkel defects, have an influence on the NMR signal as well. In agreement with the literature, they give a clear, distinctive signal in the solid state ^{19}F MAS NMR spectrum that can be identified in powder produced by water-free soft chemistry, but that are neither present in the mechanically ground fluorite, nor in samples obtained in water-ethanol solution.

CHAPTER IV

In-Situ X-Ray Diffraction Furnace at MCX Beamline

M. Abdellatief, A. Lausi, J.R. Plaisier, P. Scardi, J. Macleod, X. Santarelli, G. Zerauschek

Abstract

The instrumental and technical set-up of the MCX beamline at ELETTRA synchrotron designed for powder diffraction applications will be presented. At MCX a furnace was developed for real time in-situ x-ray diffraction (XRD) and small angle x-ray scattering (SAXS) experiments for powders and thin films. The design and characterization of the furnace are discussed in this chapter.

4.1 Introduction

In many scientific and engineering areas, investigations into fast reactions and crystallographic phase transitions in materials by in–situ X-ray diffraction (XRD) serve a wide range of applications. For example, kinetics and grain growth **(Kirsch, Richman, Riley, & Tolbert, 2004)** mechanisms are very interesting for catalytic and dynamic applications (Morcrette, et al., 2002). Many materials show structural phase transitions at high temperatures and consequently altered properties **(Maehlen, et al., 2007)**. In-Situ XRD is a non-destructive and effective tool to follow the progress in materials' microstructure features in real time and temperature at various non-ambient experimental conditions **(James, Scates, & Martyn, 2003)**. It can be used as a complementary technique for thermal analysis tools like thermo-gravimetric, differential scanning calorimetry, etc., when studying phase transitions.

The beamline MCX at the synchrotron facility at Trieste is designed for diffraction experiments on polycrystalline materials in general. A wide variety of applications of powder diffraction is possible (e.g. GIXD, residual stress, etc.) in both transmission and reflection geometry. However, as the diffracted intensities are measured using a point detector, this set-up is not suited for kinetic studies. In order to cover the field of the in-situ real-time XRD experiments a furnace was developed. The furnace uses a translating Image Plate (IP) detector and provides two modes of XRD experiments: step scan and continuous scan. The step scan allows the collection of a large number of patterns on the same IP with a maximum of about 60 patterns. In a continuous scan the diffraction is measured without interruption, while heating the sample. A user friendly program interface has been developed, which allows users not only to program their experiment, but also to monitor each running step of the in-situ experiments. The furnace heating element is a high resistance wire, wrapped around an alumina tube. The temperature is controlled by a Proportional Integration Differentiation PID controller with a small temperature tolerance.

This chapter is divided in two parts. In the first part a general description of the beamline MCX will be presented. In the second part the oven design, alignment procedures and temperature calibration will be described.

4.2 MCX Beamline

The Materials Characterization by X-ray diffraction (MCX) beamline at the Italian national synchrotron radiation facility ELETTRA in Trieste was designed to perform a wide range of powder diffraction experiments. **Figure 4.1** shows a schematic representation of MCX. The source of MCX is a bending magnet with a field of 1.2 Tesla when the operating energy of the storage ring is 2 GeV and 1.45 Tesla when the ring energy is 2.4 GeV **(Lausi, Busetto, Leoni, & Scardi, 2006)**. The flux at the experimental station was calculated theoretically by Code Shadow program to be more than 10^{11} photons/sec at a wavelength of 1Å (**figure 4.2**). The beamline is divided in three parts: front end, optical and experimental hutch and each of them deal with specific tasks.

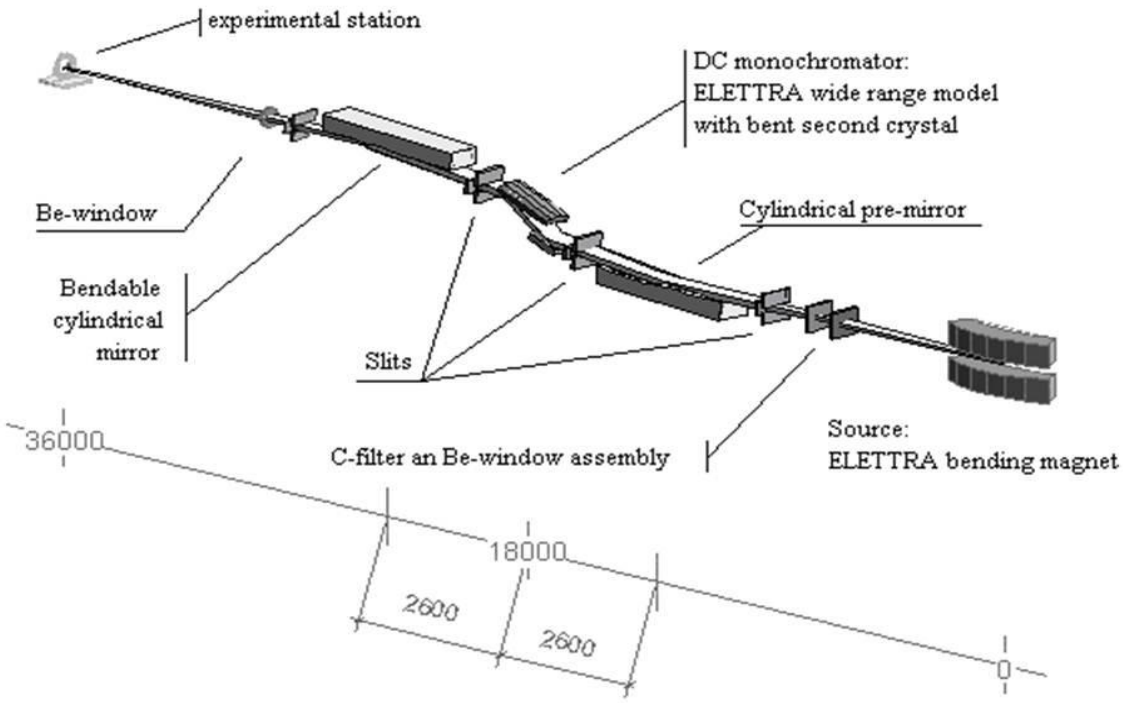

Figure 4.1 *Schematic representation of MCX beamline at ELETTRA*

In the first part, just before the front end hutch (**figure 4.3.a**), a water cooled shutter-stopper is located directly after the storage ring exit. Inside the hutch a set of apertures is placed to define the beam vertical and horizontal aperture to about 6 mrad, for a total power of about 70 W.

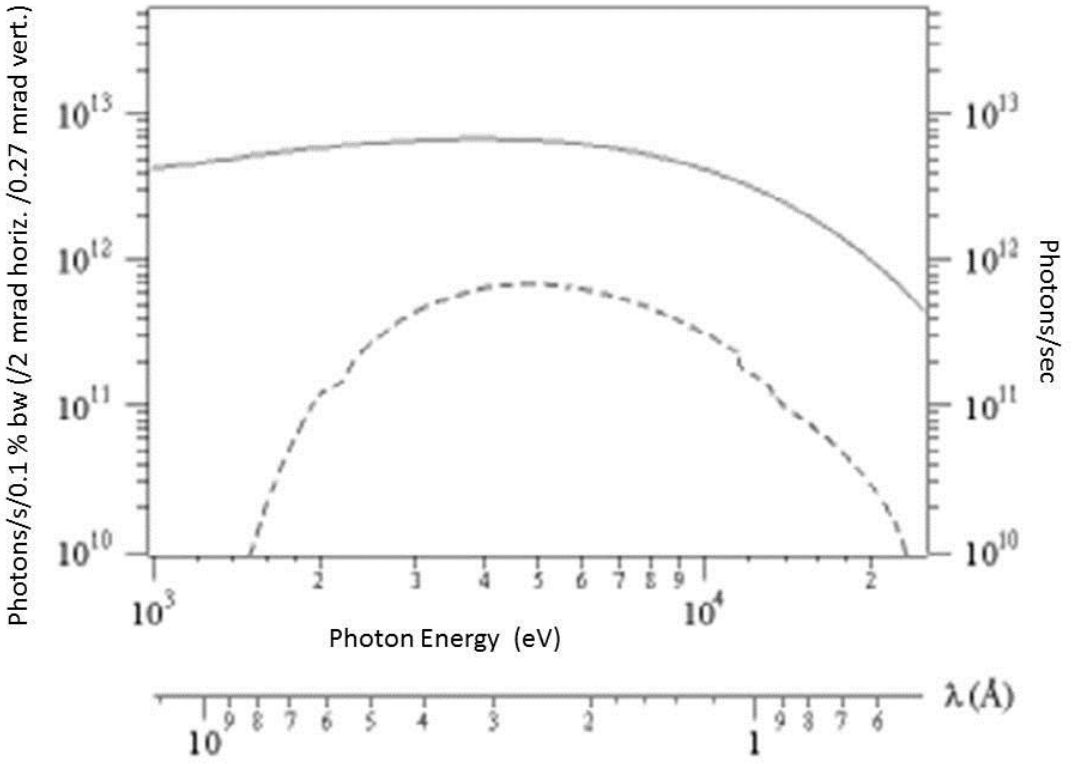

Figure 4.2 *Calculated source brilliance and flux of MCX beamline*

The front end hutch is followed by the optical hutch (**figure 4.3.b)** which contains the instruments dealing with beam focusing and energy selection. The first focusing object is a 80 mm wide and 1.2 m long flat Si blank -Pt coated- Mirror. It is positioned face up and has a bending mechanism that allows changing the tangential radius between 5 and 16 km for vertical collimation of the incoming beam. After that, a double Si crystal (111) monochromator allows to select the energy by changing the diffraction angle of the first crystal according to Bragg's law. At the first Si crystal, the beam is diffracted upwards and therefore a second Si crystal is oriented parallel to the first crystal in order to bring the beam again to a horizontal path, shifted up about 7cm. The Si second crystal is bendable for horizontal focusing and it has additional degrees of freedom. The translation, rotation (independent from the first crystal), yaw, roll and pitch movements are all tuned together to provide a focused beam. Afterwards, the second mirror is placed face down. This mirror is bendable and its radius can be changed in order to produce either a parallel beam or a beam focused vertically on the

experiment. The optical hutch ends with a fast valve and a stopper that has to be closed when the experimental hutch is open for preparing the measurements.

In the experimental hutch (**figure 4.3.c**) a beryllium window separates the high vacuum part of the beamline (pressure around 10^{-8} mbar) from the low vacuum part (around 1 mbar). Between the window and the experiment three instruments are located. A set of slits are mounted to control the beam size at the experiment. The intensity of the incoming beam of the experiment is monitored by an ionization chamber, and finally, there is a filter holder containing several aluminum sheets, which can be inserted in the beam, when it is necessary to attenuate the photon flux.

For the X-ray diffraction experiments a high-precision 4-Circle Huber goniometer is installed (0.0001^o 2θ accuracy). The experiments can be performed using capillaries in Debye-Scherrer geometry or with flat samples using Bragg-Brentano geometry. For both flat samples and capillaries spinners are available, that allow to rotate the sample during the measurement to improve statistics. The experimental setup for flat samples furthermore allows controlled 360^o Φ-rotation, $\pm 90^o$ χ tilting and x-y-z movements. In order to measure the diffraction intensities the two-theta arm is equipped with a high count-rate scintillation detector. Before the detector a set of slits and optionally a Si 111 analyzer crystal are located. As an alternative detector, a multi-channel analyzer is available. This detector has a lower dynamic range, but allows counting of photons of a specified energy range (e.g. to eliminate background originating from fluorescence of the sample).

The main experiments performed at MCX using the 4- circle goniometer are:

- Standard powder diffraction applications for phase analysis or (micro-)structure determination (flat plate – capillary)
- Powder diffraction in non-ambient conditions (controlled cooling to 100K using a cryo-cooler and controlled heating by a blower up to 1000 ^{o}C with 10 ^{o}C /min rate
- Residual stress and texture analysis (mechanical applications)
- Grazing angle and reflectivity (thin films)

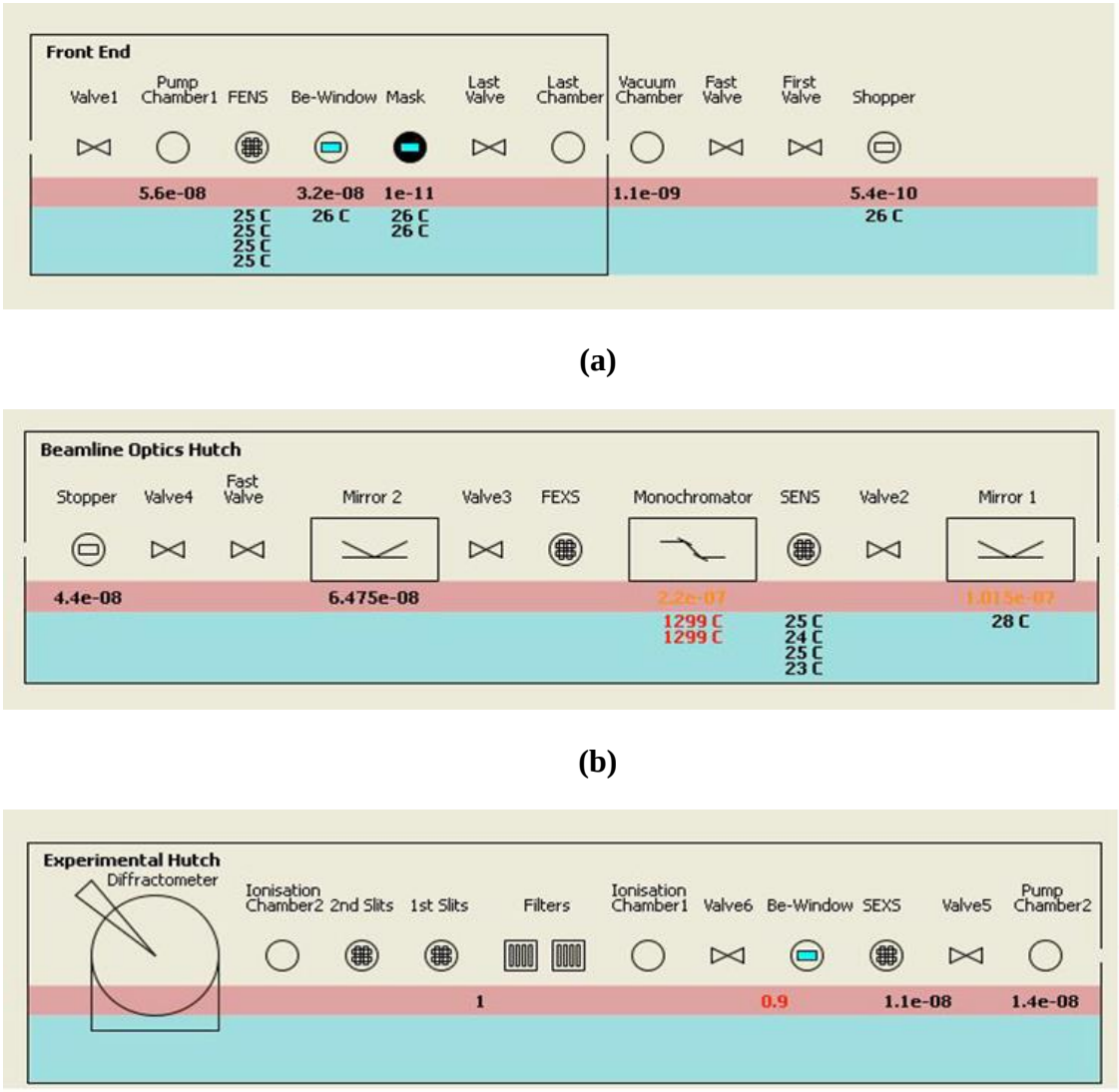

Figure 4.3 *MCX beamline: a) front end hutch, b) optical hutch and c) experimental hutch*

It is a well-known fact, that proper analysis of XRD patterns requires an elementary knowledge of the instrumental contribution in line profiles. For the instrumental profile, a diffraction pattern of Silicon standard NIST SRM 640a was measured at different energies and the peaks were fitted to the pseudo-Voigt function. Caglioti functions **(Caglioti, Paoletti, & Ricci, 1958)** for FWHM (**equation 4.1**) and η (**equation 4.2)** were analyzed for Si standard collected at 10 (**figure 4.4**) and

18 keV (1.241Å and 0.689Å respectively). The refined values of the peak positions, FWHM, and the asymmetry factor η were obtained. The FWHM (**figure 4.5**) was below 0.04° over a wide range of 2θ coupled with a negligible asymmetrical contribution (**figure 4.6**) due to the instrument.

$$FWHM^2 = W + V \tan(\theta) + U \tan^2(\theta) \quad (\mathbf{4.1})$$

;FWHM is the full width at half maximum. W, V and U are the second order equation's coefficients. θ is the Brag angles for each peak.

$$\eta_{Lorentz} = a + b\,\theta + c\,\theta^2 \quad (\mathbf{4.2})$$

; a, b and c are the second order equation's coefficients

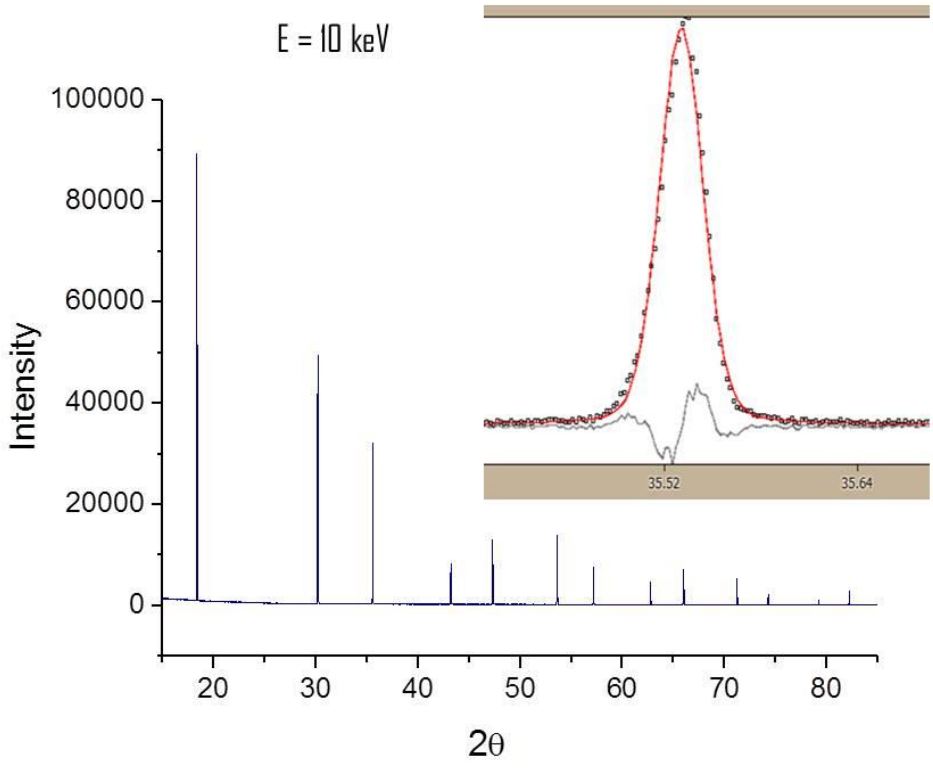

Figure 4.4 *Silicon standard pattern at 10 keV*

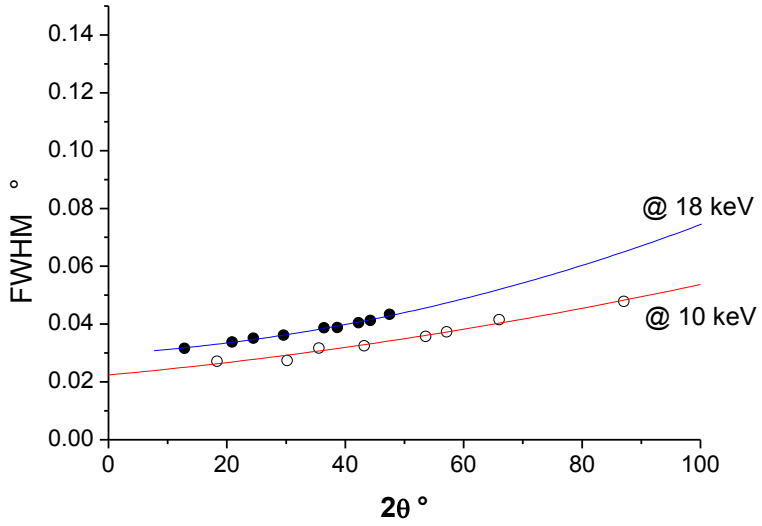

Figure 4.5 *The FWHM-2θ dependence obtained by Silicon standard at MCX at 10 and 18 keV*

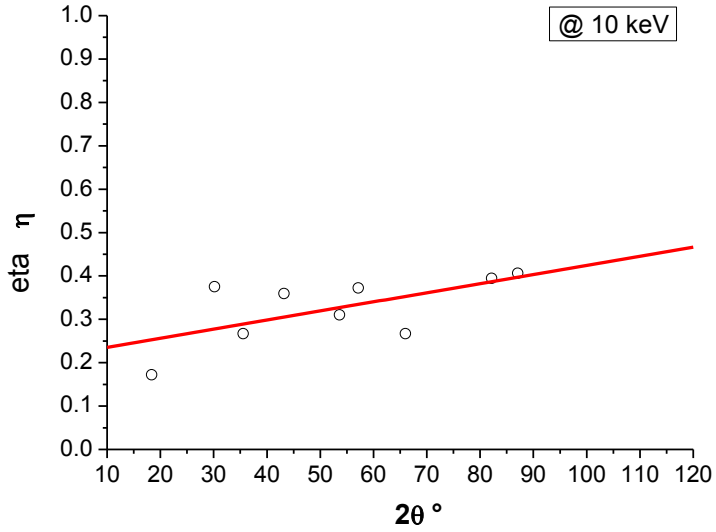

Figure 4.6 *The contribution of peak asymmetry with 2θ dependence*

4.3 Design of the furnace for in situ XRD experiments

In order to study dynamic processes as a function of temperature under non-ambient conditions at MCX, a furnace was developed for in-Situ XRD experiments **(Riello, Lausi, Macleod, & Plaisier, 2013)**. The design of the furnace was constructed in such way to be able to either collect many patterns rapidly or to measure the diffraction continuously during heating. Capillaries and thin film samples are allowed. Furthermore, heating up to 1000°C is available and there is a possibility for a gas flow through sample in capillary.

Figure 4.7 shows an image and a schematic design of the furnace. The furnace is divided into four main parts. The first part is the entrance of the X-ray beam. The second part is the hot room in which the heating elements are located. The third component, a cold room, houses the sample holder and gas flow system. Finally, the last part is an imaging plate IP holder with a magnetic bed used to fix the IP at its position. The oven components and table are very heavy to limit the vibrational movement thereby increasing the furnace's mechanical stability.

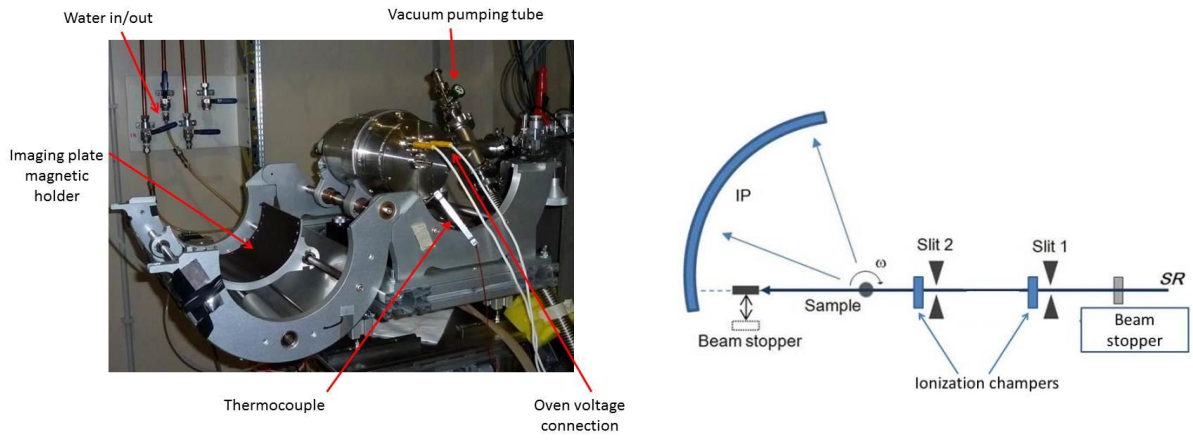

Figure 4.7 *The real time/high temperature oven*

The first part of the furnace contains the entrance path of the photons. In this part a shutter is positioned in front of two fixed slits each of which is followed by an ionization chamber. The objective of the slits is to control the beam size. The vertical and horizontal apertures of the slits are

controlled by Huber series 3000 slit screen system. The ionization chambers are essential in the final alignment as discussed below and to record the intensity of the incoming beam.

The second part of the furnace, the hot room, houses the diffraction experiment. It is a cylindrical vacuum chamber (**figure 4.8**) of stainless steel with Kapton windows for the beam entrance and exit. The entrance has a circular shape while the exit is a fixed slit about 1 mm wide covering up to 140° 2θ. A beam stopper is fixed inside the vacuum chamber and it protects the IP from being damaged by the direct beam. The furnace heating element is an Alumina tube with a resistive Kanthal wire connected to a high voltage power supply. The oven tube has either a zigzag wrapping mode or spiral wrapping mode as shown in **figure 4.9**. The zigzag wrapping provides a null magnetic field at the sample however it is difficult to prepare therefore the spiral wrapping oven is preferable due to its relative simple preparation. The alumina tube has an aperture that allows the incoming and diffracted x-rays to pass. The temperature of the sample is measured by a thermocouple of K-type fixed from the hot room side and thoroughly fixed to reach the sample from beneath.

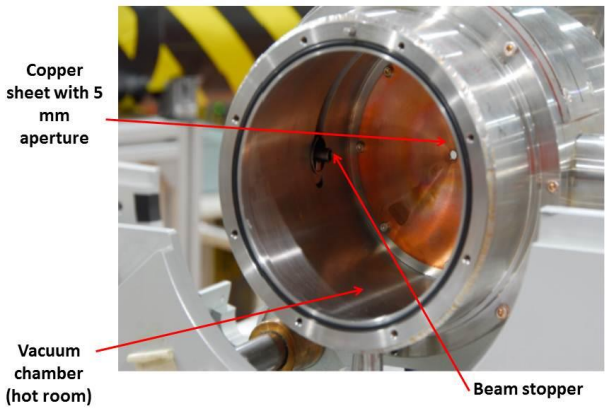

Figure 4.8 *Side view for the cylindrical chamber from the hot room side*

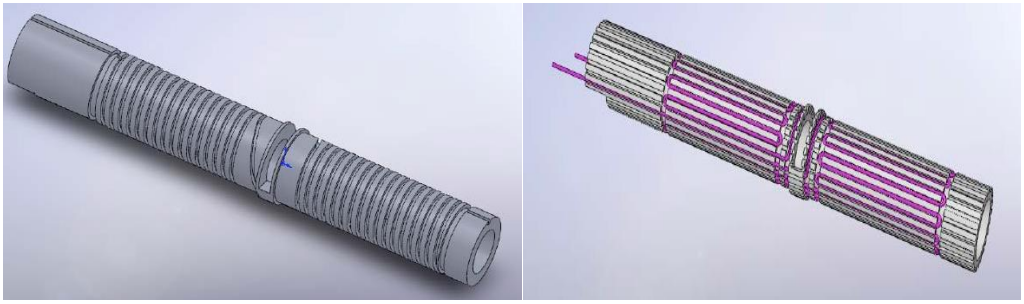

Figure 4.9 *Oven with spiral wrapping (left) and with zigzag wrapping right*

A water flow circuit is placed around the hot room to prevent heat to reach to the outer metallic surface of the furnace and consequently protecting the IP from the heat radiation that could result in a loss of recorded intensity at the IP after some time. Experiments in the oven are operated under vacuum of about 10^{-3} bar for two reasons; firstly to decrease the air scattering and secondly to protect the oven from oxidation that could occur when it is heated up at elevated temperatures. A copper diaphragm divides the cylindrical chamber separating the hot and cold rooms, stopping the heat from reaching the cold room. The diaphragm has a 5 mm aperture in its center which allows the sample to enter the furnace from the cold room.

The cold room houses the sample holder, which is a goniometer head especially designed to allow gas flow in capillaries. The goniometer head, shown in **figure 4.10**, is capable of hosting different size capillaries from 0.01 mm to 2 mm diameter. The goniometer is connected to a spinner that provides 90° spinning in order to increase statistics. Two soft Teflon hoses are connected to the goniometer head. Gas flow is achieved through the sample via a double capillary configuration (**figure 4.11**). The inner capillary with smaller size (usually less than or equal to 0.5 mm diameter) contains the investigated specimen while the outer capillary acts as a closed reactor (with 2 mm diameter). The double capillary model is used instead of one capillary gas flow. It was observed in one capillary gas flow experiments that the gas does not flow completely into the sample due to the powder compaction. Consequently, gas enters and exits directly without penetrating the powder. In the double capillary gas flow model this problem is solved by breaking gently the top of the inner capillary to drive the gas to pass through the sample. The gas then exits through the outer capillary. Quartz wool is put on the top of the inner capillary in order to avoid the loss of powder by gas flow pressure. Various gas flow rates are available giving the possibility to reach slow or high flow rates. The double capillary system in such case behaves as a reactor for controlled temperature and pressure at non ambient atmosphere.

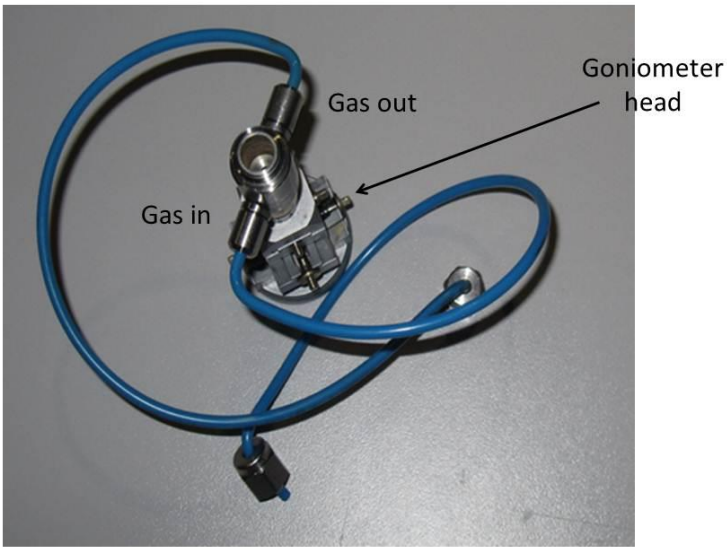

Figure 4.10 *Goniometer head with gas flow connectors*

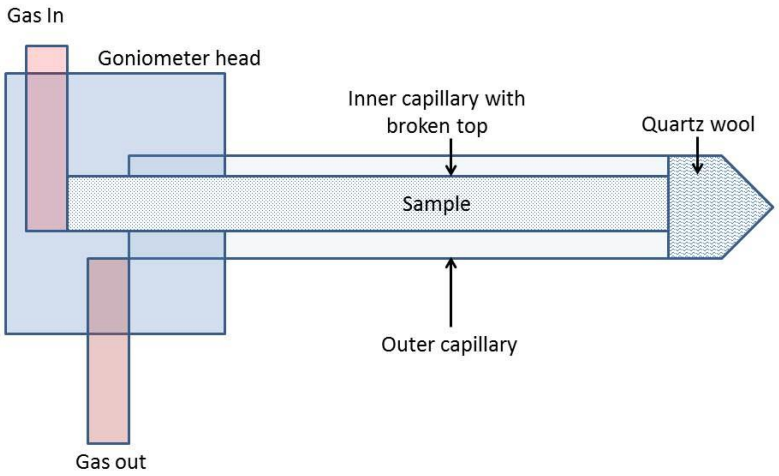

Figure 4.11 *Schematic representation for double capillaries gas flow model*

An alternative way to perform in-situ XRD by the oven is the thin film holder. In this case, little sample tilt is required for the grazing angle diffraction without sample spinning. For thin film samples it is not possible to measure under gas flow.

The fourth part is the translating IP holder, which is a magnetic and translating curved holder that supports an imaging plate that allows recording one or more diffraction patterns on the same image. The imaging plate is fixed in such a way that a diffraction pattern with a total range of about 130° 2θ can be measured. The IP (Fujifilm BAS-IP SR 2025) records and stores diffracted X-ray intensity by a photo- phosphoric mechanism. The stored image is then read by a Fujifilm FLA-7000 scanner. The scanner program offers several resolution choices. The maximum resolution is 25µm for each pixel. Then the scanned two dimensional (2D) images can be analyzed by free programs available on the international web. The Fit2D program is one of them; it is used to convert the image into 1D patterns of intensity vs. pixels. A conversion is then required from pixels axis into 2θ axis, which is discussed below.

4.4 Alignment of the furnace

Before any measurement can be performed the furnace has to be aligned very carefully to obtain the best possible results. Preliminary alignment is done outside the experimental hutch followed by a final alignment using the beam. In the preliminary alignment, slits, oven tube, capillary and the hot chamber gap must be perfectly aligned before moving the oven inside the experimental hutch for the final precise alignment. The oven aperture has to be aligned with the beam stopper and with the exit gap in front of the imaging plate to avoid any diffraction from the oven. An aligned oven aperture is schematically presented in **figure 4.12** captured from the beam entrance side.

Alignment of the oven with the beam is then performed by maximizing the current read by the ionization chambers by adjusting the oven's vertical and horizontal positions (**figure 4.13**).

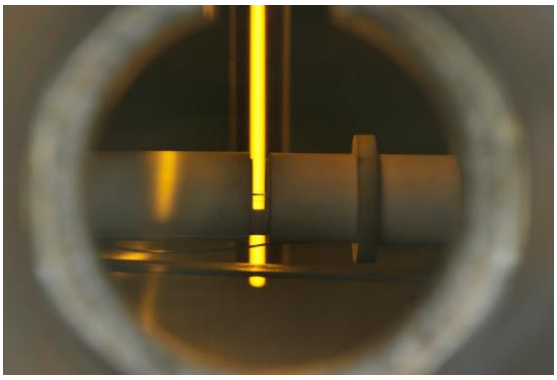

[5]**Figure 4.12** *Side view of aligned oven gap, capillary and exit slot captured from the beam entrance direction.*

[5] Figure reference: Xenja Santarelli thesis, university of Trieste Italy, 2010

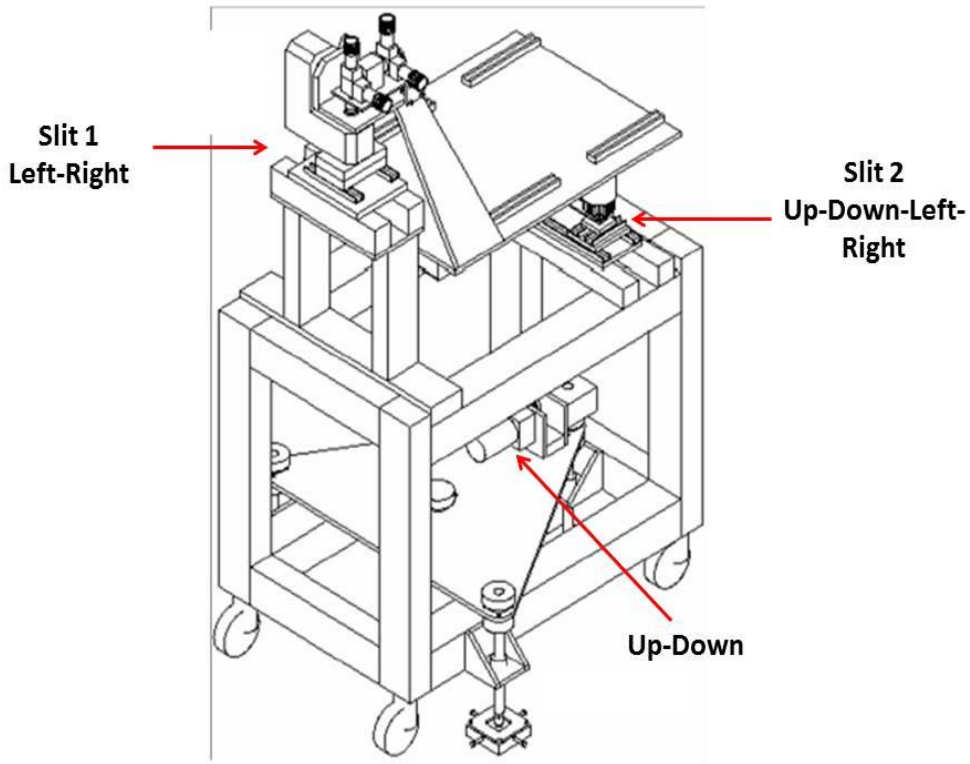

Figure 4.13 *Schematic representation of the oven table with fixed two slits and two ionization chambers*

4.5 Oven program control

LabView (National Instruments) was used to control various aspects of the measurements through a simple interface. LabView provides the communication with different electrical components and power supplies as shown schematically in **figure 4.14**. The oven program is composed of several panels from which the users utilizes mostly the 'user parameters' panel (**figure 4.15**) to define heating rate, waiting time, exposure time, IP displacement and experiment mode (In-Situ continuous or step scan XRD).

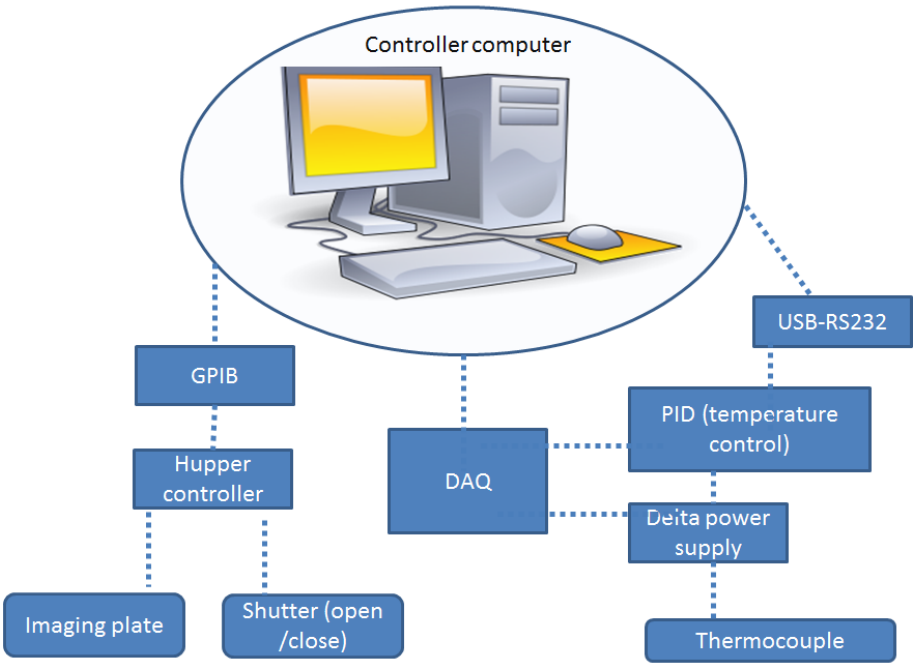

Figure 4.14 *Main programmed components of the oven*

An example of each scan mode (continuous and/or step) is given in **figure 4.15**. In case of a step scan, the set temperature is given at room temperature (25 °C) then the "wait" field allows a pause time if needed. The ramping time is zero because the set temperature equals the current temperature in this example. When heating is required, the appropriate ramping time in seconds should be entered based on the desired rate. A tolerance in temperature is defined so the shutter won't open until the temperature reaches the set temperature within the given tolerance range. The tolerance usually is small (1-5 degrees). At the end of the step scan experiment, an exposure time is given. The IP advance is the preferred displacement in mm of the IP after diffraction collection finishes. It is worth noting that the IP advance implicitly defines the gap width. In other words according to the example, 3 mm is divided into 1 mm as a slot width, where the pattern is recorded, and 2 mm will be the separation between the collected pattern and the next experiment.

A continuous scan requires three parameters, the set temperature, ramping time and the plate advance. The acquisition time in this case has no meaning as the shutter will continuously be opened during the experiment. The three parameters are used to calculate the heating rate, IP velocity, exposure time per point, and the temperature range per pixel. Increasing time is preferred for better statistics but it also increases the temperature range per pixel and the user has to optimize the conditions to find the lowest time that provides sufficient statistics coupled with lowest temperature range per pixel. In the given example (**figure 4.20**), the temperature will be raised

from RT up to 250 °C with 5 °C /min rate (i.e. 2700 seconds) with IP advance equals 22.5 mm. So the IP velocity is 0.008 mm/sec (minimum velocity limit) therefore one point on the IP will be exposed to XRD for time of 1mm travel (exit gap width) means 120 sec. Consequently, the temperature range per pixel is the exposure time multiplied by the heating rate (i.e. 10 °C in this example, 2 min multiplied by 5 °C /min).

Figure 4.15 *User parameter front panel interface of the Oven control program*

4.6 Heating rate characterization

Preliminary heating tests at different fixed voltage and currents of the power supply were studied to characterize the dependence of oven temperature on the power supply's voltage and current. These tests were also valuable to predict the appropriate range of possible heating rates. When the voltage and current is set at 30 V and 1.98 A, the temperature rise obeys a third order polynomial (**equation 4.3 and figure 4.16**) in the test range from room temperature up to 673 K. The time required for the mentioned set up was approximately 445 seconds. The average calculated heating rate was around 50 °C/min.

$$t = -548.986 + 3.61868\,T - 0.00792\,T^2 + 7.013\times10^{-6}\,T^3 \qquad (\mathbf{4.3})$$

; t is the time in seconds and T is the temperature in Kelvin

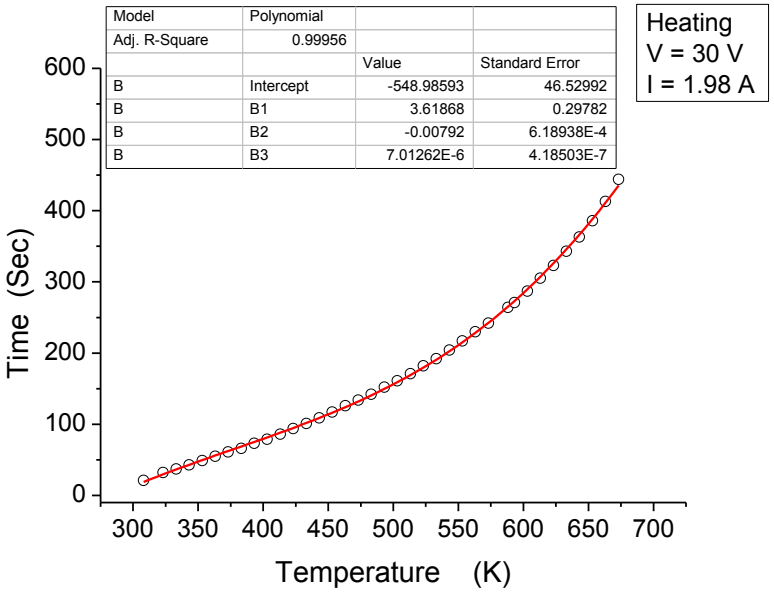

Figure 4.16 *Oven heating rate at 30 volt and 1.98 Ampere*

The situation altered when the voltage and current were raised up to 40 V and 2.66 A respectively. The temperature showed a linear increasing over time (**equation 4.4**) and the heating rate was doubled to be approximately 100 °C/min compared to the previous conditions at 30 V and 1.98 A. Although fast heating rates could be desired in some cases, it causes thermal shock and consequently thermal stress to the heating element (**figure 4.19**), which decreases its life time (i.e. the Kathnel wire). The thermal stress can break the Kathnel wire leading to an open circuit. Although the zigzag wrapping oven is preferred, due to its zero internal magnetic field, it also has a lot of plastically deformed and stressed sharp turns. Another disadvantage of high heating rates (above 50 °C/min) is the long time required to stabilize the temperature, when the set point is reached. This is a serious drawback that makes high rates unsuitable for most cases.

$$t = -192.93 + 0.5361\,T \qquad (\mathbf{4.4})$$

; t is the time in seconds and T is the absolute temperature

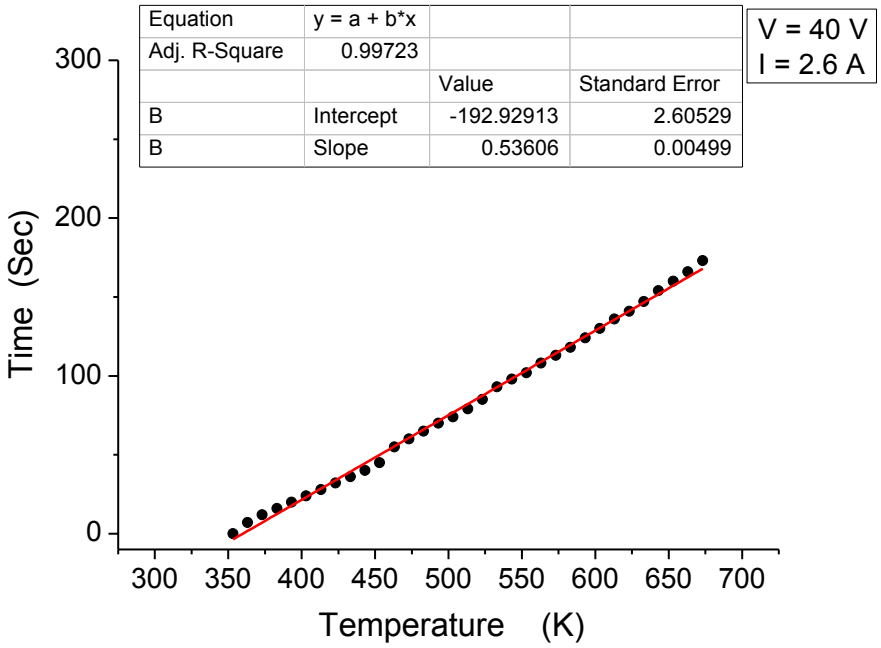

Figure 4.17 *Oven heating rate at 40 volt and 2.6 Ampere*

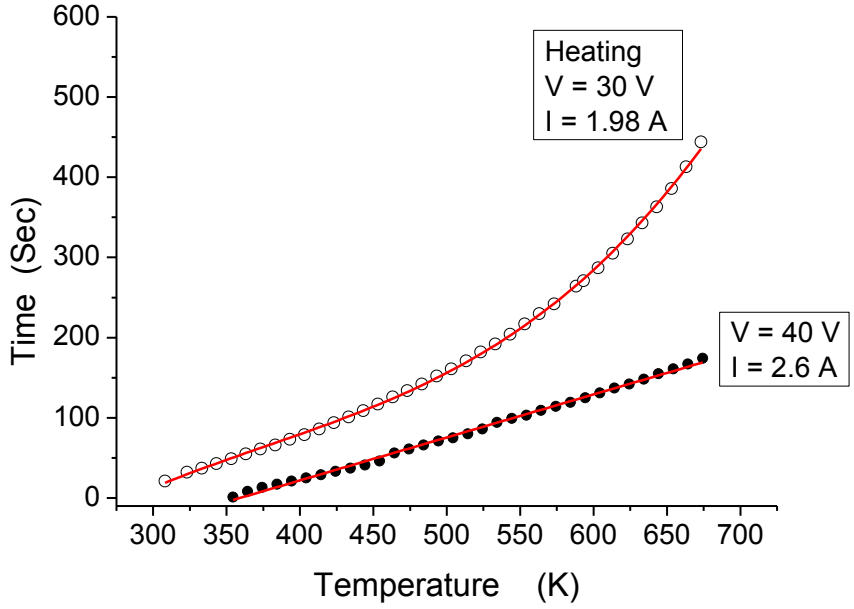

Figure 4.18 *Comparison between different heating rates under different powers*

Figure 4.19 *Thermally stressed zigzag wrapping oven*

4.7 Cooling rate

The cooling rate of the oven shows very fast cooling from 1000°C down to 400°C in a couple of minutes. Subsequently, the rate slows down with an exponential trend (**figure 4.20**). The average time required to cool the temperature down from 400°C to room temperature is around one hour according to the best exponential fit (**equation 4.5**).

$$t\ (sec) = 79.55 + 215964.6 \exp(-T\ (K)/71.5) \qquad (4.5)$$

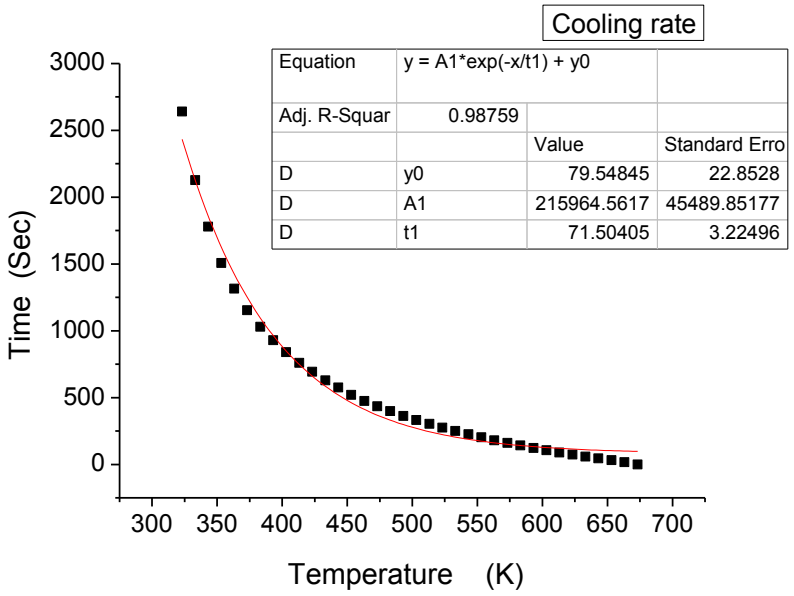

Figure 4.20 *Oven cooling rate from 400 °C to room temperature*

4.8 Pixels-2θ conversion and temperature calibration

The temperature of the oven is controlled by a Proportional-Integration-Derivative PID (PID, Omega iSeries) through an automatic current control using a manually fixed voltage to reach the desired set temperature. The temperature calibration was done with the well-known thermal expansion behavior for Silicon **(Watanabe, Yamada, & Okaji, 2004)** using **equation 4.6**. In this

case, the temperature can be obtained from the lattice parameter-temperature dependence but it requires a very precise pixel-2θ conversion because any little error in the conversion procedure will lead to a strong mathematical error in temperature calculation.

$$\alpha(\mathbf{T})\ /(10^{-6}\ K^{-1}) = -3.0451 + 0.035705\ \mathbf{T} - 7.984 \times 10^{-5}\ \mathbf{T}^2 + 9.5783 \times 10^{-8}\ \mathbf{T}^3 - 5.8919 \times 10^{-11}\ \mathbf{T}^4 + 1.4614 \times 10^{-14}\ \mathbf{T}^5 \quad \textbf{(4.6)}$$

;α is the thermal expansion coefficient and T is the temperature in Kelvin

The relation between pixels and 2θ in theory should satisfy a straight line according **equation 4.7.** The well-known peak positions for silicon ($\mathbf{2\theta_{hkl}}$) at the utilized wavelength and its corresponding pixel location on the imaging plate ($\mathbf{P_{hkl}}$) can be used to determine the unknown parameters. For example, **figure 4.21** shows the fit of **equation 4.7** at 15 keV beam energy. The R square factor equals 1, but zooming in on the fitted line shows a small mismatch between the points and the line. Possible causes are the error in the wavelength and sample displacements, especially the horizontal one that is more significant for Debye Sherrer geometry **(Scarlett, Rowles, & Wallwork, 2001)**. Possibly, the wavelength could be refined by a modified **equation 4.7** (**see equation 4.8**). Regardless of the physical aspects, some mechanical problems coming from the heavy IP holder and its gears also cause a little contribution to the peak shifts like a small tilt of the imaging plate. Each of the mentioned parameters influences the peak positions in pixels. A significant effect is visible at larger angles 2θ due to the short sample-IP distance (104 mm).

$$\mathbf{2\theta_{hkl}\ (degrees) = \ 2\theta_o + m \times P_{hkl}} \quad \textbf{(4.7)}$$

;$2\theta_{hkl}$ is the calculated 2θ position corresponding to Si planes (hkl) based on Bragg law, $2\theta_o$ is the zero shifts in 2θ, m is a geometrical factor depends on the oven geometry (IP- sample separation and IP curvature) and P_{hkl} is the (hkl) peak position in pixels.

$$\mathbf{P_{hkl}} = \frac{\mathbf{2\theta_\circ}}{\boldsymbol{m}} - \mathbf{2}\ \boldsymbol{Sin^{-1}}\left(\frac{\lambda\sqrt{\boldsymbol{h^2 + k^2 + l^2}}}{\boldsymbol{2a}}\right) \quad \textbf{(4.8)}$$

; λ is the wavelength and a the unit cell parameter of Si standard (5.4311946 ± 0.00000092 A).

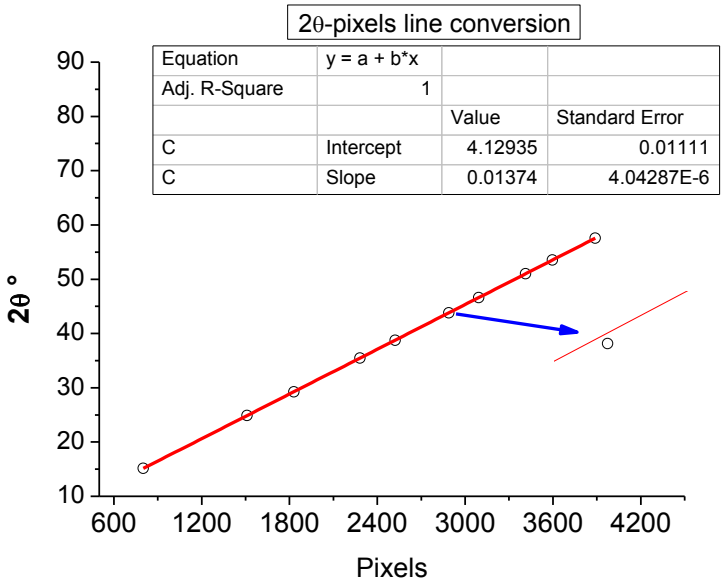

Figure 4.21 *Pixel-2θ conversion using equation 5.7*

A direct influence of non-precise pixels-2θ conversion can be observed from the peak positions' shift and consequently intensity difference between the observed and calculated model (**figure 4.22**).

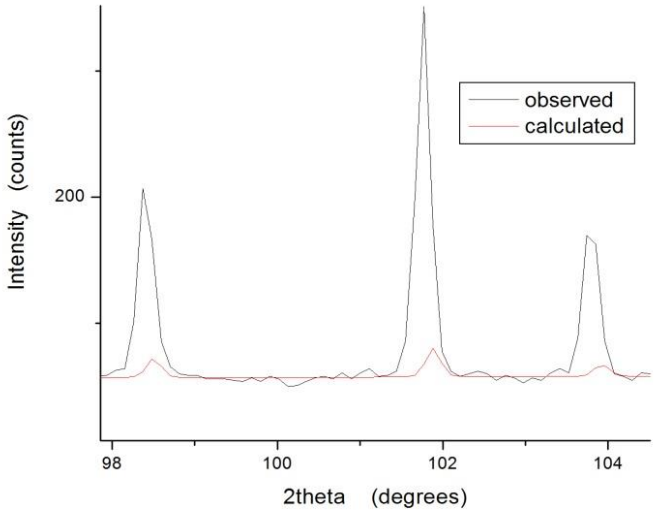

Figure 4.22 *Peaks shifts and strong intensity mismatching due to incorrect converted 2θ*

This problem might be solved mathematically by linearly interpolating the 2θ-pixels points shown in **figure 4.21.** The maximum number of the interpolation points has to be chosen in such way to satisfy the full pixels range with the same pixel step size (i.e. increment of one integer pixel each point). In this case and from the interpolated data, each pixel point can be substituted by its

corresponding interpolated 2θ value. This procedure gives high degree of accuracy and the corresponding fit improves in such case as shown in **figure 4.23**.

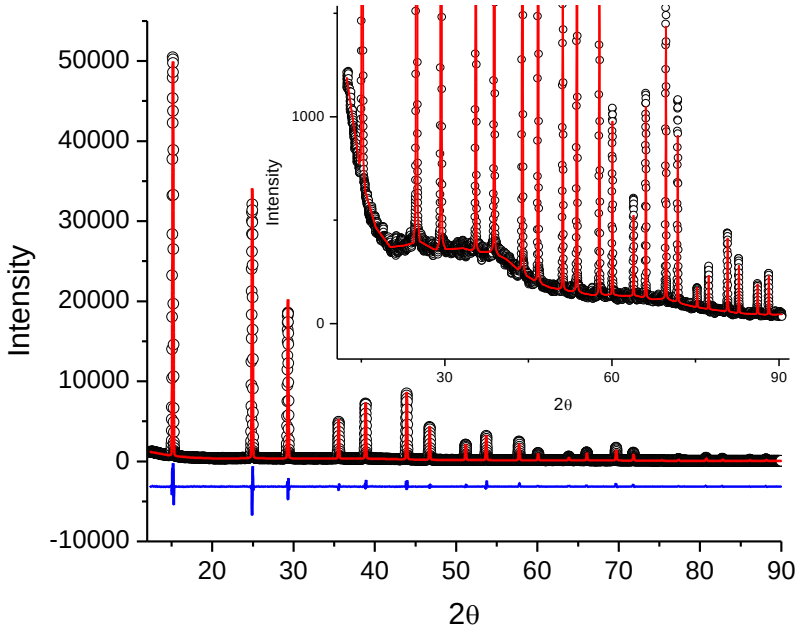

Figure 4.23 *Fitting quality of Si pattern after Pixel-2θ interpolation conversion method*

Based on the interpolation conversion method, it is possible then to correct any systematic error comes from the IP tilt by following the beam stopper reference as a function of IP advance (**figure 4.24a**) and this error is simply corrected as zero shifts in 2θ increases with IP distance (**figure 4.24b**).

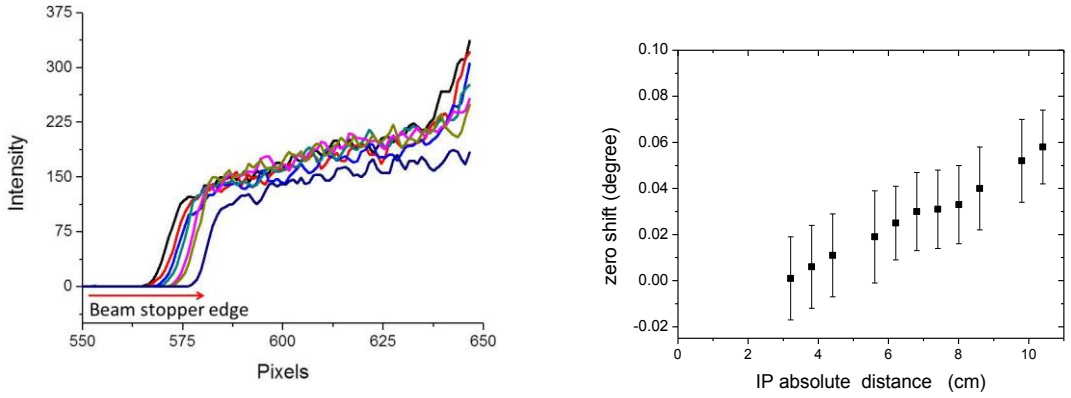

(a) (b)

Figure 4.24 *a) Beam stopper edge reference with IP advance and b) corresponding pattern zero shift*

By taking into account all previous conversions, temperature calibration was analyzed from Si standard thermal properties. A very good matching between the PID set temperature and the real temperature of the sample (**figures 4.25 and 4.26**) resulted.

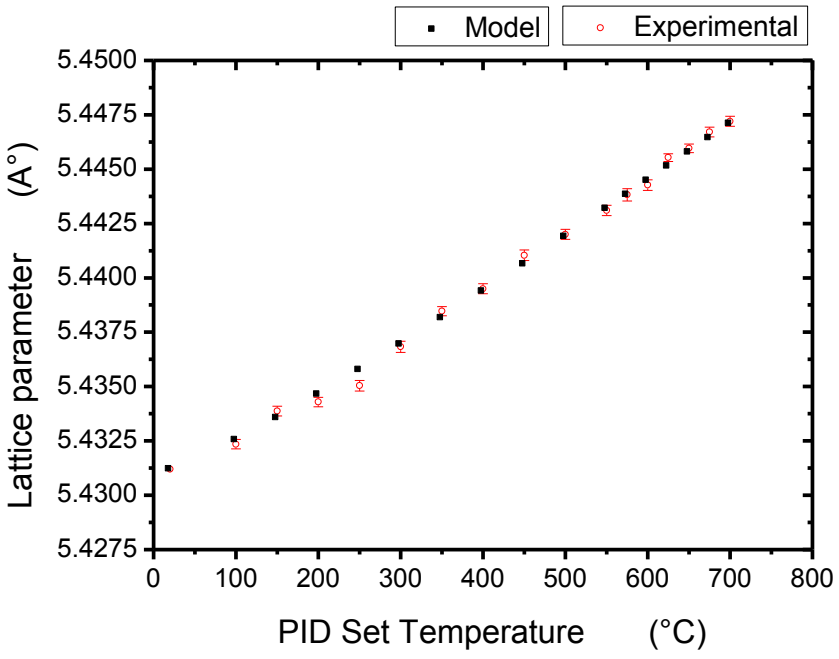

Figure 4.25 *Lattice parameter-temperature dependence of Si standard*

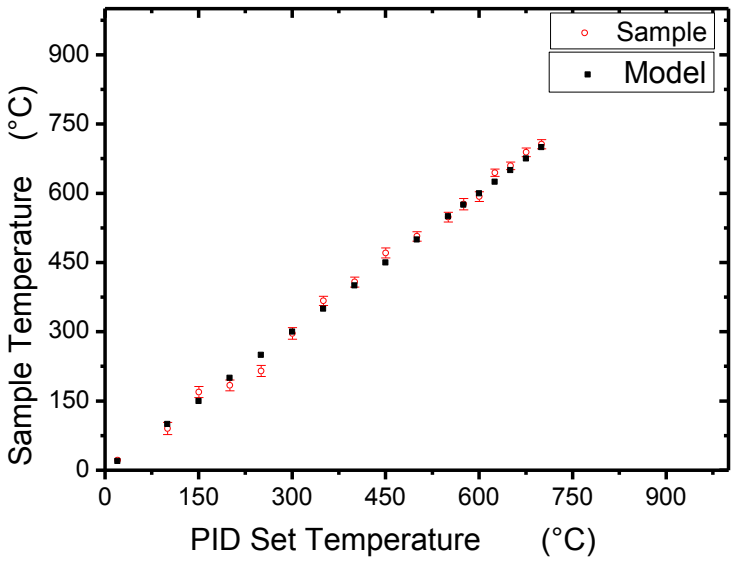

Figure 4.26 *Real sample temperature Vs. PID set temperature resulted from lattice parameter-temperature dependence analysis of Si standard*

Figure 4.27 shows a diffraction pattern of silicon collected at 15 keV (0.827 A) on an IP. The inset shows the 111 reflection demonstrating the good profile shape produced by the furnace. The instrumental contribution in terms of the FWHM is shown schematically in **figure 4.28** and it lies around 0.16 degree.

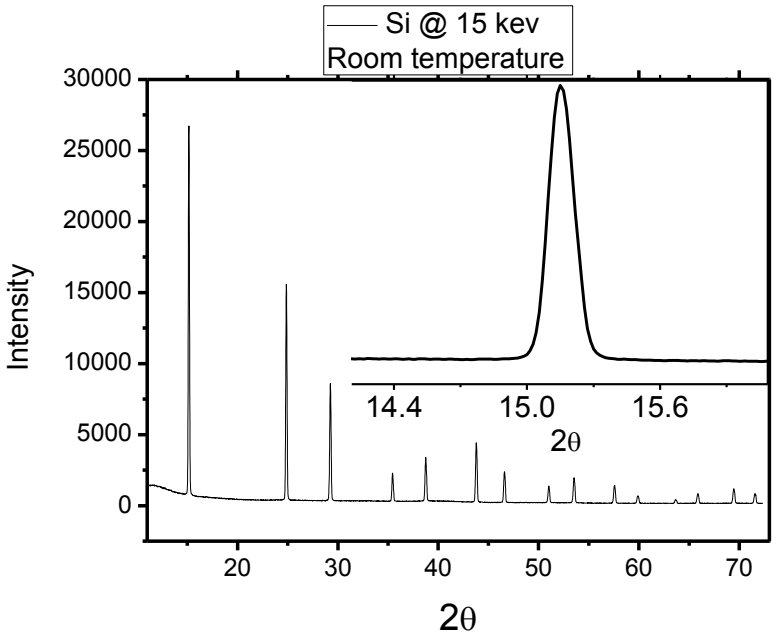

Figure 4.27 *Silicon diffraction pattern collected on an IP at 15 keV*

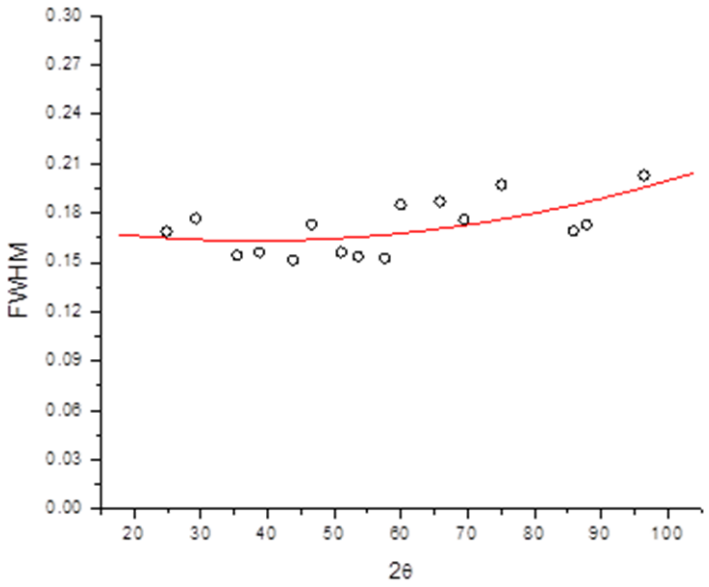

Figure 4.28 *Oven instrumental full widths at half maximum-2θ dependence*

4.9 Selected example of in-Situ XRD:

This section aims to show a real in-situ XRD example for a famous material used for hydrogen storage applications (e.g. Magnesium Hydride MgH_2). Mg is one of the famous candidates used to store hydrogen because it satisfies many advantages of storage needs while it has other limitations still in the research hand thus it is a material of more interest. The subject of MgH_2 storage properties will be studied in much detail in **chapter 6** and **7**. MgH_2 pristine powder was used to fill 0.5 mm capillary with broken top which is then sealed genteelly in a 1.5 mm capillary (outer capillary) as discussed in **section 4.3**. Then the furnace was used to perform a continuous scan 5 °C/min heating rate and the data was collected on an IP. The resulted in-situ XRD pattern is shown in **figure 4.29** together with the room temperature diffraction pattern. At room temperature, four phases are presented in the pristine powder while the β-MgH_2 covers approximately 90. The other phases are MgO, Mg and $Mg(OH)_2$ and they are formed due to the high sensitivity of Mg to the environment (e.g. Oxygen and moisture). By heating up at to temperature around 300 °C, $Mg(OH)_2$ peak disappeared by means the hydroxide layer is totally destructed then at temperature around 430 °C the hydride phase transforms to Mg as a result of hydrogen release. This example

shows how is possible to follow the progress in the crystal structure coincide in time which is the main subject of the furnace and successfully approved in this example.

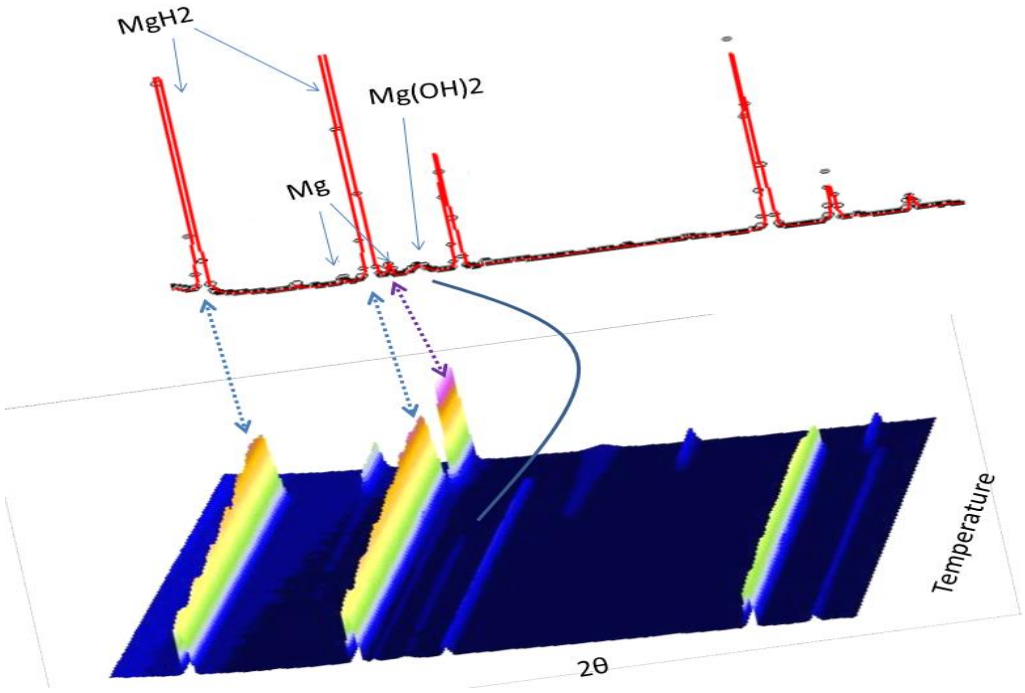

Figure 4.29 *in-Situ XRD pattern of pure MgH_2 showing a phase transformation from tetragonal MgH2 into Hexagonal Mg*

4.10 Conclusions

A furnace at MCX beamline for real time in-situ XRD experiments was well established and characterized. XRD for powder in a capillary and for thin films under controlled non-ambient environment of temperature (up to 1000 °C) and gas flow are available coupled with a simple user program interface providing step and/or continuous scan. A special double capillary system has been developed to allow gas flow through the sample. The temperature accuracy was investigated by silicon standard thermal expansion coefficient properties and the results shows a very good matching between the model and the PID reading. The oven has a little instrumental contribution on the diffraction profiles over a wide range of 2θ.

CHAPTER V

In-Situ XRD Study of Lattice Defects Influence on Grain Growth Kinetics of Nanocrystalline Fluorite

M. Abdellatief, A. Lausi, J.R. Plaisier & P. Scardi

Part of this chapter was submitted to:

Metallurgical and Materials Transactions A, (2013), In press

DOI: 10.1007/s11661-013-1786-8

Abstract

The growth process of nanocrystalline fluorite was studied by in-situ synchrotron radiation X-ray diffraction. The two studied samples had comparable crystalline domain size, but quite different content of lattice defects as a result of the different preparation procedures: ball milling of coarse CaF_2 powder or co-precipitation of $CaCl_2$ and NH_4F. It is shown that the high dislocation density in the ball milled fluorite is responsible for a recrystallization process above 500°C, which is not observed in the chemically synthesized fluorite. The linear Thermal Expansion Coefficient of both nanocrystalline powders, as obtained also from the in-situ X-ray diffraction data, shows a smaller increase with temperature than suggested by the literature on coarse-grained fluorite.

5.1 Introduction

Many applications of nanocrystalline materials are based on specific domain size/shape and content/distribution of lattice defects defects **(Sakintuna, Darkrim, & Hirscher, 2007) (Kandhasamy, Nallathamby, & Minakshi, 2012) (Fukunaga, Itoh, Orimo, & Fujii, 2002) (Sumino, 2000) (Majumdar, Huhtinen, Majumdar, & Paturi, 2012) (Fukabori, et al., 2012) (Schichtel, et al., 2010)**. The latter – most notably, the nanocrystal surface – play a key role in diffusion processes in metallic **(Peterson, 1986)** and in ceramic **(Heitjans & Indris, 2003)** materials. A marked improvement of ionic diffusivity is observed in materials with high lattice strain (e.g. caused by extensive plastic deformation), as compared with conventional bulk phases **(Puin, Rodewald, Ramlau, Heitjans, & Maier, 2000) (Heitjans & Indris, 2003) (Janek, Martin, & Becker, 2009)**. Besides lattice defects, also a small domain size enhances grain boundary ionic diffusivity **(Martin, 2003) (Durá, et al., 2010)** as an effect of the large surface to volume ratio.

Applications based on diffusion frequently require high temperatures, so it is necessary to assess the stability of nanocrystalline systems above room temperature. In-situ X-ray diffraction (XRD) is especially useful to study grain growth mechanisms and kinetics, and in a more general sense to understand the evolution of the diffusion process in nanocrystalline materials.

Several grain growth mechanisms in the solid state have been reported in literature **(Khawam & Flanagan, 2006)**; however, Ostwald Ripening (OR) **(Zhang, Huang, & Lin, 2010) (Wagner, 1961) (Kirchner, 1971)**, and Oriented Attachment (OA) **(Zhang, Huang, & Lin, 2010) (Moldovan, Wolf, & Phillpot, 2002) (Moldovan, Yamakov, Wolf, & Phillpot, 2002)**, have been found to be more appropriate to describe growth processes in nanostructured materials. According to the OR mechanism, large grains grow at the expenses of smaller ones, in many cases obeying the Lifshitz-Slyozov equation of linear (particle volume) growth as a function of time **(Zhang, Huang, & Lin, 2010)**. Although the OR mechanism is quite a classical, several examples were found to deviate from the expected growth trend **(Peng, Wickham, & Alivisatos, 1998) (Krill III, et al., 2001) (Zhang & Banfield, 1999)**. Moreover the growth in presence of a high density of lattice defects is also not completely accounted for by the OR model. Recently, the OA approach **(Zhang, Huang, & Lin, 2010) (Moldovan, Wolf, & Phillpot, 2002) (Moldovan, Yamakov, Wolf, & Phillpot, 2002)**, was found to take the evolution of structure morphology into account during the early stages of the growth process at the nano scale. Several experimental studies show that grain rotation plays a significant role **(Ribeiro, Lee, Giraldi, Aguiar, Longo, & Leite, 2005) (Shen & Lee, 2001)**, as small grains rotate until they adjust to a common crystallographic axis between each two neighbors in order to decrease the (surface) grain boundary free energy. Lattice plastic deformation and dislocations were reported to enhance the grain orientation mechanism, both in

theoretical **(Bobylev, Mukherjee, & Ovid'ko, 2009)** **(Mukherjee, 2002)**, and in experimental studies **(Ribeiro, Lee, Giraldi, Aguiar, Longo, & Leite, 2005)**. Some experimental studies rely on High Resolution Transmission Electron Microscopy (HRTEM) to capture the growth mechanism in-situ, but this is not always possible and direct evidence is limited to relatively few cases. As an alternative, XRD line profile analysis (LPA) **(Klug & Alexander, 1974)** **(Snyder, Fiala, & Bunge, 1999)** **(Scardi P. , in Powder Diffraction: Theory and Practice)**, can follow the evolution of crystallite size and lattice strain with temperature. If a state of the art LPA approach is used, like Whole Powder Pattern Modeling WPPM **(Scardi & Leoni, 2002)** **(Scardi & Leoni, Whole Powder Pattern Modeling: theory and applications, 2004)**, it is possible to directly model structural broadening sources, like dislocations and finite crystallite size, and to follow the evolution of the nanostructure with temperature, so to disclose fine details of the grain growth process.

In this work, an in-situ XRD data collection is used to study the difference between grain growth mechanisms in heavily defected and in defect-free nanocrystalline fluorite. Even if the specific results are obtained on the studied material, several conclusions, and the role of lattice defects in particular, are of much broader scope.

5.2 Experimental Details

Two samples of nanocrystalline CaF_2 were considered. The first one, CaF2@90%, was obtained by co-precipitation of $CaCl_2$ and NH4F in 90% ethanol – 10% water precipitation **(Wang, Fan, Pi, & Wang, 2005)** **(Omolfajr, Nasser, & Mahmood, 2011)**. The chemical synthesis conditions yield fine nanocrystals with no significant amount of (line/planar) defects. The second sample, CaF_2@64h, was obtained by high energy ball milling of bulk (mm grain size) commercial grade (98.5 % purity) fluorite for 64h, a treatment leading to finely divided crystalline domains, with a size similar to the CaF2@90% grains, and a high density of lattice defects, mostly dislocations **(Abdellatief, Abele, Leoni, & Scardi, 2013)**.

All data were collected at the MCX beamline of the Italian Synchrotron ELETTRA (Trieste, I) **(Lausi, Busetto, Leoni, & Scardi, 2006)**. A first set of measurements was made using a capillary (Debye-Scherrer geometry) and a hot air blower for in-situ studies from RT to 400°C. These data were used mainly to follow the unit cell parameter-temperature dependence and the linear thermal expansion coefficient. To limit the measurement time in isothermal conditions at different temperatures, powder diffraction data were collected across the angular range of the three most

intense reflections of fluorite ((111), (220), (311)) only. Before measurements on fluorite, a capillary filled with the NIST SRM 640a Silicon standard was used for calibration.

Additional (0.2 mm diameter) capillaries were filled, respectively, with CaF_2@64h and with CaF_2@90%, for isochronal measurements with heating rates of 5, 10, and 15 °C/min. Measurement geometry was still Debye-Scherrer, but this time the capillary was placed in an oven coupled to a translating curved imaging plate (IP) detector **(Riello, Lausi, Macleod, Plaisier, & Fornasiero, 2013)**. The oven control software was used to control different experimental parameters, like heating rate, velocity of the IP (0.01 mm/sec) and total IP displacement. The first and second slits at the oven entrance were opened to 0.3 mm, whereas the IP opening strip was ~1 mm. The scanning time for all six experiments was fixed to 100 s per point, which was found the minimum time to get sufficient counting statistics. As a consequence, each point on the IP covered a finite range of temperature, changing with the heating rate (ΔT= 8.3 °C @ 5 °C/min; ΔT=16.7 °C @ 10 °C/min; ΔT= 25 °C @ 15 °C/min). After each scan the IP was read using a scanner with a pixel size of 25x25 μm, and then the Fit2D program was used to convert the images into powder patterns. A capillary filled with NIST SRM 640a Silicon standard was used to correctly transform pixels to 2θ steps.

5.3 Results and Discussion

5.3.1 In situ XRD measurements with hot air blower:

Three peaks for each scan collected at different temperatures were modeled using the PM2K software **(Leoni, Confente, & Scardi, 2006)**; based on the WPPM approach **(Scardi & Leoni, 2002)** **(Scardi & Leoni, Whole Powder Pattern Modeling: theory and applications, 2004)**, assuming a lognormal distribution of spherical domains, and dislocations laying on the primary slip system of fluorite **(Muñoz, Domingguez-Rodriguez, & Kasstaing, 1994)**. Refined (microstructural) parameters are: mean (μ) and variance (σ) of the diameter distribution, mean dislocation density (ρ), effective outer cut-off radius (Re) and fraction of edge/screw dislocation types. As shown below, some parameters can be restrained to limit instability in the least square modeling; however, even if statistics is affected by the short counting time (1s per 0.05° step, to reduce data collection time and minimize temperature errors), the goodness of fit was relatively fine in all cases (**e.g., see Fig. 5.1**). The room temperature results of PM2K **(Leoni, Confente, & Scardi, 2006)**, (**Table 5.1**) show that the two samples have almost the same unit cell parameter and crystallite size, although they are differently prepared. The main difference, as shown below in

greater detail, is in the defect content: while CaF_2@90% is free of dislocations (within the limits of sensitivity of LPA), the CaF_2@64h sample shows a high density of dislocations.

The linear thermal expansion coefficient (TEC) was obtained in the usual way, from the variation of the unit cell parameter. According to literature, the thermal expansion coefficient α of CaF_2 should obey a linear relation. Data in **Fig. 5.2** were analyzed by linear regression according to **equation (5.1)**

$$\alpha(T) = \alpha_0 + \alpha_1 T \qquad (5.1)$$

where α_0 and α_1 are parameters to be adjusted by linear regression, and T is the temperature in Kelvin. **Table 5.2** reports the best linear fit coefficients in comparison with literature data for bulk CaF_2 **(Aurora, Day, & Pederson, 1994)**. According to the results, the TEC for the nanocrystals in the limit of low temperatures (α_0), especially those with high dislocation density, is higher than the bulk, but the latter seems higher at room temperature and above. So far this evidence did not find any convincing explanation, even if it is recognized (see below) that the evolution of the nanostructure – dislocation annealing and crystalline domain growth – mostly likely affects this result.

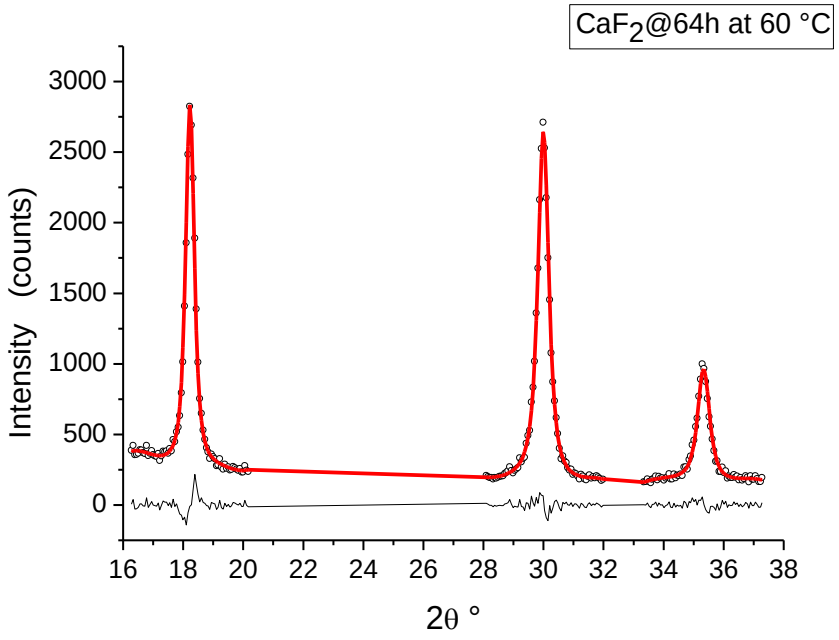

Figure 5.1 *PM2K modeling result for sample CaF2@64h at 60 °C*

Table 5.1 *Results of the PM2K modeling for RT data*

	Unit cell parameter (nm)	<D> (nm)	Dislocation density (10^{15} m^{-2})
CaF_2@90%	0.54673(2)	10.8(1)	-
CaF_2@64h	0.54655(3)	12.3(24)	31(2)

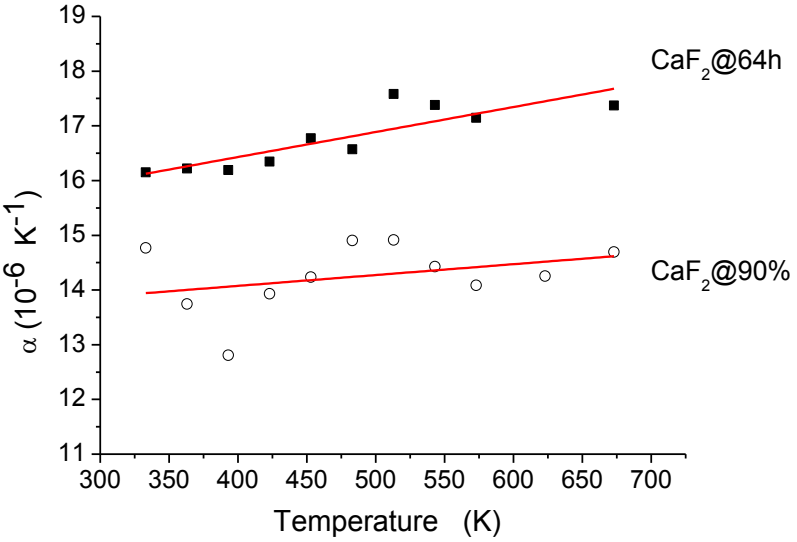

Figure 5.2 *Thermal variations of the linear thermal expansion coefficients of CaF_2@90% (open circle) and CaF2@64h (solid square).*

Table 5.2 *Linear thermal expansion coefficients: coefficients of temperature variation and Room Temperature (RT) values. Bottom raw, literature data for bulk fluorite* **(Aurora, Day, & Pederson, 1994)**.

	α_0 (10^{-6} K^{-1})	α_1	α_{RT} (10^{-6} K^{-1})
CaF_2@90%	13.3(9)	0.0020(2)	14(1)
CaF_2@64h	14.6(5)	0.0046(9)	16(4)
CaF_2	13.23	0.0172	18.4

Lattice anharmonicity is expected to cause a linear change of TEC with temperature, even if lattice defects can give additional terms **(Schuler, Aurora, Pederson, & Day, 1995)**. For example, an excess thermal expansion, $\Delta\alpha$, is observed at high temperature, when the fraction of intrinsic (thermal) vacancies becomes important. This can explain why the TEC is larger in CaF_2@64h than in CaF_2@90%, as the former has a much higher concentration of extrinsic lattice defects caused by plastic deformation.

Explaining why the TEC of both samples grows with temperature much less than bulk fluorite is less straightforward. Literature on Se **(Zhao & Lu, 1997)** Cu **(Birringer, 1988)** and Pd **(Tong, Wang, Ding, Jiang, & Lu, 1992)** shows that the TEC for nanocrystals is higher than in the corresponding coarse-grained materials. However, other studies report a decrease in TEC, e.g. in some ball milled metals **(Zhao, Sheng, & Lu, 2001)** **(Eckert, Holzer, Krill III, & Johnson, 1992)**; as a top-down synthesis route, and for chemically synthesized silver **(Hu, Cai, Cuncheng, Gan, & Chen, 2005),** as a bottom-up route. The decrease in TEC of ball milled nanocrystalline metals was explained in terms of grain boundary relaxation, as the milling reaches a steady-state grain size. The grain size relaxation mechanism suppresses the stored grain boundary enthalpy and thereby the TEC **(Zhao, Sheng, & Lu, 2001)**. The domain size in CaF_2@64h is ~12 nm, about the same value obtained after a much shorter milling of 16 hours; **(Abdellatief, Abele, Leoni, & Scardi, 2013)** while the size reaches a steady state in a relatively short time, further milling only increases the dislocation density, until this parameter also reaches a saturation stage, as an effect of balancing between damage and annealing processes. Therefore, the grain boundary relaxation process might play an important role in decreasing the TEC of CaF_2@64h sample.

For nanocrystalline Ag produced by sol gel method, which is a bottom-up route like the method used to produce the CaF_2@90% sample, the TEC's decreasing was attributed to the large grain surface energy **(Hu, Cai, Cuncheng, Gan, & Chen, 2005)**. While this might appear in conflict with the grain boundary relaxation process invoked for the ball milled fluorite, an important difference is that crystalline domains in ball milled samples develop a real grain boundary, as all grains are fragmented but strongly agglomerated, whereas a chemical synthesis like the co-precipitation used for CaF_2@90% delivers loose (or weakly interacting) crystalline grains. The latter thus has a large free surface area with no real grain boundaries, whereas the opposite is true of the ball milled fluorite.

The line profiles collected with the capillary geometry and hot air blower can also provide a preliminary assessment of the microstructure stability in the RT – 400°C range. As shown in **figures 5.3** the domain size is relatively stable, with just a shallow growth in the investigated range. Samples CaF_2@90% and CaF_2@64h have comparable domain sizes around 12 nm. The latter two samples, however, show a quite different lattice defect content: while CaF_2@90% has none (within the detection limit of line profile analysis), CaF_2@64h has a high density of dislocations, initially unaffected by the heat treatment. More details on the evolution of the microstructure in temperature are provided by the isochronal measurements made with the oven / Imaging Plate system.

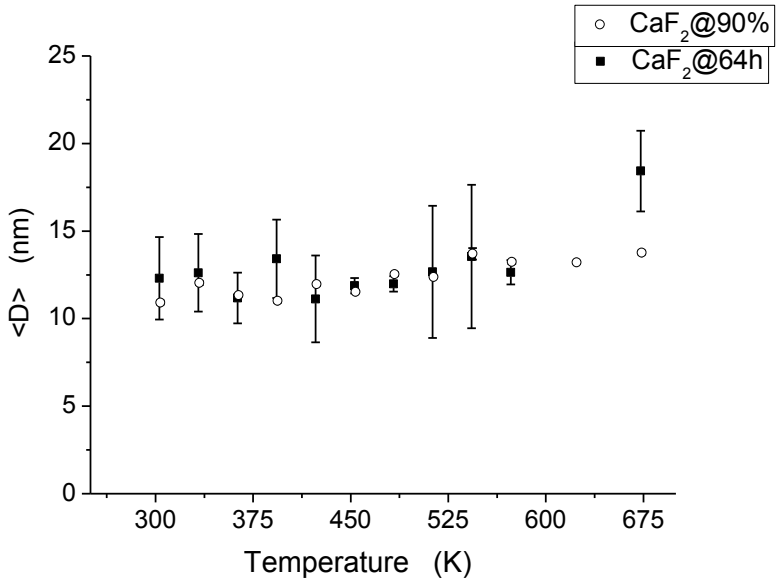

Figure 5.3 *Crystallite size evolution with temperature as obtained from hot air blower measurements*

5.3.2 In-Situ XRD measurements in oven with translating curved IP detector:

Non-isothermal heating analyses were done for samples CaF_2@64h and CaF_2@90%, in order to compare the growth kinetics for heavily defected and nearly defect free crystalline domains. The oven with the IP was useful in this case, as it allows many data collections of quite many data, across an extended angular range within a relatively short measurement time. As a main drawback of this experimental set-up, the IP has a low angular resolution, which might affect the stability of the PM2K-WPPM algorithm. The main parameters that were found unstable were the variance of the lognormal size distribution and the effective outer cut of radius of the dislocation model for sample CaF_2@64h.

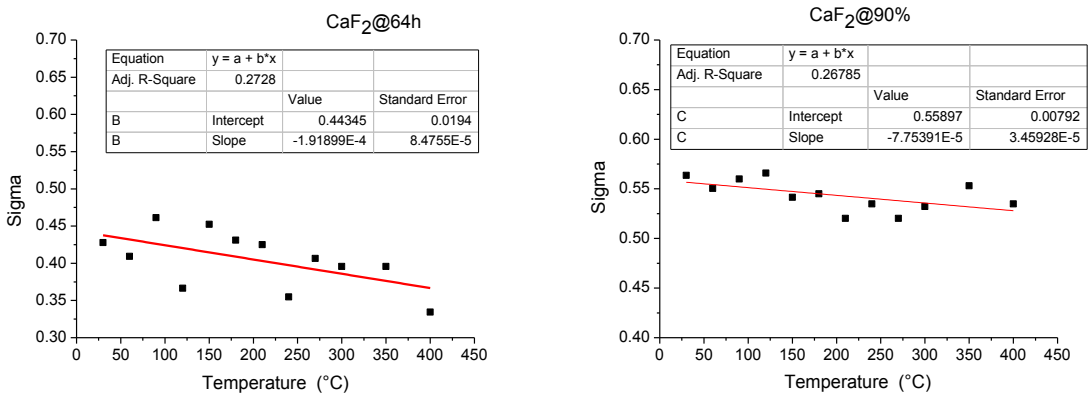

Figure 5.4 *Temperature dependence of lognormal variance for CaF_2@64h and CaF_2@90% (in-situ high temperature with hot air blower)*

As shown in **figure 5.4** for the in situ high temperature data collection with hot air blower, the lognormal variance of both samples has just a weak dependence on the temperature; the parametric expression obtained from linear regression can then be used to reduce instability in the analysis of data collected with the IP. In particular, values of domain size from IP data were calculated using the refined expressions in **figure 5.4**, so to limit refinable domain size parameters to the lognormal mean only. In case of sample CaF_2@64h the effective outer cut-off radius (Re) was fixed to the room temperature value obtained from the data collected with the hot air blower. As a consequence of these constraints, more than the exact (actual) value of dislocation density, the results shown in the following are useful to study the trend with the temperature.

As an example of measured data with this configuration, **Fig. 5.5** shows in-situ powder patterns of CaF_2@64h, collected by the IP with a heating ramp of 5 °C/min.

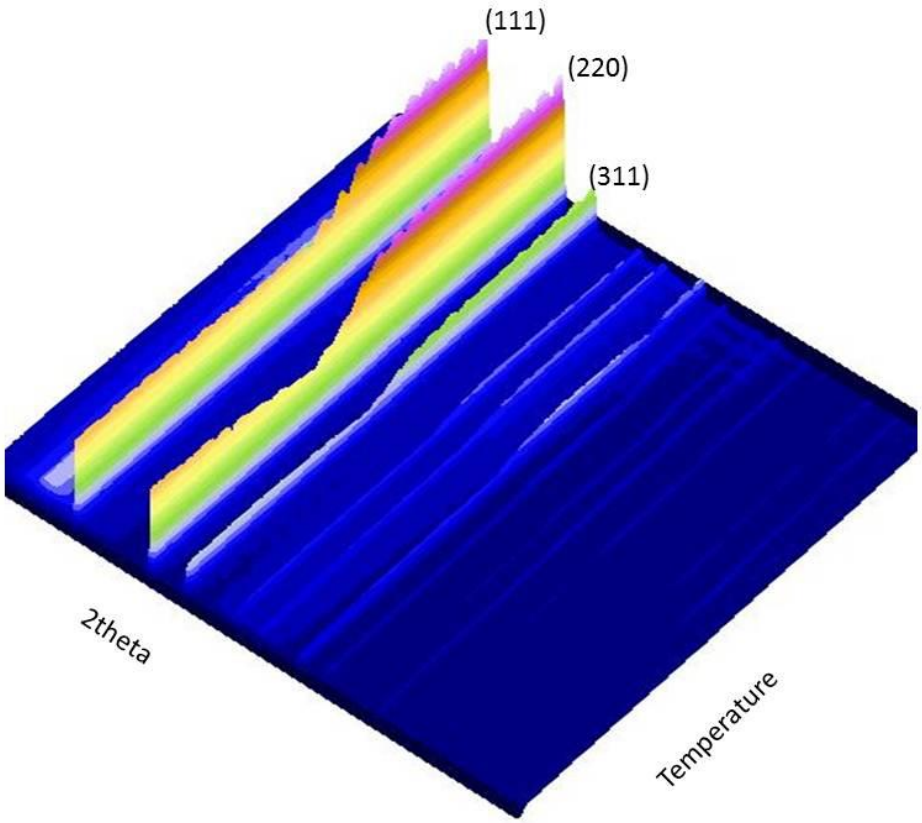

Figure 5.5 *Powder patterns collected in situ, using the oven with IP for sample CaF2@64h (heating rate, 5 °C/min): the three most intense observed reflections are labeled by the corresponding Miller indices.*

The crystal growth process can schematically be divided in two stages. At low temperature (RT to ~500°C) domain size is little affected, and trends for CaF_2@64h and CaF_2@90% are similar (**Fig. 5.6**): crystalline domains starting from roughly 12 nm size reach approximately 25 nm at 500 °C. Around that temperature a clear splitting occurs, with CaF_2@64h showing a sudden increase in grain growth rate with respect to CaF_2@90%, which keeps on growing continuously. The faster grain growth in CaF_2@64h is coupled with a marked decrease in the dislocation density, shown in **Fig. 5.7**. As already observed in ball milled metallic nanocrystalline systems **(Leoni M. , Scardi, D'incau, & Luciani, 2012)** **(Molinari, Libardi, Leoni, & Scardi, 2010)**, this picture is compatible with a recrystallization process taking place in CaF_2@64h above 500°C.

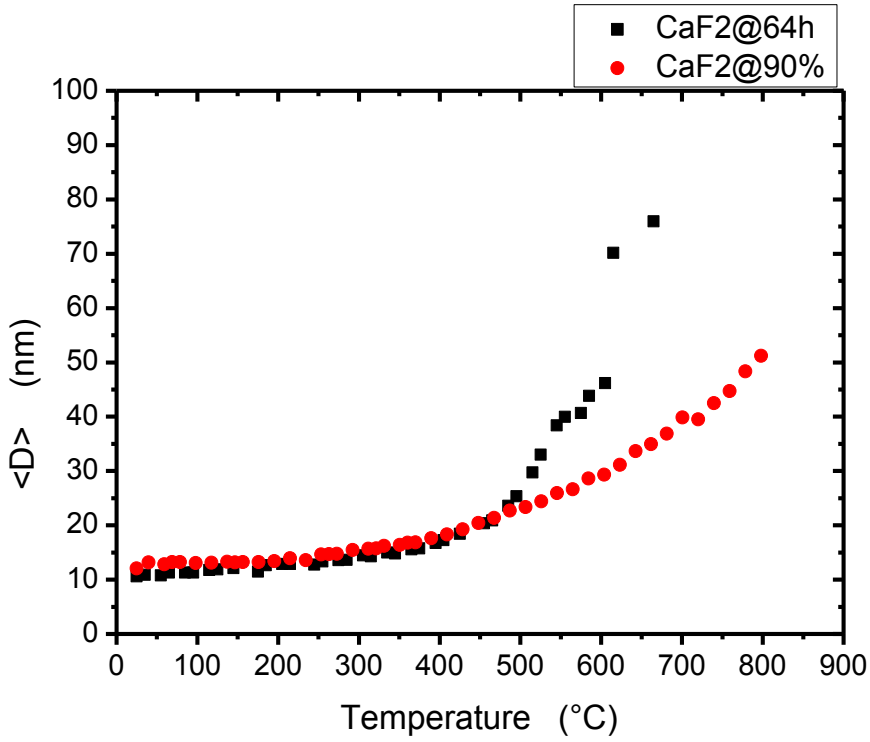

Figure 5.6 *Temperature dependence of the mean crystalline domain size (diameter) for samples CaF2@64 (solid square) and CaF2@90% (solid circle).*

In more detail, the dislocation density is nearly constant up to ~300°C (**Fig. 5.7**), which can be considered as the upper limit of the stability range for the nanostructure. Then a recovery process takes place, with ρ steadily decreasing, probably as an effect of dislocation disentanglement and annihilation processes, until the temperature is high enough to exploit the excess energy of the residual dislocations to start the recrystallization process. This point can be seen in **Fig. 5.7**, at temperatures of 500°C and higher, where the growth rate clearly increases.

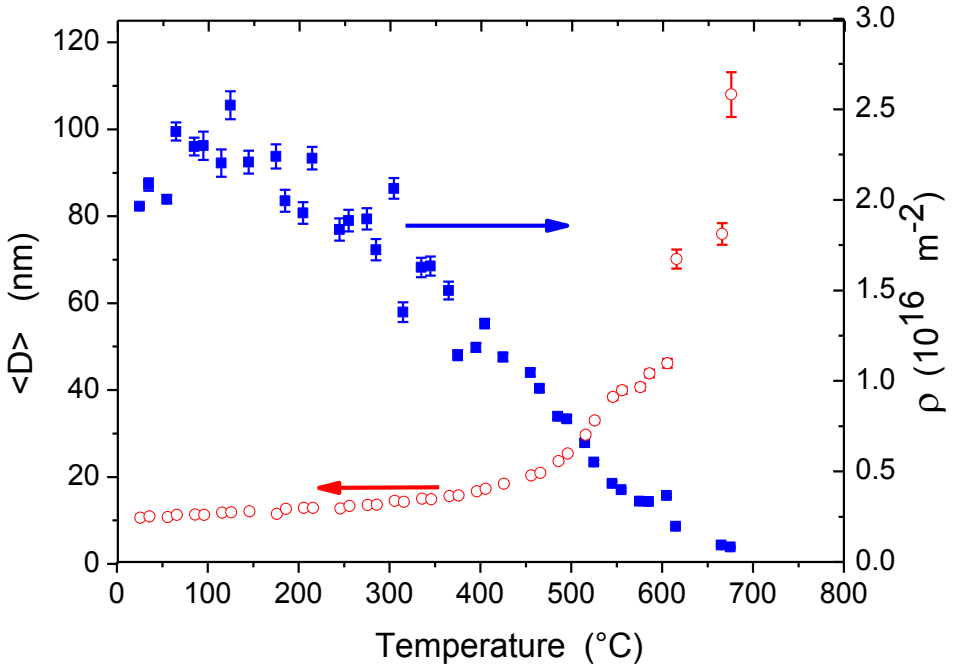

Figure 5.7 *Changes in mean crystalline domain size and dislocation density for sample CaF2@64h heat treated at 5 °C/min*

5.3.3 Grain growth Kinetics analysis of plastically defected nanocrystalline fluorite:

Further insights in the kinetics process can be gained from recent theoretical work on the deformation of nanocrystalline materials **(Bobylev, Mukherjee, & Ovid'ko, 2009)** **(Mukherjee, 2002)**, which underlines the role of dislocations in activating grain rotation mechanisms. The high density of dislocations in the ball milled sample is responsible for a considerable amount of excess energy (and volume) **(Zhao, Sheng, & Lu, 2001)** **(Scardi & Leoni, Diffraction Analysis of the Microstructure of Materials, 2004)**. Even if in our case there is no applied stress, dislocations can have some effect on the growth caused by their movement and annealing process, which might involve grain rotations such to activate the coalescence between neighboring grains with similar orientation **(Zhang & Banfield, 1999)** **(Ribeiro, Lee, Giraldi, Aguiar, Longo, & Leite, 2005)**. A closer look at **Fig. 5.6** and **5.7** shows that a first change in growth rate of the ball milled sample takes place at about 500 °C, which is 100 °C below the temperature of what was labeled as stage III, which is the final recrystallization process. Especially at slow heating rate, the dislocation density shows the fastest decrease in this region between 500 and 600°C, which matches the first growth "step" in the domain size.

The energy stored at the grain boundaries plays a key role in the recrystallization process observed in sample CaF_2@64h. The grain boundary energy of nanostructured materials, especially if highly defected as CaF_2@64h, is higher than in the corresponding bulk phases and can be released at temperatures around 500°C and higher. This energy originates from excess dislocations in the grain boundaries regions and also from the grain orientation mismatch. Therefore, to release this energy a possible mechanism might involve diffusion along the grain boundaries, supporting the rotation of the grains. This would enhance the growth process as properly aligned grains lower the grain boundary energy. A similar trend of grain growth has been reported in the literature on nanostructured defected Aluminum **(Dong, Zou, & Yang, 2001)**, where it was also found that grains grow slowly till a certain temperature (ca 300°C) and then turn to a much faster growth process. The sharp changes was also attributed to a release of the grain boundary stored energy.

The situation is different for sample CaF_2@90%, where there is no real grain boundary, as in CaF_2@64h, and apparently no further energy contributions from lattice defects. In this case the excess energy can only come from the free surface, which tends to relax (reorganize) in nanocrystals, and most presumably involves a much lower stored energy than the ball milled nanocrystals. This would involve a weaker driving force for grain movements and rearrangement than in the ball milled fluorite.

The mean dislocation density data (**figure 5.8**) can be used to assess the recrystallization temperature (T_p) and at least an estimate of the related activation energy. The chosen reference of T_p was when the dislocations reached values close to zero, within the experimental error (arrows in **figure 5.8**). **Table 5.3** contains the lower and upper limit of the calculated activation energy taking into account the temperature tolerance (unfortunately the analysis is based on three temperatures only). Kissinger equation (**equation 5.2**) was then used to estimate the activation energy (**see figure 5.9**), E:

$$\boldsymbol{ln\left(\frac{\beta}{T_p^2}\right) = A - \frac{E}{RT}} \qquad \textbf{(5.8)}$$

where β is the heating rate, R is the molar gas constant (8.3144621 J/(mol K)) and A is a constant.

The situation is different for the chemically synthesized sample, which shows no sharp change in the growth rate. Considering that the nanocrystals of CaF_2@90% are free of lattice defects – if not for the presence of the nanocrystal surface – we can assume that the steady growth stems from a progressive agglomeration (sintering). The lack of lattice defects is therefore a nanostructure stability factor, as the mean domain size at the highest temperature measured for CaF_2@90%

(800°C) is about 50 nm, i.e. four times the starting RT size. Under the same conditions (**figure 5.6**) domain size for CaF_2@64h is well above the detection limit of line profile analysis, which for the present data quality can be set to ≥200 nm.

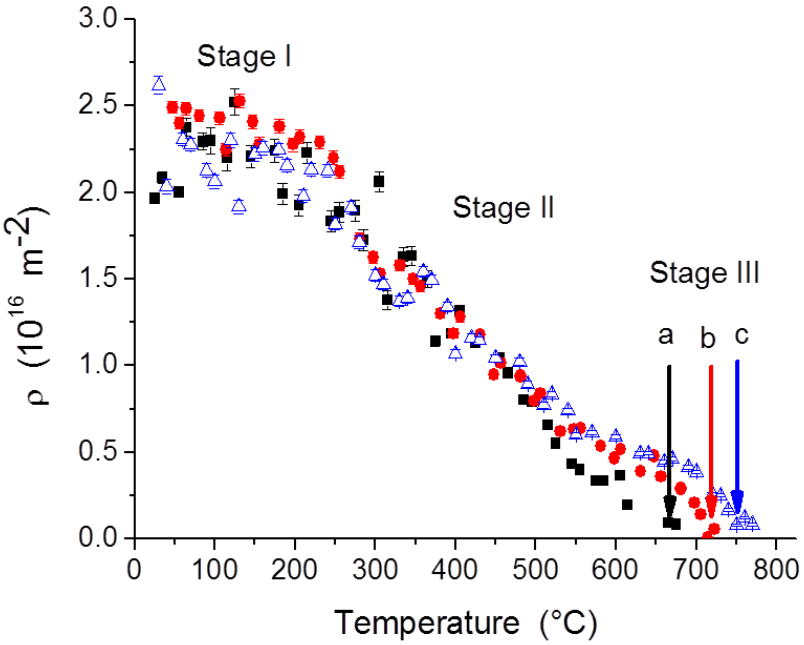

Figure 5.8: *Temperature dependence of the mean dislocation density ρ for sample CaF2@64 at three different heating rates(5 °C/min (solid squares), 10 °C/min (solid circles) and 15 °C/min (open triangles)). Arrows show the estimated recrystallization temperatures (a-660, b-720 and c-750°C, respectively for 5, 10 and 15 °C/min).*

Table 5.3 *Calculated lower and upper crystallization activation energy limits for CaF2@64h sample using Kissinger equation*

Rate (°C/min)	Crystallization temperature (°C)	Upper E (k J/mol. K)	Lower E (k J/mol. K)
5	661	98	68
10	718		
15	751		

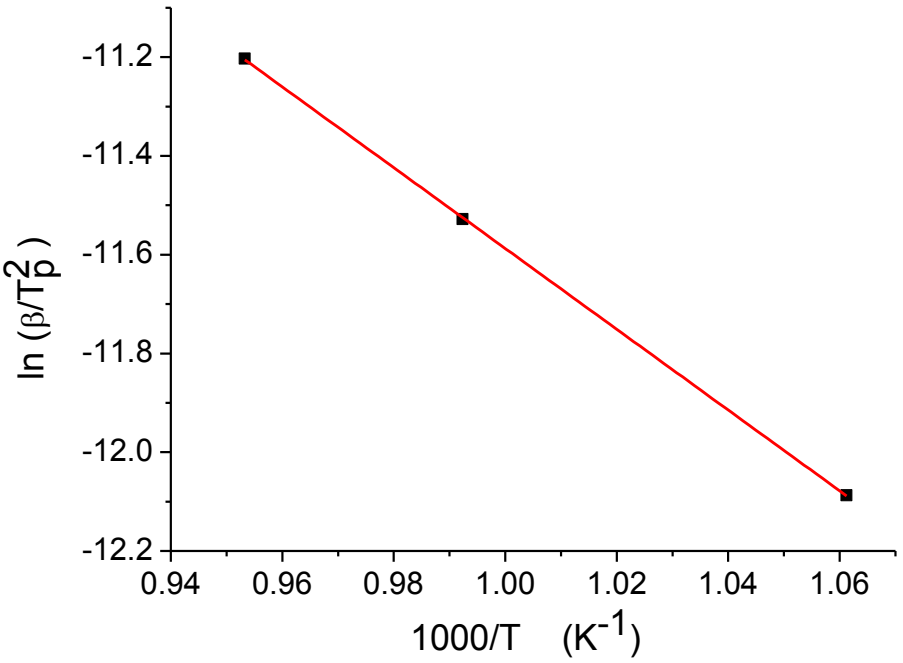

Figure 5.9 *Kissinger plot for activation energy (sample CaF_2@64h)*

5.4 Conclusions

Lattice defects in nanocrystalline materials can contribute to store a considerable amount of energy, which affects properties and thermal stability. The results of this work point out the difference between the contribution of free surfaces, as in chemically synthesized and weakly bound nanocrystals, and that of grain boundaries in heavily deformed nano-polycrystalline aggregates. In particular, it was shown that dislocations accumulated in large amount during extensive ball milling of fluorite tend to slowly anneal but, at sufficiently high temperature (>500°C) they trigger a recrystallization process with an activation energy comparable with that measured for ball milled metals.

A nanocrystalline fluorite with similar domain size but free of dislocations, produced by co-precipitation of $CaCl_2$ and NH_4F, showed a similar slow growth trend at low temperature, with no abrupt changes as those seen in the ball milled sample. It can then be concluded that the bottom up approach of chemical synthesis provides fluorite nanocrystals with better thermal stability.

The nanostructure was also responsible for different values of linear thermal expansion coefficients: as a consequence of the larger amount of free volume accumulated during mechanical deformation, the TEC of the ball milled sample is systematically larger than that of the fluorite produced by co-precipitation. In both cases, however, the TEC grows with temperature at a much lower rate than bulk fluorite. Although some possible explanations can be put forward, at least on a qualitative level, more extensive studies will be required to understand this feature.

CHAPTER VI

Effects of SnO_2 on hydrogen desorption of MgH_2

M.Abdellatief, R. Campostrini, M. Leoni, P. Scardi

Part of this chapter has been published in

International Journal of Hydrogen Energy, Vol. 38, Issue 11, PP. 4664-4669, (2013)

http://dx.doi.org/10.1016/j.ijhydene.2013.02.016

Abstract

The hydrogen desorption properties of Magnesium Hydride (MgH_2) ball milled with cassiterite (SnO_2) have been investigated by X-ray powder diffraction and thermal analysis. Milling of pure MgH_2 leads to a reduction of the desorption temperature (up to 60 K) and of the activation energy, but also to a reduction of the quantity of desorbed hydrogen, referred to the total MgH_2 present, from 7.8 down to 4.4 wt%. SnO_2 addition preserves the beneficial effects of grinding on the desorption kinetics and limits the decrease of desorbed hydrogen. Best trade-off e activation energy lowered from 175 to 148 kJ/mol and desorbed hydrogen, referred to the total MgH2 present, lowered from 7.8 to 6.8 wt% e was obtained by co-milling MgH_2 with 20 wt% SnO2

6.1 Introduction

Magnesium hydride (MgH_2) is a promising material for the chemical storage of hydrogen **(Jain, Lal, & Jain, 2010)** **(Varin, Czujko, & Wronski, 2006)** **(Oelerich, Klassen, & Bormann, 2001)** **(Barkhordarian, Klassen, & Bormann, 2004)** **(Fukai, 1993)**, as it combines low cost with high gravimetric hydrogen density (7.66 wt%), high volumetric hydrogen density (110 kg/m3), and reversible reaction with hydrogen **(Malkaa, Czujko, & Bystrzycki, 2010)** **(Imamura, et al., 2009)** **(Hanada, Ichikawa, Orimo, & Fujii, 2004)**. However, the slow hydrogen kinetics, high desorption temperature and high thermodynamic stability ($\Delta H = -75$ kJ/mol) **(Fátay, Spassov, Delchev, Ribárik, & Révész, 2007)** **(Buschow, Bouten, & Miedema, 1982)** still limit the possible industrial application of MgH_2 for hydrogen storage. Several methods have been proposed in the literature to improve the hydrogen desorption properties of MgH_2 **(Guo, Shang, & Zinsou, 2008)**, among which the introduction of structural defects by high energy ball milling seems the most promising **(Oelerich, Klassen, & Bormann, 2001)** **(Huot, Liang, Boily, Van Neste, & Schulz, 1999)** **(Sakintuna, Lamari-Darkrim, & Hirscher, 2007)**. In fact, milling creates extra channels for hydrogen desorption via structural defects such as grain boundaries and dislocations, leading to an easier desorption **(Varin, Czujko, & Wronski, 2006)** **(Zaluska, Zaluski, & Ström-Olsen, 1999)**. Literature data show that milling reduces the desorption temperature of 64 K and lowers the activation energy from 156 to 120 kJ/mol **(Huot, Liang, Boily, Van Neste, & Schulz, 1999)**.

A further catalytic effect on the hydrogen kinetics can be obtained by milling MgH2 together with e.g. transition metals **(Malka, Czujko, & Bystrzycki, 2010)** **(Zheng, et al., 2007)**, metal halides **(Malkaa, Czujko, & Bystrzycki, 2010)** **(Malka, Czujko, & Bystrzycki, 2010)** **(Zaluska, Zaluski, & Ström-Olsen, 1999)** **(Jin, Shim, Cho, & Yi, 2007)** and metal oxides **(Sakintuna, Lamari-Darkrim, & Hirscher, 2007)** **(Hanada, Ichikawa, & Fujii, 2005)** **(Dufour & Huot, 2007)** **(Patah, Takasaki, & Szmyd, 2009)** **(Jung & Lee, 2006)**. Among the oxides, the most effective seem to be Nb_2O_5, Fe_3O_4, V_2O_5, Mn_2O_3, Cr_2O_3, TiO_2, Sc_2O_3, Al_2O_3, CuO and SiO_2 **(Oelerich, Klassen, & Bormann, 2001)** **(Barkhordarian, Klassen, & Bomann, 2003)**, although the real catalytic mechanism of metal oxides is not yet clear. In this chapter, different amounts of MgH_2 and SnO_2 were ball milled together to prepare a set of SnO_2/MgH_2 mixtures. The catalytic effect of SnO_2 on the hydrogen desorption properties of MgH_2 was studied.

6.2 General aspects of hydrogen storage energy

One of the main reasons of the global warming is the emission of CO_2 which is a direct result of the fossil fuels' burning. In 1990, 20.7 billion tons of CO_2 was emitted and this amount increased to 32.5 billion tons in 2006 **(Guoa, Shang, & Aguey-Zinsou, 2008).** In addition to the climate change resulted from the fossil fuels, the growing demand for the energy necessitates the research in energy area in order to find an alternative energy source satisfy some energy requirements. These requirements include the energy source availability, cost, clean and flexibility. The clean new energy sources are wind, solar, geothermal, hydrogen, etc. Among these new energy sources, hydrogen is considered a very promising candidate justifies most of the energy requirements and much more appropriate for vehicles and transport applications. Whilst it is available with large amount in the sea water and can be produced in easy and flexible routes. Moreover from the environmental point of view, it produces a null side effect as the resultant exhaust from the hydrogen fuel cell is only water (**figure 6.1**). Hydrogen also contains a very high energy density comparable with the gasoline energy density (**figure 6.2**).

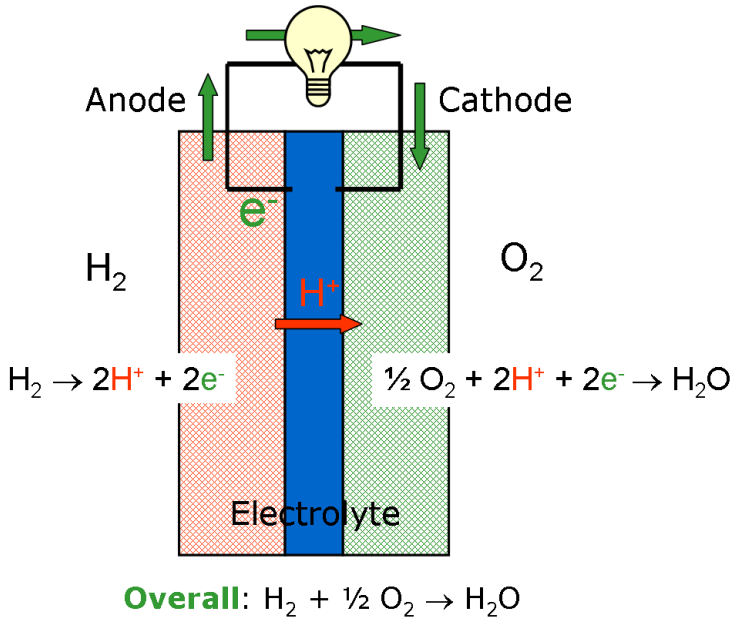

[6]Figure 6.1 *A schematic representation for hydrogen fuel cell*

[6] Figure reference: http://addis.caltech.edu/research/FCs%20for%20sustain%20energy.html

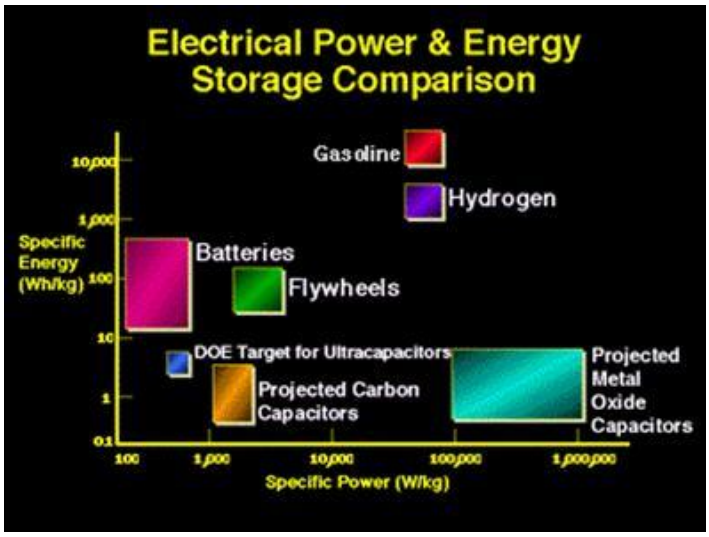

[7]**Figure 6.2** *Hydrogen energy density compared to other energy systems*

Hydrogen economy is consisted of five main subjects; its production, delivery, storage, conversion and applications **(Read, Thomas, Ordaz, & Satyapal, 2007)**. Although hydrogen covers many of the energy requirements, it is still a challenge to be used in markets because of its storage difficulties. In particular its storage includes the delivery, conversion and applications subjects. Especially the later requires an intensive care from the safety side in transports and vehicles. Hydrogen can be found in three phases and it depends on the temperature and pressure factors as shown in **figure 6.3**. At the ambient conditions, hydrogen performs gas phase so it has low density and consequently low energy density. Also the volume required storing one kg of hydrogen gas at room temperature and atmospheric pressure is 11 m^3 which is anther limitation in real applications. Volume criterion can be partially solved by compressing hydrogen but it has two problems in this case related to the tank material and the safety considerations. Container material is an issue because hydrogen performs a chemical reaction with most of metals under high pressure that is needed for the compression. The safety criterion specifically has a paramount human importance and this can-not be justified by liquid compressed hydrogen tanks. The best way then to store hydrogen is when it reacts chemically with materials perform at transit solid state phase to be a bridge between storage and applications stages. Actually, hydrogen reacts chemically with many candidates with high volumetric and gravimetric ratios as shown in **figure 6.4.**

[7] Figure reference: "http://www.see.murdoch.edu.au/resources/info/Tech/enabling/index.html"

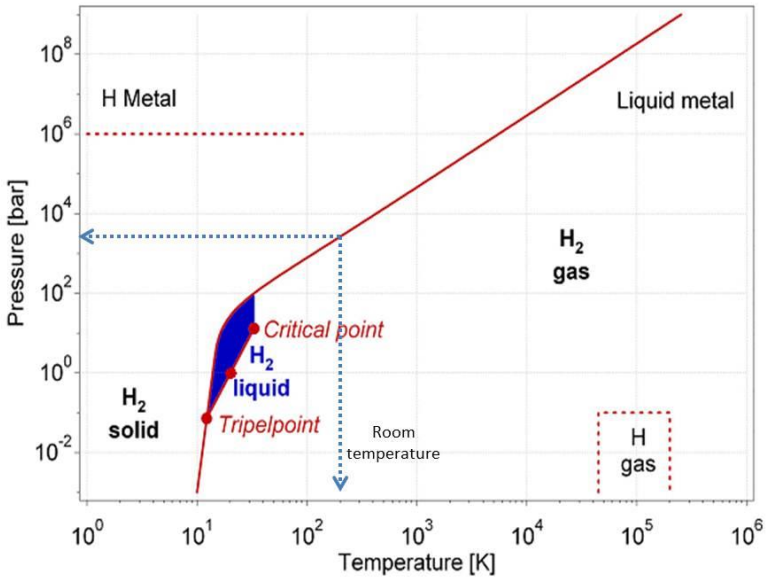

Figure 6.3 *Hydrogen phase diagram*

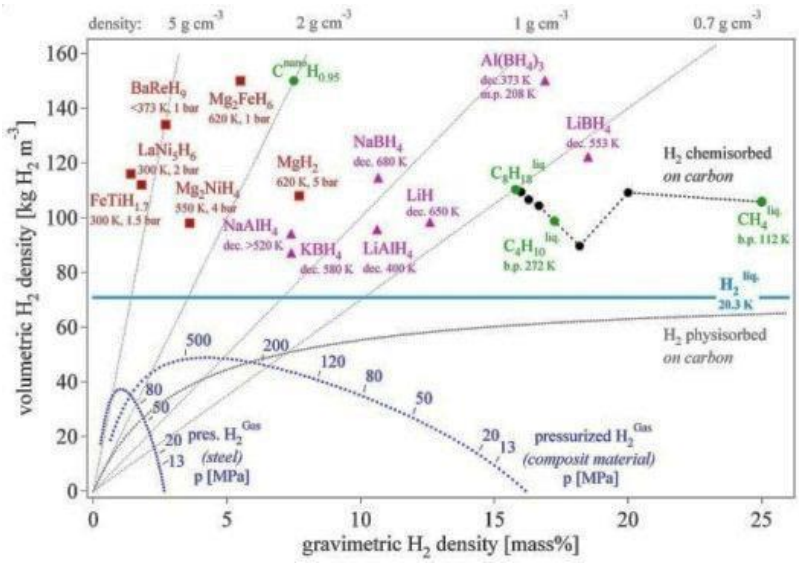

[8]**Figure 6.4** *Volumetric and gravimetric hydrogen density for selected hydrogen storage materials*

In order to select the best candidate for hydrogen storage, it is necessary to highlight the main aspects of interest that candidate has to stratifies in the storage subject and they can be pointed as follows **(Guoa, Shang, & Aguey-Zinsou, 2008) (see also table 6.1)**

- High hydrogen capacity ($> 6\ or\ 9\ gravimetric\ \%$)

[8] Figure reference: **(Guoa, Shang, & Aguey-Zinsou, 2008)**

- Low thermodynamic stability (*low desorption temperature* $< 150\ °C$ *under a moderate pressure*)
- High kinetics for hydrogen absorption/desorption (*around 5 minutes refilling time*)
- High stability against Oxygen and moisture (*i.e. long cycle life* > 500 *cycles*)
- Good thermal conductivity (*for rapid condition of sorption heat*)
- Low cost

[9]**Table 6.1** *Hydrogen storage parameters requirements according to the U.S Department Of Energy (DOE)*

Storage Parameter	2005	2010	2015
Gravimetric Capacity (Specific energy)	1.5 kWh/kg 0.045 kg H_2/kg	2.0 kWh/kg 0.060 kg H_2/kg	3.0 kWh/kg 0.090 kg H_2/kg
System Weight:	***111 Kg***	***83 Kg***	***55.6 Kg***
Volumetric Capacity (Energy density)	1.2 kWh/L 0.036 kg H_2/L	1.5 kWh/L 0.045 kg H_2/L	2.7 kWh/L 0.081 kg H_2/L
System Volume:	***139 L***	***111 L***	***62 L***
Storage system cost	$6 /kWh	$4 /kWh	$2 /kWh
System Cost:	***$1000***	***$666***	***$333***
Refueling rate	.5 Kg H_2/min	1.5 Kg H_2/min	2.0 Kg H_2/min
Refueling Time:	***10 min***	***3.3 min***	***2.5 min***

Although many candidates can be used to store hydrogen in a solid state phase (**see figure 6.4**), none of them satisfy all practical requirements. But also there are sufficiently good candidates meet some of the practical targets whilst the other targets are still under research scope to be improved. The tuned parameters to improve the storage properties are mainly the structure, chemistry and diffusion paths **(Guoa, Shang, & Aguey-Zinsou, 2008).** The structure by means crystalline size, degree of crystallinity, structural defects, etc. The chemistry improvement refers for example to the catalytic effect of several additives. The diffusion path herein refers to the path that hydrogen takes to be desorbed or absorbed which in turn related also to the structural defects and chemical enhancement.

[9] Reference: http://en.wikipedia.org/wiki/Hydrogen_storage

Looking insight at the general mechanism of hydrogen-metal reaction (**figure 6.5**), hydrogen molecules in the gas form firstly is absorbed physically by the surface. Due to this surface absorption, hydrogen atoms leave their molecules and individual atoms accommodate the metal surface. Hydrogen diffuses in metal as individual atoms much easier than in case molecules form. The diffused hydrogen atoms in metals then form a temporary solid solution phase called α-phase with low hydrogen density and later on α-phase is transformed into β phase after complete hydrogen diffusion.

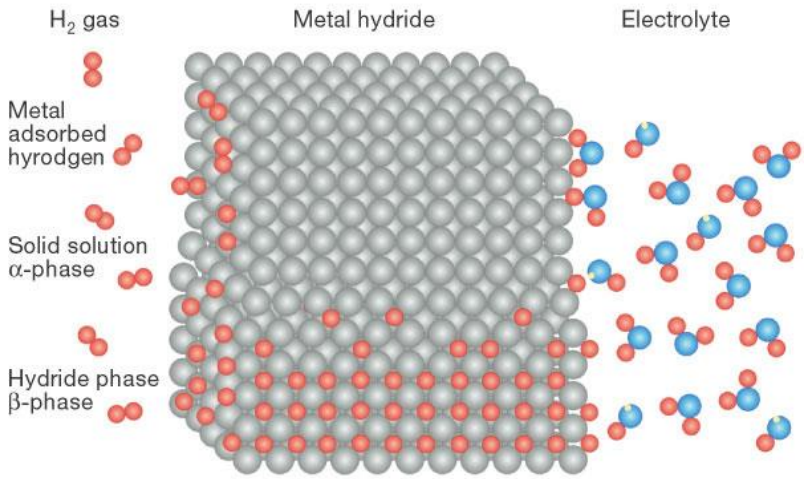

[10]**Figure 6.5** *Processes of hydrogen sorption in metals*

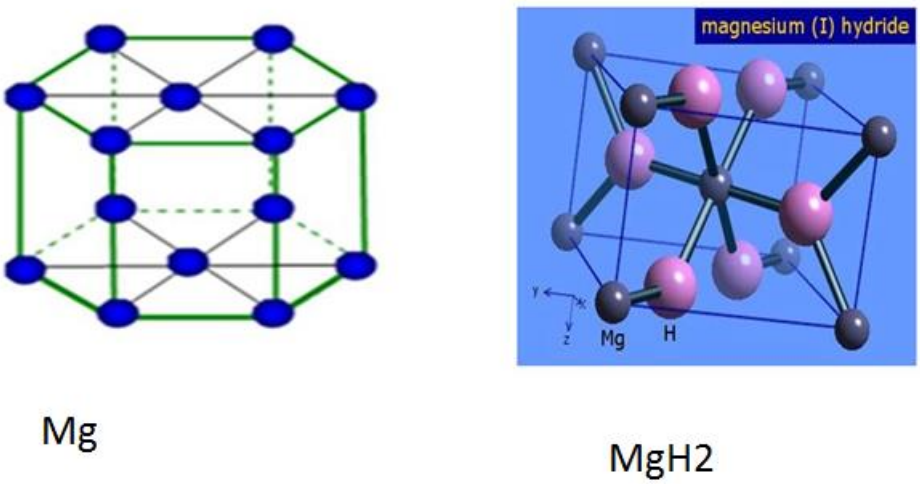

Figure 6.6 *Crystal unit cells of Mg (hexagonal [P63/mmc]; a = b = 3.0927 A, c = 5.21033 A) and β-MgH_2 (tetragonal [P42/mnm]; a = b = 4.514, c = 2.992 A)*

[10] Figure reference: http://www.fuelcell.sg/hydrogen.php

Among several storage candidates, Mg has many storage advantages already have been mentioned in the introduction section mainly low cost, high gravimetric and volumetric hydrogen densities and reversibility. In the other hand, hydrogen's slow kinetics in Mg and its high thermodynamic stability (i.e. high desorption/absorption temperature) still a challenge

Mg has a hexagonal crystal structure (**figure 6.6**) that transforms into tetragonal (**figure 6.6**) when hydrogen atoms are fully dissociated in the Mg unit cell. Two factors limit the diffusion in hydrogen in Mg **(Guoa, Shang, & Aguey-Zinsou, 2008)**, firstly the formation of oxide layer on the Mg particles' surface. Secondly, the hydrogen-metallic layer that forms after a while of hydrogen diffusion also limits further diffusion **(Berlouis, Cabrera, Hall-Barientos, Hall, Dodd, & Morris, 2001)**. An enhancement in the diffusion could be achieved by introducing structural defects and decreasing size so hydrogen can find additional paths to diffuse **(Berube, Radtke, Dresselhaus, & Chen, 2007)**. Hydrogen paths are shortening for smaller Mg particles than for large particles. Further enhancement in Mg storage properties can be reached by alloying with several catalysts as already mentioned in the introduction.

6.3 Experimental details

Commercial magnesium hydride ($MgH_2 \geq 96.5\% -$ Sigma Aldrich) and Tin (IV) Oxide (SnO_2 99.9% − Sigma Aldrich) powders were employed. To minimize the oxidation, handling and processing were carried out under Ar atmosphere inside a glove box. A first set of five samples (set A in the following) was prepared by adding 0, 5, 10, 15, and 20 g of SnO2 to 100 g of MgH_2. The powder mixtures were milled for 16 h in a Fritsch Pulverisette 4 planetary ball mill under static Ar atmosphere employing a hardened Cr steel milling set (80 cm^3 bowl and ø12 mm balls). A total of 10 balls and a 1:47 powder-to-ball weight ratio were employed. A second set of three samples (set B in the following) was prepared by pre-milling the pure SnO_2 powder for 8, 32 and 64 h before mixing it with MgH_2; these last samples, produced with 17.6 g of SnO_2 added to 100 g of MgH_2 (i.e. 15 wt% SnO2 and 85 wt% MgH_2) were then milled further for 3 h under static Ar atmosphere. X-ray diffraction data were collected on a Rigaku PMG/VH diffractometer using a long fine-focus Cu tube operated at 40 kV and 30 mA. The machine is equipped with 1° divergence slit, 2° primary and secondary Soller slits, 1° antiscatter slit and a 0.15 mm receiving slit and a bent (002) graphite crystal analyzer: the optics guarantee a narrow and symmetric instrumental profile over a wide 2θ range. Diffraction data were measured in steps of 0.05_ with a fixed counting time of 5 s per step. Phases were identified using the PANAlytical HighScore 2.2 software and the ICDD PDF-2 database. The Bruker TOPAS v. 4.2 software (based on the Rietveld method **(Young, 1993)**) was

used for the quantitative phase analysis whereas the PM2K program **(Leoni, Confente, & Scardi, 2006)** implementing the Whole Powder Pattern Modeling (WPPM) **(Scardi & Leoni, 2002) (Scardi & Leoni, Diffraction Analysis of the Microstructure of Materials, 2004) (Leoni, Martinez-Garcia, & Scardi, 2007)** was employed for microstructure analysis. Thermogravimetric (TG) and Differential Thermal Analysis (DTA) were performed on a Setaram LabSys thermobalance under 120 cm^3/min He flux (99.999% purity) by means of a Matheson electronic mass flow system. Measurements were carried out from 20 °C up to 500 °C for all specimens. The powders were weighted, loaded into 0.1 cm^3 alumina crucibles and sealed with Parafilm. The crucibles were then fixed in the thermobalance together with an a-Al_2O_3 reference (8.7 mg): the sealing film was quickly removed just before closing the thermobalance which was immediately purged with He.

The TG-DTA unit-system was coupled to a TRIO-1 VG quadrupole Mass Spectrometer (MS) through a homemade transfer line, based on an empty deactivated-silica capillary column (0.32mm internal diameter; 16m length) enveloped in a thermostatic jacket kept at 250 °C **(Campostrini, Sicurelli, Ischia, & Carturan, 2007).** The MS is employed for an accurate measurement of hydrogen desorption. Electron impact mass spectra (70 eV) were recorded every second in the 1e400 amu range (ionization chamber temperature 200 °C). The calibration of the quadrupole MS was done weekly using Heptacos (perfluorotributylamine) as a reference, while parameters were optimized daily with particular attention to the improvement of the He signal. A 5% H_2/N_2 mixture was employed to test the instrument sensibility to H_2.

6.4 Results and discussion

6.4.1 Phase analysis

Phase content of the specimens was characterized by X-ray powder diffraction. Four phases can be identified in the starting MgH_2 powder as taken from the purchased bottle stored under the same environment as the prepared samples: β-MgH_2, $Mg(OH)_2$ (brucite), MgO (periclase) and metallic Mg (**see figure 6.7**). The Rietveld method was employed for Quantitative Phase Analysis (QPA) of the crystalline phases. The technique can provide direct information on the crystalline phases only: this should be taken into account in the analysis of the results, especially if the presence of an amorphous phase cannot be excluded. Rietveld QPA (cf. **Table 6.2**) shows that the major crystalline constituents are MgH_2 (ca. 88.2 wt%) and $Mg(OH)_2$ (ca. 7.8 wt%). This is partly

in agreement with the specifications of the purchased MgH_2, the main difference being the presence of $Mg(OH)_2$. The latter is most likely the result of the oxidation of a fraction of the original MgH_2: despite all measures taken to avoid it, oxidation may have occurred in the glove box (e.g. due to the residual oxygen present in the Ar bottle) or, more likely, during the preparation of the specimen for XRD measurement. The occurrence of $Mg(OH)_2$ has been already reported in the literature both on unmilled **(Varin, Jang, Czujko, & Wronski, 2010)** and milled MgH_2 powders.

Table 6.2 *Rietveld QPA results for the specimens studied in this work. The estimated standard deviation for the measurement is of the order of 1 wt%.*

Sample label	**Nominal SnO_2 wt%**	**β-MgH_2 wt%**	**γ-MgH_2 wt%**	**MgO wt%**	**$Mg(OH)_2$ wt%**	**Mg wt%**	**cryst. SnO_2 wt%**	**amorph. SnO_2 wt%**
as received MgH_2		88.2		2.2	7.8	1.8		
milled MgH_2		79.9	14.1	6.0				
A-SnO_2(5%)	4.76	77.9	4.2	13.5			4.4	
A-SnO_2(10%)	9.09	71.3	4.8	14.2			9.7	
A-SnO_2(15%)	13.04	65.3	4.2	16.8			13.7	
A-SnO_2(20%)	16.67	62.8	4.2	16.2			16.8	
B-SnO_2(8h)	15	69.2	7.0	16.3			7.5	
B-SnO_2(32h)	15	65.7	8.5	19.5			6.3	
B-SnO_2(64h)	15	70.9	7.6	16.5			5.0	
rescaled B values accounting for missing (crystalline) SnO_2								
B-SnO_2(8h)	15	63.6	6.4	15.0			6.9	8.1
B-SnO_2(32h)	15	59.6	7.7	17.7			5.7	9.3
B-SnO_2(64h)	15	63.4	6.8	14.8			4.5	10.5

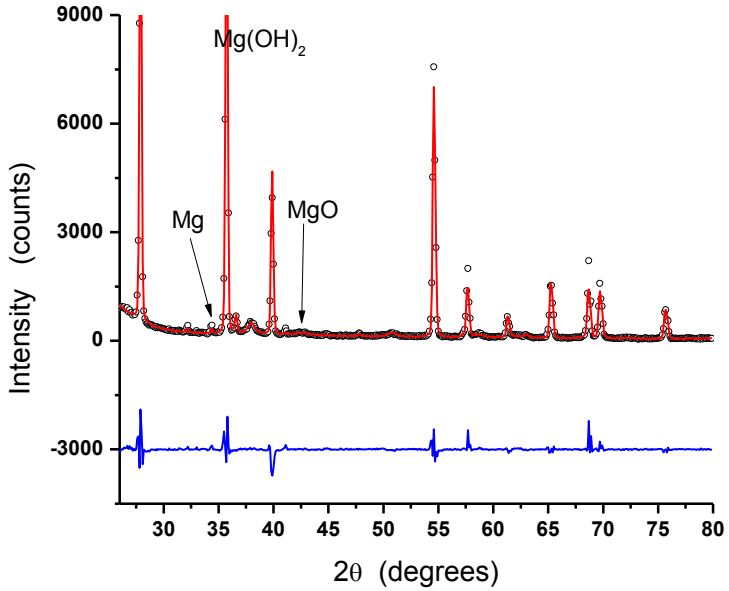

Figure 6.7 *XRD pattern of pristine MgH_2, arrows show the additional phases (Mg, MgO, $Mg(OH)_2$) presented rather than β-MgH_2*

Milling of the powder (**Table 6.2**) causes the partial transformation of the tetragonal β-MgH_2 into the orthorhombic γ-MgH_2 polymorph. This transformation has already been observed in the literature, and is attributed to the high compressive stresses developed by the milling process **(Huot, Liang, Boily, Van Neste, & Schulz, 1999)** **(Bastide, Bonnetot, Letoffe, & Claudy, 1980)** **(Nayeb-Hashemi, 1988)**. A larger quantity of MgO is present in the milled powder with respect to the pristine one. This extra MgO results both from the oxidation of Mg in the hydride and from the possible conversion of $Mg(OH)_2$ into MgO with the release of water. Brucite and magnesium are possibly converted into magnesium oxide or into an amorphous phase (that cannot be evaluated). The quantitative phase analysis results are in good agreement with literature data **(Huot, Liang, Boily, Van Neste, & Schulz, 1999)** (74 wt% β-MgH_2, 18 wt% γ-MgH_2, 8 wt% MgO) obtained for a different powder (95% MgH_2, 5% Mg from Th. Goldschmidt AG), type of mill (Spex 8000 shaker mill) and milling conditions. This is a possible indication that in both cases MgH_2 reached a steady state that depends only on the material and on the mechanical properties.

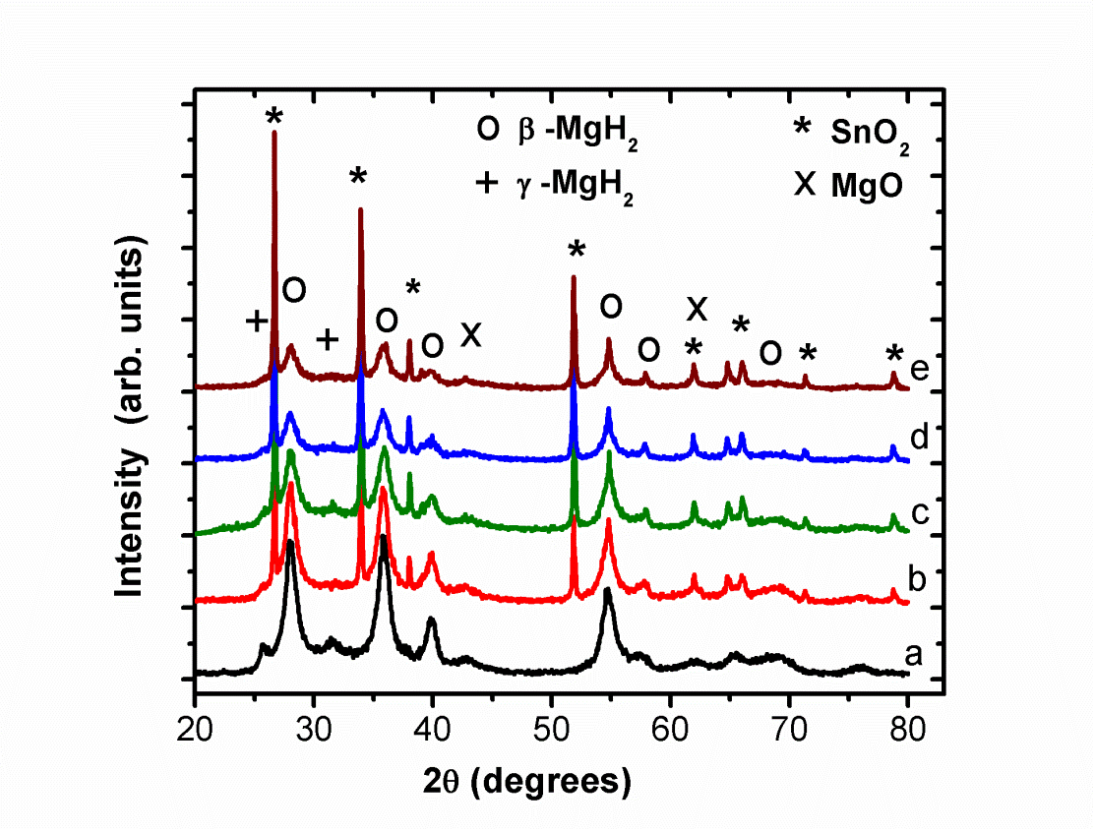

Figure 6.8 *Comparison of the XRD patterns for (a) ground MgH_2, (b) A-SnO_2(5%), (c) A-SnO_2(10%), (d) A-SnO_2(15%), (e) A-SnO_2(20%)*

The situation changes slightly for the SnO_2/MgH_2 samples of set A (see **Figure 6.8** and **Table 6.2**): both MgO and γ-MgH_2 are present together with SnO_2. The QPA (cf. **Table 6.2**) indicates that SnO_2 distributes homogeneously in the mixtures and its amount is preserved during milling: in fact, the SnO_2 wt% obtained from the XRD analysis is in good agreement with the nominal values adopted for the preparation of the powders (**cf. Figure 6.9**). The quantity of γ-MgH_2 is significantly lower in the ground set A than in the milled MgH_2. The simultaneous milling with SnO_2 is therefore beneficial to stabilize the β-MgH_2 towards the polymorphic transformation, but it seems also to favor the oxidation of the existing hydride (cf. **Table 6.2**). In fact, the MgO fraction grows steadily with the amount of cassiterite present in the mixture. The stabilizing effect of SnO_2 can be understood by considering the relative elastic properties of MgH_2 (E = 87.3 GPa, G =36.1 GPa, ν = 0.209 **(Jr, JF, & Wolf W, 2007)**) and SnO_2 (E = 218 GPa, G = 82.1 GPa, ν = 0.321 **(Caravaca, Casali, & Ponce, 2011)**): the milling energy is preferably employed to deform (mill) SnO_2 than MgH_2. The increase in surface area and defect content resulting from milling can also play an

important role in favoring the oxidation of the powder. On the other hand, MgH_2 and SnO_2 show little mutual chemical affinity as no reaction phases are identified from the powder diffraction patterns.

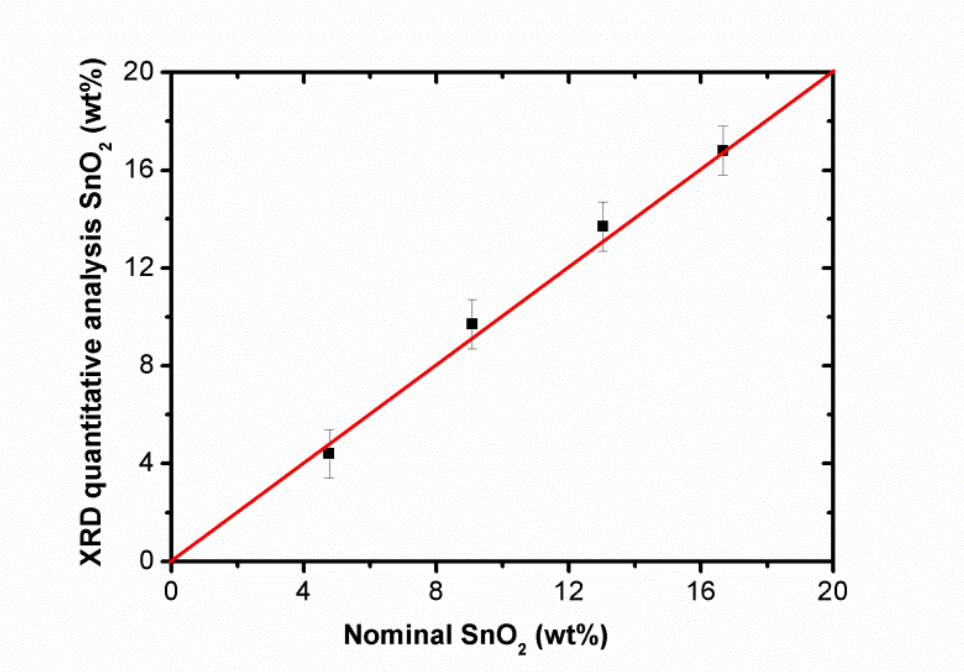

Figure 6.9 *Comparison of the nominal and Rietveld refined SnO_2 composition*

Table 6.3 WPPM results for SnO_2: mean diameter <D> and variance of the (lognormal) size distribution σ. Estimated standard deviations on the last significant digit are reported in parentheses.

Sample label	<D> SnO_2 (nm)	σ SnO_2 (nm^2)
A-SnO_2(5%)	82(2)	26(8)
A-SnO_2(10%)	29(3)	22(9)
A-SnO_2(15%)	22(4)	19(9)
A-SnO_2(20%)	17(4)	16(9)
B-SnO_2(8h)	5(1)	5(2)
B-SnO_2(32h)	5(1)	2(2)
B-SnO_2(64h)	4(2)	4(2)

The stabilizing effect of SnO_2 and the proposed mechanism are confirmed by set B (SnO_2 preliminary milled and then alloyed with MgH_2). In set B, cassiterite has a much smaller domain size (cf. **Table 6.3**): this results in a reduced capacity to absorb the milling energy and therefore to prevent the conversion of β-MgH_2 into γ-MgH_2. The QPA values obtained from the Rietveld analysis (cf. **Table 6.2**) cannot be directly used for a comparison to set A: a large fraction of SnO_2 seems in fact missing in the atomic balance. To preserve matter, we therefore assumed that the missing cassiterite is no longer crystalline and we rescaled the weight fractions accordingly (cf. values at the bottom of **Table 6.2**). The quantity of γ-MgH_2 is higher in set B than in the set A, but still lower than in the milled pristine powder. The amount of periclase in the specimens is confirmed to be related to the nominal quantity of cassiterite in the mixture, in agreement with the values obtained for set A: the values for set B should in fact correspond to an ideal A-SnO_2(17.6%) case.

6.4.2 Hydrogen desorption

Hydrogen desorption features can be evaluated by the trend of TG-DTA curves and from the simultaneously collected MS data. DTA-TG data were collected for all specimens under He flow with a heating rate of 10 K/min: the main results concerning the onset temperature, the temperature of the desorption peak (from DTA) and the weight percent of desorbed hydrogen (from IC m/z=2 band of MS) are tabulated in **Table 6.4**.

Table 6.4 *TG-DTA-MS analysis: onset and peak temperatures of DTA for set A and B samples. Four values for the weight percent of desorbed hydrogen are given, referred to (i) the nominal MgH_2, (ii) the quantity of β+γ-MgH_2 obtained from XRD, (iii) the sole quantity of β-MgH_2 and (iv) the total weight of the specimen. The estimated standard deviations are of 1 °C for temperatures and 0.1% for hydrogen content.*

Sample		T_{onset} (°C)	T_{peak} (°C)	Hydrogen wt% nominal MgH_2	Hydrogen wt% XRD total MgH_2	Hydrogen wt% XRD β-MgH_2	Hydrogen wt% total wt
A	as received MgH_2	433	444	7.1	7.8	7.8	6.9
	Milled MgH_2	365	379	4.1	4.4	5.1	4.1
	A-SnO_2(5%)	370	381	3.9	4.5	4.8	3.7
	A-SnO_2(10%)	360	378	5.0	6.0	6.4	4.5
	A-SnO_2(15%)	356	386	4.7	5.9	6.3	4.1
	A-SnO_2(20%)	359	382	5.5	6.8	7.3	4.6
B	B-SnO_2(8h)	365	383	5.0	6.1	6.7	4.3
	B-SnO_2(32h)	365	383	5.5	6.9	7.8	4.7
	B-SnO_2(64h)	358	374	5.3	6.4	7.1	4.5

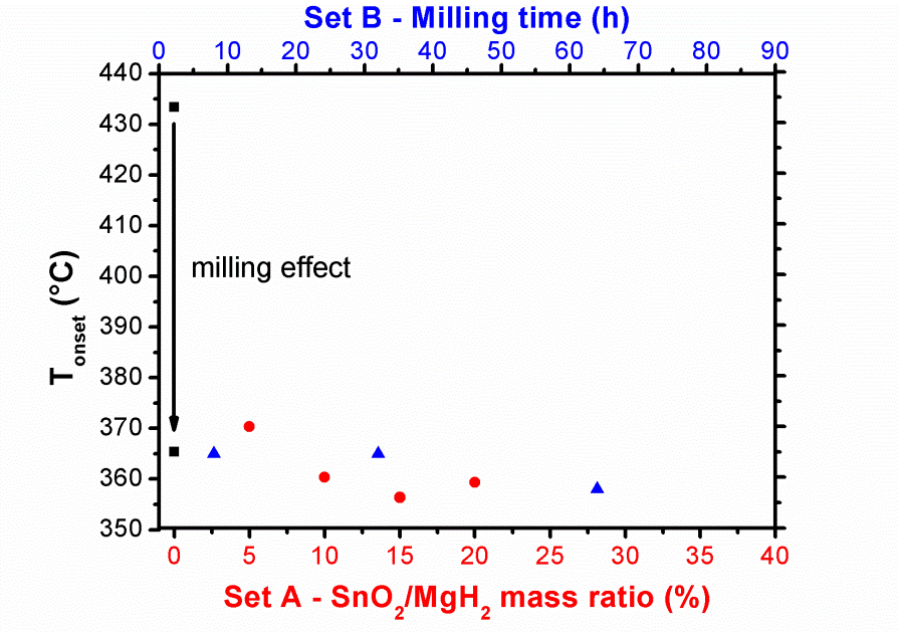

Figure 6.10 *Onset desorption temperature as a function of SnO_2 mass ratios (set A) and milling time (set B). Pure MgH_2 (square), set A (dot), set B (triangle).*

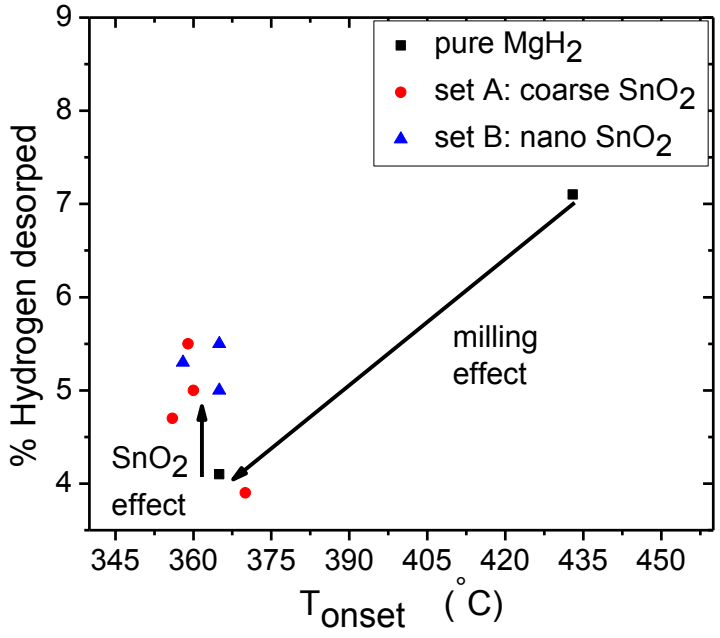

Figure 6.11 *Correlation between onset temperature (from DTA-data) and released hydrogen amount (from TG-data). Pure MgH_2 (square), set A (dot), set B (triangle).*

Recorded data (see the DTA-T_{onset} trend in **Figure 6.10**) indicate a clear improvement in the desorption temperature due to milling, independently of the content of SnO_2. The addition of the oxide has a minor effect that seems to saturate quickly with the amount of added oxide. However (see **Figure 6.11**), milling pure MgH_2 leads to a remarkable reduction in the quantity of desorbed hydrogen: cassiterite is effective in limiting this effect. Thus both **Figures 6.10 and 6.11** are necessary to give a complete picture of both the effect of milling and of the addition of the catalyst. Although the real catalytic mechanism of oxide species is not fully understood, a clear advantage of the SnO_2 presence is to prevent the agglomeration of MgH_2 with small-sized β-MgH_2 crystallites during the milling process, an effect clearly detrimental to the hydrogen desorption properties. As desorption proceeds from the surface towards the interior, milling and therefore refining the MgH_2 particles has a beneficial effect, visible in terms of lower desorption temperature. This is claimed by some authors **(Guo, Shang, & Zinsou, 2008)** as one of the positive effects of adding oxides to MgH_2. The destruction of the hydroxide layer which is an obstacle to desorption is a further result obtained by the addition of oxides to MgH_2. The amount of desorbed hydrogen referred to the total MgH_2 present, increases with increasing SnO_2 amount and reaches a maximum (6.8 wt%) for the A-SnO_2(20%) sample. This is a further validation of the mechanism of action of SnO_2 proposed here: SnO_2 acts as a lubricant for MgH_2 during milling, absorbing part of the impact energy and keeping the milling temperature down, therefore decreasing the probability of losing hydrogen during milling. If we assume that the β-MgH_2 phase is the one actually releasing hydrogen, then (**cf. Table 6.4**) we see that the effect of SnO_2 is to counterbalance the action of milling. This in turn suggests that it might be possible to perform a co-milling using SnO_2 and another (stronger) catalyst to combine the action of the two. However, SnO_2 adds extra weight but does not carry any hydrogen; some evaluation should therefore be done also on the specific capacity referred to the total weight of the specimen. The result is slightly biased, as the pristine specimen is not 100% pure (it contains just 88.2% of MgH_2): nevertheless we still see an increase from 4.1 to 4.6 wt% (referred to the total weight) with the addition of SnO_2.

Pre-milling SnO_2 before mixing it with MgH_2 (set B) has a positive influence on the quantity of hydrogen that can be effectively desorbed. The amount of hydrogen desorbed in set B was in fact relatively high compared to set A, except for A-SnO_2 (20%). This could be connected to milling time being 3 hours for set B and 16 hours for set A: the time allowed for losing hydrogen is therefore expected to be longer in set A than in set B. The H_2-desorption temperature decreases rapidly, even for the sample with SnO_2 powder preliminarily milled for 8 hours. Further milling seems to have only a marginal effect, probably because the efficiency limit of the milling process has been already reached (cf. **Table 6.4**).

From the results of **Table 6.4** and **Figure 6.11**, the overall best performance (best tradeoff between reduction of the desorption temperature and amount of desorbed hydrogen) is achieved with sample A-SnO_2(20%). The desorption kinetics of A-SnO_2(20%) was therefore analyzed in detail; TG-DTA analysis was done at different heating rates (7, 10, 13, 16, 19, 22, 25 K/min) and compared with analogous analyses (10, 13, 16, 19, 22 K/min) done on the as received MgH_2. The heating-rate dependency of the desorption temperature can be related to the activation energy of the process via Kissinger equation $\ln\left(b/T_p^2\right) = A - E/RT$ where b is the heating rate, T_p is the desorption temperature, *E* is the activation energy, *R* is the molar gas constant (8.3144621 J/(mol K)) and *A* is a constant. It is customary to represent Kissinger equation in graphical form (Kissinger plot) as shown in **Figure 6.12** for pure MgH_2 and A-SnO_2(20%) specimens.

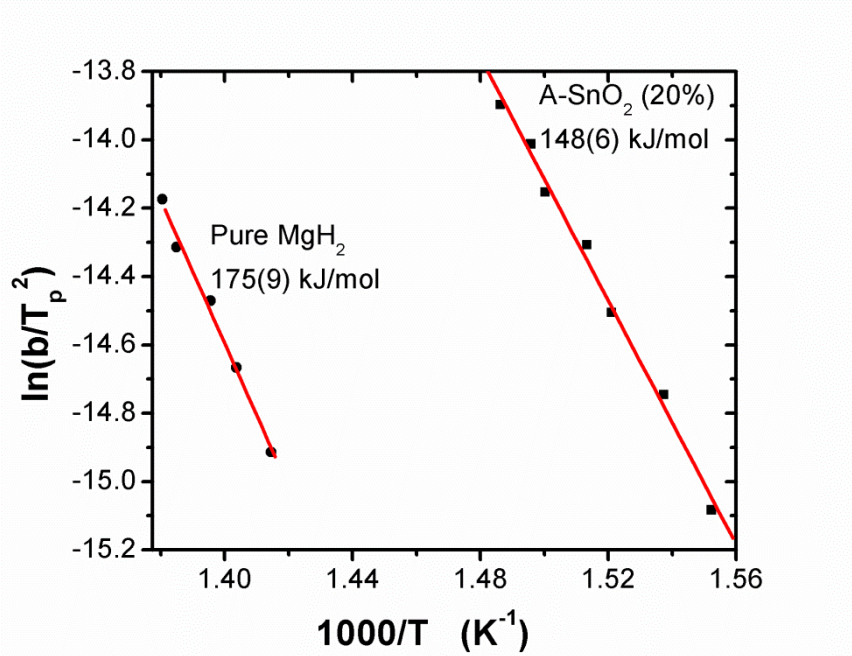

Figure 6.12 *Kissinger plot for pure unmilled MgH_2 and SnO_2/MgH_2-20% samples*

The activation energy, calculated from the slope of the plot, is 148(6) kJ/mol for A-SnO_2(20%) sample. This energy value, associated to H_2-desorption process characterized by a peak-temperature of 386 ^oC (for a heating rate of 16 K/min), is lower than that of the pure, pristine MgH_2 powder, which is 175(9) kJ/mol, correlated to a T_{peak} of 444 ^oC at 16 K/min. It is well known that the value of activation energy depends on the methodology of calculation, and literature data on E-values for pure MgH_2 roughly lie in the range 156-206 kJ/mol **(Huot, Liang, Boily, Van Neste, & Schulz,**

1999) (Gabis, Dobrotvorskiy, Evard, & Voyt, 2011) (Zaranski & Czujko, 2011). Our experimental results then indicate that the mixing and milling of commercial MgH_2 powders with a 20% of SnO_2 as catalyst-species yields beneficial effects quantified by a net decrease in both the H_2-desorption temperature (58 K) and in the activation energy (27 kJ/mol).

6.5 Conclusions

Milling of MgH_2 is beneficial as it increases the surface area, it introduces defects and it reduces the amount of hydroxide found in the starting powder, with a consequence of lowering the H_2 desorption temperature.

The use of SnO_2 as an additive for the milling can increase those beneficial effects. In the form of coarse powder, SnO_2 can effectively act as a lubricant for the milling of β-MgH_2, thus reducing the quantity of material converted into γ-MgH_2. When added as a milled nanocrystalline powder, SnO_2 has a milder effect in reducing the impact energy on MgH_2, which in turn must undergo its destabilization and transformation into the γ polymorph.

As a net result, the combined effect of milling and of SnO_2 addition is to decrease the onset temperature for hydrogen desorption by ca. 60 K (ca. 10% decrease) and to stabilize the MgH_2 present. A gain is also seen in the relative quantity of hydrogen that can be released. The best compromise is obtained with a mixture containing 20% SnO_2, where the activation energy for desorption lowers from 175(9) kJ/mol (pristine MgH_2) to 149(5) and the desorbed hydrogen from the MgH_2 present lowers from 7.8 wt% to 6.8 wt% (reduction from 6.9 to 4.6 wt% if referred to the total weight). It is therefore inferred that SnO_2 could be used as low-cost lubricant additive to MgH_2, in association with a further catalyst.

CHAPTER VII

Activation Energy in the Thermal Decomposition of Magnesium Hydride Powders by TG-MS Coupled Measurements

R. Campostrini, M. Abdellatief, M. Leoni & P. Scardi

Part of this chapter was submitted to:

Journal of Thermal Analysis, (2013)

Abstract

Thermal decomposition of MgH_2 was investigated by combined Thermogravimetry-Mass Spectroscopy (TG-MS), Differential Thermal Analysis (DTA) and Differential Thermogravimetry (DTG). Three main vapour phases – H_2O, CO_2, and H_2 – evolved from MgH_2 at different temperatures. The activation energy for each of these events was obtained by using several known equations (Kissinger-Akahira-Sunose; Flynn-Wall-Ozawa; Starink; Friedman), derived from model-free iso-conversion methods and applied to experiments performed at constant heating rate. A comparison between the most general methods for activation energy calculation is then studied at three iso-conversion reference points: onset, fixed transformed fraction, maximum transformation rate.

7.1 Introduction

As already shown in the previous chapter, hydrogen storage in metals in general, and more specifically in Mg, has a great potential as a new clean, powerful, and available energy storage method. Investigations on hydrogen sorption/desorption processes focus on the determination of kinetics parameters, such as reference temperatures, from which an activation energy can be calculated. Unfortunately Mg is very sensitive to ambient conditions, as it reacts with oxygen forming an oxide layer which inhibits and limits hydrogen diffusion, and consequently negatively influences the sorption/desorption kinetics. Therefore, studying other secondary gas evolutions in the thermal analysis is not less important than studying H_2 release, because other gases can give a complementary description of the final hydrogen activation energy.

The literature provides several methods and equations to calculate the activation energy, leading to a range of possible values. Main differences are due to the intrinsic accuracy of the different methods, which is turn depend on the validity of some mathematical approximations, as well as to the operative and instrumental conditions, and to the temperature interval of the observed event. All of this has quite an impact on hydrogen storage technology. As a consequence, following the seminal work of Starink **(Starink, 2003)** **(Starink, 2007)**, the present chapter is dedicated to a discussion of theoretical and methodological aspects relevant to the determination of the activation energy.

7.2 Methodological background

The most common assumption in kinetics studies of thermally activated reactions, like those occurring in solid state during linear heating treatments, is that the transformation rate ($d\alpha/dt$) is given by the product of two independent functions (**equation 7.1**). The first term on the right hand side of **equation 7.1** is ($k_o e^{-E/RT}$), and it depends on temperature only (following an Arrhenius law), while the second term, $f(\alpha)$, is called the reaction function and it depends only on the transformed fraction (α). $f(\alpha)$ is generally an unknown law, related to the kinetic model of the reaction.

$$\frac{d\alpha}{dt} = k_o e^{-E/RT} \cdot f(\alpha) \qquad (7.1)$$

where K_o is a constant, R is the universal gas constant and E is the activation energy.

Among the so called kinetic triplet parameters (k_o, E, $f(\alpha)$), in order to determine the activation energy (E) of reactions performed at constant heating rate ($\beta=dT/dt$), all reliable methods that were proposed in the literature require a correct choice of temperatures T_f corresponding to a fixed transformed phase fraction α. This can be evaluated by integrating **equation 7.1** (**see equation 7.2**).

$$\int_0^{\alpha} \frac{d\alpha}{f(\alpha)} = g(\alpha) = \frac{k_o}{\beta} \cdot \int_0^{T_f} e^{-E/RT} dT = \frac{k_o \cdot E}{\beta \cdot R} \cdot \int_{y_f}^{\infty} \frac{e^{-y}}{y^2} dy \qquad \textbf{(7.2)}$$

where $y = E/R \cdot T$ and $y_f = E/R \cdot T_f$

This method is labeled as iso-conversion of type B and its derivation relies on approximating the temperature (or Arrhenius) integral, $p(y)$:

$$p(y) = \int_{y_f}^{\infty} \frac{e^{-y}}{y^2} dy \qquad \textbf{(7.3)}$$

As a consequence, type B iso-conversion methods are affected by the inaccuracy in the temperature integral approximation. Many approaches have been reported in the literature concerning this integral approximation, valid in most cases for 15 < y < 60. Several mathematical expressions have been proposed, such as:

$$p(y) = \frac{e^{-y}}{y \cdot (\omega + y)} \left(1 + g(y)\right) \qquad \textbf{(7.4)}$$

where ω is a constant and $g(y)$ a suitable series expansion

7.2.1 Kissinger-Akahira-Sunose equation (type B-2):

Kissinger-Akahira-Sunose **equation 7.6** can be obtained by considering only the first term in the $g(y)$ expansion (**equation 7.5**), and assuming ω=0 in **equation 7.4** (i.e., the Murray-White approximation)

$$g(y) = \left(1 + \frac{2!}{-y} + \frac{3!}{(-y)^2} + \frac{4!}{(-y)^3} + \ldots\right) \qquad \textbf{(7.5)}$$

$$\ln\left(\frac{\beta}{T_f^2}\right) = \frac{-E}{R}\cdot\frac{1}{T_f} + C_2 \qquad (7.6)$$

$$; C_2 = \ln\left(\frac{k_0 \cdot R}{E \cdot g(\alpha)}\right) \qquad (7.7)$$

For experiments performed at different linear heating rates, **equation (7.6)** provides E from the slope of the trend of $\ln(\beta/T_f^2)$ plotted versus $1/T_f$.

7.2.2 Flynn-Wall-Ozawa equation (type B-0):

A second group of mathematical expressions adopts a linear approximation of the Arrhenius integral of the general type:

$$p(y) \cong \frac{e^{(-Ay+B)}}{y^k} \qquad (7.8)$$

where A and B are optimized values for the k exponent.

If Doyle approximation (i.e.: k=0; A=1.0518; B= –5.330) is assumed, then Flynn-Wall-Ozawa equation (type B-0) results (**equation 7.9**):

$$\ln \beta = 1.0518\frac{-E}{R}\cdot\frac{1}{T_f} + C_4 \qquad (7.9)$$

$$C_4 = -5.330 + \ln\left(\frac{k_o \cdot E}{R \cdot g(\alpha)}\right) \qquad (7.10)$$

Equation 7.9 provides E from the slope of $\ln \beta$ plotted versus $1/T_f$.

7.2.3 Starink equations (type B-1.95, B-1.92)

Starink procedure assigns the values of k, A, and B in **equation 7.8** to be (k=1.95, A=1 and B= –0.235). Recently, the new optimized values k=1.92, A=1.0008 and B= –0.3125 have been proposed, leading to the type B-1.95 and B-1.92 (**equation 7.11 and 7.12**):

$$\ln\left(\frac{\beta}{T_f^{1.95}}\right) = \frac{-E}{R}\cdot\frac{1}{T_f} + C_5 \qquad (7.11)$$

$$\ln\left(\frac{\beta}{T_f^{1.92}}\right) = 1.0008\frac{-E}{R}\cdot\frac{1}{T_f} + C_6 \qquad (7.12)$$

$$C_5 = -0.235 + \ln\left(\frac{k_o}{g(\alpha)} \cdot \left(\frac{R}{E}\right)^{0.95}\right) \quad \textbf{(7.13)}$$

$$C_6 = -0.312 + \ln\left(\frac{k_o}{g(\alpha)} \cdot \left(\frac{R}{E}\right)^{0.92}\right) \quad \textbf{(7.14)}$$

Thus, from Starink equations E values can be obtained from the slope when $\ln(\beta/T_f^{1.95})$ or $\ln(\beta/T_f^{1.92})$ is plotted versus $1/T_f$.

7.2.4 Friedman equation (type A)

A different approach can be proposed, based only on the knowledge of the reaction rate at an equivalent stage ($(d\alpha/dt)_f$ and its corresponding temperature T_f. The equations that are based on this approach are labeled as type A. An example belonging to type A is the Friedman equation (**equation 7.15**)

$$\ln(\beta \cdot d\alpha/dT) = \frac{-E}{R} \cdot \frac{1}{T_f} + C_1 \quad \textbf{(7.15)}$$

with $C_1 = \ln(k_o \cdot f(\alpha))$. The activation energy can be obtained from **equation 7.15** from the slope of a plot of $\ln(\beta \cdot d\alpha/dT)$ versus $1/T_f$ at different heating rates. This method is also called model-free because it does not involve any kinetic model assumptions, which could introduce some uncertainties in the values of conversion rate.

7.3 Experimental

Commercial magnesium hydride (96.5% purity) pure reagent was purchased from *Sigma-Aldrich* as-received (coarse powder). Samples were kept and handled under argon atmosphere (99.999% purity) working inside a glove-box. Thermogravimetric (TG) and differential thermal analyses (DTA) were performed on a *LabSys Setaram* thermobalance, between 20–500°C. Measurements were carried out fluxing the thermobalance furnace with a constant 120 $cm^3 \cdot min^{-1}$ He flow (99.999% purity), previously set at 20°C and 0.1 MPa. Thermal analyses were recorded using similar sample amounts (7–10 mg) and different linear heating rates: 7, 10, 13, 16, 19, and 22 °C/min. Handling the samples inside the glove-box, the powders were weighted and loaded into alumina sample holders (volume 0.1 cm^3), which were sealed with plastic packaging film

(*Parafilm*®). The filled crucibles were then fixed in the thermobalance together with α-Al_2O_3 as a reference (8.7 mg). The thermobalance was immediately closed and purged with the inert He flux. The He flow rate was adjusted and controlled by means a *Matheson* mass flow controller.

Mass spectrometric analyses were carried out using a *TRIO-1 VG* quadrupole mass spectrometer detector (QMD), connected with the thermobalance by a homemade transfer line **(Campostrini, Ischia, & Palmisano, 2003)**. Simultaneously, the thermal analyses of an appropriate fraction of the purging He flux, sampled few millimeters above the sample-crucible, were continuously withdrawn and analyzed. Electron impact mass spectra (70 eV) were recorded with frequency of 1 scan s^{-1} in the 1–400 amu range (ionization chamber temperature 200°C. A flux of a 5% H_2/N_2 mixture was also used to optimize the instrument sensibility in detecting the H_2 signal, due to its extreme low *m*/*z* value within the instrumental scanning range.

TG-MS instrument coupling were realized connecting the furnace of the thermobalance with the ionization chamber of the mass-spectrometer through an empty and deactivated-silica capillary-column (0.32 mm inter. diam.; 16 m length) enveloped in a thermostatted jacket heated at 250°C. Operative experiments showed that gaseous species usually transfer from the thermobalance furnace to the mass spectrometer in less than 40 s. MS-data are recorded as a continuous sequence of mass spectra. From these MS-data, the total ion current (TIC) and the *m*/*z* ion current (IC) were scanned in time. The integrated areas of the IC bands were used for a semi-quantitative evolution of the evolved gases and also for comparison to TG-MS measurements **(Campostrini, Ischia, & Palmisano, 2003)**.

7.4 Results and Discussion

7.4.1 TG-MS analysis

The thermal decomposition of the MgH_2 phase was analyzed taking into account different parameters: the onset and peak temperature of the DTA-band curve; the peak temperature of the DTG-band curve; the flex point of the TG-curve during the H-release event. Analogously, from MS-data the peak temperature of the TIC and other representative IC curves were considered. Temperatures of the onset and of the α=0.1 iso-conversion point were also processed in the case of IC *m*/*z*=2 ion current.

Figure 7.1 shows the TG-MS for (unmilled) MgH_2 tested at 10 °C/min heating rate. The TIC-curve clearly indicates the presence of three separate events, which yield two small broad bands at 86 and

312°C, and an intense net peak at 440°C. These peaks are attributed, respectively, to the evolution of H_2O, CO_2 and H_2, with corresponding m/z = 18, 44, and 2 (**see figure 7.1**).

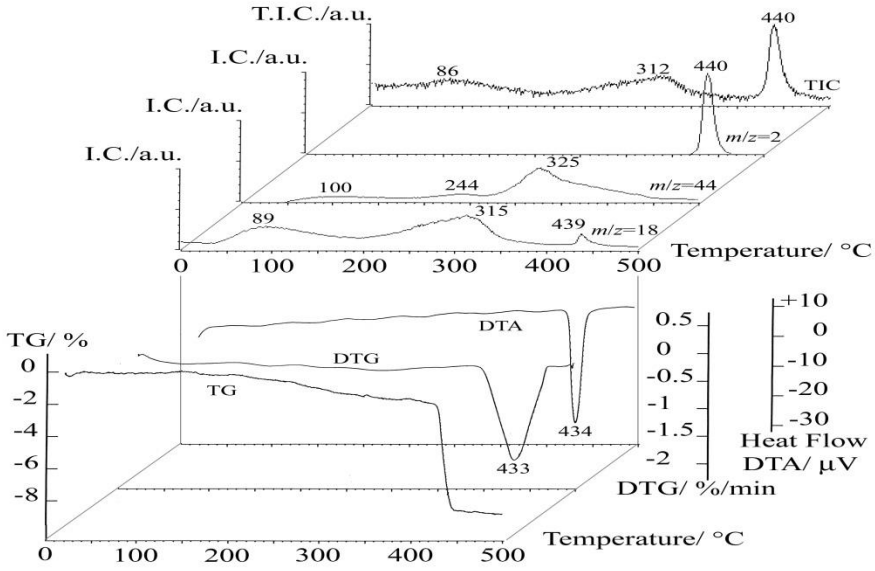

Figure 7.1 *TG-MS analysis of pure (unmilled) MgH_2 sample, carried out at 10°C/min heating rate*

Table 7.1 summarizes how the temperature values of the most representative points in all curves (onset-, peak-, flex-, α=0.1 fixed conversion-temperature) are detected shifting upward with the increase in the TG-MS heating rate. The reductive decomposition of pure MgH_2 to magnesium metal powders is the main detected event. As shown in **figure 7.1**, its maximum occurrence is revealed at 433°C, with a relative intensity of 7.0 wt%, when the heating rate is carried out at 10°C/min.

Table 7.1 *TG-MS analyses of pure (unmilled) MgH_2 sample. Temperatures of constant conversion degree (α) recorded in the various experiments at different heating rates (β)*

Heating rate of TG-MS analysis, β, (°C/min)			**10**	**13**	**16**	**19**	**22**
T	data	TG-curve, T_{flex}	433.2	438.5	442.3	447.8	449.8
e	from	DTG-curve, T_{peak}	433.0	438.4	449.7	455.3	457.7
m	TG-DTA	DTA-curve, T_{onset}	426.1	430.6	434.2	436.8	439.3
p	analyses	DTA-curve, T_{peak}	434.0	439.4	443.5	449.1	451.4
e	data	TIC-curve, 1st band, T_{peak}	86.5	101.8	113.6	120.1	132.4
r	from	TIC-curve, 2nd band, T_{peak}	311.9	324.4	327.7	338.2	344.7
a	MS	TIC-curve, 3rd band, T_{peak}	439.8	447.2	453.1	457.5	462.4
t	analysis						
u	**H_2 release**	IC-curve, m/z=2, T_{peak}	440.1	447.5	453.0	459.2	463.1
r		IC-curve, m/z=2, T_{onset}	418.2	425.0	430.2	433.4	438.0
e		IC-curve, m/z=2, $T_{\alpha=0.1}$	434.9	441.6	447.0	451.7	455.9
(°C)	**H_2O release**	IC-curve, m/z=18, 1st band, T_{peak}	89.0	100.8	112.0	123.5	132.0
		IC-curve, m/z=18, 2nd band, T_{peak}	315.0	322.4	328.0	334.4	338.8
		IC-curve, m/z=18, 3rd band, T_{peak}	438.7	445.9	451.2	455.6	460.5
	CO_2 release	IC-curve, m/z=44, 1st band, T_{peak}	100.0	113.1	124.8	133.0	140.8
		IC-curve, m/z=44, 2nd band, T_{peak}	243.7	249.6	253.6	256.5	259.6
		IC-curve, m/z=44, 3rd band, T_{peak}	325.0	332.8	339.2	344.9	349.8

Different model-free Flynn-Wall-Ozawa (type B-0), Kissinger-Akahira-Sunose (type B-2), and Starink (**type B-1.95 and 1.92**) methods were applied to determine an apparent activation energy (*E*) from the experimental data summarized in **Table 7.1**. **Tables 7.2** and **7.3** contain the activation energy values resulting from different thermal curves (TG, DTA, TIC and IC), using different transformed iso-conversion points.

Table 7.2 *Apparent activation energy values obtained, for pure (unmilled) MgH_2 sample, from* ***TG-MS*** *analysis using* ***Flynn-Wall-Ozawa*** *(type B-0),* ***Kissinger-Akahira-Sunose*** *(type B-2), and* ***Starink*** *(type B-1.95 and 1.92) equations*

Data from	$T_{isoconversion}$ point from	Method	R^2 *	Act. Energy kJ/mol
TG-DTA analysis	TG-curve, T_{flex}	B-0	0.991	185(10)
		B-2	0.9898	183(11)
		B-1.95	0.9898	183(11)
		B-1.92	0.9899	183(11)
	DTG-curve, T_{peak}	B-0	0.9708	117(12)
		B-2	0.9644	111(12)
		B-1.95	0.9646	111(12)
		B-1.92	0.9647	111(12)
	DTA-curve, T_{onset}	B-0	0.9992	236(4)
		B-2	0.9991	236(4)
		B-1.95	0.9991	237(4)
		B-1.92	0.9991	237(4)
	DTA-curve, T_{peak}	B-0	0.9931	177(8)
		B-2	0.9922	175(9)
		B-1.95	0.9922	175(9)
		B-1.92	0.9922	175(9)
MS analysis	TIC-curve, 1st band, T_{peak}	B-0	0.9929	21(1)
		B-2	0.9860	15(1)
		B-1.95	0.9863	15(1)
		B-1.92	0.9864	15(1)
	TIC-curve, 2nd band, T_{peak}	B-0	0.9785	69(6)
		B-2	0.9712	63(6)
		B-1.95	0.9714	63(6)
		B-1.92	0.9715	63(6)
	TIC-curve, 3rd band, T_{peak}	B-0	0.9992	146(3)
		B-2	0.9991	141(3)
		B-1.95	0.9991	141(3)
		B-1.92	0.9991	142(3)

* *R^2 factor refers to the goodness of fit*

Table 7.3 *Apparent activation energy values obtained, for pure (unmilled) MgH_2 sample, from **TG-MS** coupled measurements by using **MS-data** processed with **Flynn-Wall-Ozawa** (type B-0), **Kissinger-Akahira-Sunose** (type B-2), **Starink** (type B-1.95 and 1.92), and **Friedman** equations*

Data from	$T_{isoconversion}$ point from	Method	R^2 *	Act. Energy kJ/mol
MS analysis	IC *m*/*z*=18 curve, 1st band, T_{peak}	B-0	0.9976	20.9(4)
		B-2	0.9944	15(1)
		B-1.95	0.9946	16(1)
		B-1.92	0.9946	16(1)
	IC *m*/*z*=18 curve, 2nd band, T_{peak}	B-0	0.9978	94(3)
		B-2	0.9972	89(3)
		B-1.95	0.9972	89(3)
		B-1.92	0.9973	89(3)
	IC *m*/*z*=18 curve, 3rd band, T_{peak}	B-0	0.9988	152(3)
		B-2	0.9986	148(3)
		B-1.95	0.9986	148(3)
		B-1.92	0.9986	148(3)
	IC *m*/*z*=44 curve, 1st band, T_{peak}	B-0	0.9986	23.5(4)
		B-2	0.9979	18.0(4)
		B-1.95	0.9979	18.4(4)
		B-1.92	0.9979	18.4(4)
	IC *m*/*z*=44 curve, 2nd band, T_{peak}	B-0	0.9968	109(4)
		B-2	0.9963	106(4)
		B-1.95	0.9963	106(4)
		B-1.92	0.9963	107(4)
	IC *m*/*z*=44 curve, 3rd band, T_{peak}	B-0	0.9998	94(1)
		B-2	0.9997	88(1)
		B-1.95	0.9997	89(1)
		B-1.92	0.9997	89(1)
	IC *m*/*z*=2 curve, T_{peak}	B-0	0.9983	141(3)
		B-2	0.9979	136(4)
		B-1.95	0.9979	136(4)
		B-1.92	0.9979	136(4)
	IC *m*/*z*=2 curve, T_{onset}	B-0	0.9966	158(5)
		B-2	0.9960	154(5)
		B-1.95	0.9961	154(5)
		B-1.92	0.9961	155(5)
	IC *m*/*z*=2 curve, $T_{\alpha=0.1}$	B-0	0.9998	154(1)
		B-2	0.9998	149(1)
		B-1.95	0.9998	150(1)
		B-1.92	0.9998	150(1)

* *R^2 factor refers to the goodness of fit*

7.4.2 Elementary possible reactions of CO_2, H_2O and H_2 evolutions

- **H_2O evolutions events (*m/z = 18)*:**

Water released is described by the trend of *m*/*z*=18 curve: two distinct broad bands centered at 89 and 315°C, the second event being slightly more intense, followed by a very small peak at 439°C. The last event is constrained within a small and sharp peak, as compared with the first two, broader and more intense bands. It involves less than 4% of the total water amount detected in the whole MgH_2 thermal process, as calculated from the ratio of these three band areas of the IC *m*/*z*=18 curve. So, in the hypothesis of neglecting the small contribution of water evolution in the main TG decomposition, and considering the measured 7.0 wt% mass loss intensity due to molecular hydrogen only, this starting "pure MgH_2 sample" can be considered as made of 91 wt% of real MgH_2 chemical species.

The values of this kinetic parameter and the temperature intervals of these events suggest three different reasons for water formation, such as:

(i) The release of water molecule chemically absorbed by the solid MgH_2 structure:

$$MgH_{2(s)}\cdots OH_2 \xrightarrow{T\approx 100°C} MgH_{2(s)} + H_2O_{(g)} \qquad (\mathbf{7.16})$$

The activation energies of the first water release are close to the values typically attributed to hydrogen bridging bonds.

(ii) The evolution of water yielded by dehydration of magnesium hydroxide units (and of $Mg(OH)HCO_3$), which is supposed to constitute part of the "impurity counterpart" of this "pure-MgH_2 sample",

$$Mg(OH)_{2(s)} \xrightarrow{T\approx 300°C} MgO_{(s)} + H_2O_{(g)} \qquad (\mathbf{7.17})$$

Temperature interval and *E* values derived for the second H_2O-release are of the same order of magnitude of chemical processes due to condensation-reaction between metal-hydroxide groups in amorphous metal oxide solid matrices **(Campostrini, Sicurelli, Ischia, & Carturan, 2007) (Campostrini, Ischia, & Palmisano, 2004)**.

(iii) The side-reaction between magnesium oxide (formed in the above reaction or even present in the sample as further type of impurity) with the hydrogen evolved, at these temperatures, by the thermal reductive decomposition of MgH_2,

$$MgO_{(s)} + H_{2(g)} \xrightarrow{T\approx 440°C} Mg_{(s)} + H_2O_{(g)} \qquad (\mathbf{7.18})$$

- **CO_2 evolutions events (*m/z = 44)*:**

The evolution of carbon dioxide is also detected in three events marked by the *m*/*z*=44 curve: firstly two very small and broad bands centered at 100 and 244°C, then a main broad band at 325°C. Differently from water release, only the last CO_2 evolution is quantitatively relevant. Taking into account the area under the ion currents of the *m*/*z*=17+18 and *m*/*z*=28+44 curves, used to quantify respectively the H_2O and CO_2 releases, water amount seems five times (in molar) higher than the CO_2 counterpart. Therefore relative impurities in pure MgH_2, such as $Mg(OH)_2$ and $MgCO_3$, are possibly present and more specifically the $Mg(OH)_2$ phase, that has been already detected by a XRD quantitative analysis of the pristine MgH_2 (**see last chapter**). Starting from the idroxide phase, H_2O released around 300 °C can be described by the following reaction (**equation 7.19**):

$$Mg(OH)_{2(s)} \rightarrow MgO_{(s)} + H_2O_{(g)} \quad (\mathbf{7.19})$$

Similarly, $MgCO_3$ decomposition (nominally simplified in its stoichiometry as follows) can lead to carbon dioxide evolution around 330°C by the reaction:

$$MgCO_{3(s)} \rightarrow MgO_{(s)} + CO_{2(g)} \quad (\mathbf{7.20})$$

These impurities found in the pristine MgH_2 are a result of the high sensitivity of Mg to the moisture and oxygen presence, despite the analysis and storage process were carefully treated to avoid that. The possible reaction due to these impurities can be summarized as follows:

$$MgH_{2(s)} + O_{2(g)} \rightarrow MgO_{(s)} + H_2O_{(g)} \quad (\mathbf{7.21})$$

$$MgH_{2(s)} + 2\ H_2O_{(g)} \rightarrow Mg(OH)_{2(s)} + 2\ H_{2(g)} \quad (\mathbf{7.22})$$

$$MgO_{(s)} + CO_{2(g)} \rightarrow MgCO_{3(s)} \quad (\mathbf{7.23})$$

$$Mg(OH)_{2(s)} + CO_{2(g)} \rightarrow Mg(OH)HCO_{3(s)} \quad (\mathbf{7.24})$$

$$Mg(OH)_{2(s)} + CO_{2(g)} \rightarrow MgCO_{3(s)} + H_2O_{(g)} \quad (\mathbf{7.25})$$

- **H_2 evolutions event (*m/z = 2)*:**

During this thermogravimetric event molecular hydrogen is the main released species (**see equation 7.26**). In the literature data on E values for pure MgH_2 roughly fall in the range 156-206 kJ/mol **(Huot, Liang, Boily, Van Neste, & Schulz, 1999)** **(Gabis, Dobrotvorskiy, Evard, & Voyt, 2011)** **(Zaranski & Czujko, 2011)**

$$MgH_{2(s)} \rightarrow Mg_{(s)} + H_{2(g)} \quad (\mathbf{7.26})$$

According to results of **table 7.2**, the E values of hydrogen desorption obtained from the TG, DTA_{onsent} and DTA_{peak} signals are higher than those given by MS for hydrogen release. This difference could be related to the fact that TG and DTA analyses are related to the mass loss in the investigated sample as a function of temperature. In other words, they cannot differentiate whether the mass loss is due to hydrogen only or to other gases as well, so the corresponding activation energy gathers implicitly other activation energies for all evolved gases (i.e. H_2O and CO_2) besides hydrogen. Differently, from MS one can directly separate the hydrogen signal from that of other gases, even if evolving at the same temperature, as each species has its corresponding mass signal (i.e. m/z ratio). Therefore MS is more reliable than thermal analysis techniques to measure the activation energy in hydrogen storage processes.

7.5 Conclusions

- TG-MS measurements are a powerful tool for the identification of the single chemical species, even when simultaneously released during the thermal evolution of MgH_2. Three gases evolved, H_2O, CO_2 and H_2, even if H_2 was the main spacies giving the most intense event. Hydrogen release is observed around 430°C, with a simultaneous evolition of other species (i.e. H_2O and CO_2), so that MS is necessary to separate each gas contribution, based on their different mass ratios.
- Temperatures corresponding to several iso-conversion points of the TG, DTG, DTA-curves and of the TIC or IC curves, were used for activation energy analysis corresponding to different gases evolutions. It was found that regardless of the method used, the activation energy values are similar, with a small error bar when the same iso-conversion point is chosen.
- The activation energy of hydrogen desorption obtained from TG and DTA is higher than the corresponding one obtained from the MS signal; main difficulty with TG and DTA methods is separating the influence of each gas evolved at the same temperature, which is quite straightforward when MS is used.

References

Abdellatief, M., Abele, M., Leoni, M., & Scardi, P. (2013). Solid State Nuclear Magnetic Resonance and X-ray Diffraction Line Profile Analysis of heavily deformed fluorite. *Thin Solid Films, 530*, 44-48.

Amatucci, G. G., & Pereira, N. (2007). *J. Fluor. Chem., 128*, 243.

Aurora, T. S., Day, S. M., & Pederson, D. O. (1994). Dilatometric and thermo-optic properties of alkaline earth and cadmium fluorides between 300 and 1300 K. *Journal of Applied Physics, 76*(4), 2122.

Baldan, A. (2002). Progress in Ostwald Ripening Theories and Their Applications to Nickel-base Superalloys, Part I: Ostwald Ripening Theories. *J. Mater. Sci., 37*, 2171–2202.

Barkhordarian, G., Klassen, T., & Bomann, R. (2003). Fast hydrogen sorption kinetics of nanocrystalline Mg using Nb2O5 as catalyst. *Scripta Mater., 49*, 213-217.

Barkhordarian, G., Klassen, T., & Bormann, R. (2004). Effects of Nb2O5 content on hydrogen reaction kinetics of Mg. *J. Alloys Compd. , 364*, 242-246.

Bastide, J. P., Bonnetot, B., Letoffe, J., & Claudy, P. (1980). Polymorphisme de l'hydrure de magnesium sous haute pression. *Mat. Res. Bull., 15*, 1215-1224.

Berlouis, L. E., Cabrera, E., Hall-Barientos, E., Hall, P. J., Dodd, S. B., & Morris, S. (2001). Thermal analysis investigation of hydriding properties of nanocrystalline Mg–Ni– and Mg–Fe–based alloys prepared by high-energy ball milling. *J. Mater. Res., 16*, 45–57.

Berube, V., Radtke, G., Dresselhaus, M., & Chen, G. (2007). Size effects on the hydrogen storage properties of nanostructured metal hydrides: a review. *Int. J. Energy Res., 31*, 637-663.

Birringer, R. a. (1988). *Advance in Materials Science, Encyclopedia of Materials Science and Engineering*. (R. W. Cahn, A cura di) Oxford: Pergamon Press.

Bobylev, S. V., Mukherjee, A. K., & Ovid'ko, I. A. (2009). TRANSITION FROM PLASTIC SHEAR INTO ROTATION DEFORMATION MODE IN NANOCRYSTALLINE METALS AND CERAMICS. *Rev. Adv. Mater. Sci. , 19*, 103-113.

Buschow, K. H., Bouten, P. C., & Miedema, A. R. (1982). Hydrides formed from intermetallic compounds of two transition metals: a special class of ternary alloys. *Rep. Prog. Phys. , 45*, 937-1039.

Caglioti, G., Paoletti, A., & Ricci, F. P. (1958). Choice of collimator for a crystal spectrometer for neutron diffraction. *Nucl. Instrum. Methods, 3*, 223-228.

Caglioti, G., Paoletti, A., & Ricci, F. P. (1958). Nucl. Instrum. and Meth. . *3*, 223.

Campostrini, R., Ischia, M., & Palmisano, L. (2003). Pyrolysis study of sol-gel derived TiO2 powders Part I TiO2-anatase prepared by reacting titanium(IV) isopropoxide with formic acid. *J Therm Anal Cal., 71*, 997-1009.

Campostrini, R., Ischia, M., & Palmisano, L. (2004). Pyrolysis study of sol-gel derived TiO2 powders Part VI TiO2-anatase prepared by hydrolysing titanium(IV) isopropoxide without chelating agents. *J. Therm. Anal. Cal. , 75*, 25-34.

Campostrini, R., Sicurelli, A., Ischia, M., & Carturan, G. (2007). Pyrolysis study of a hydride-sol-gel silica Part II Kinetic aspects. *J. Therm. Anal. Cal. , 90*, 179-184.

Campostrini, R., Sicurelli, A., Ischia, M., & Carturan, G. (2007). Pyrolysis study of a hydride–sol–gel silica. Part II. Kinetic aspects. *J. Therm. Anal. Calorim., 90*, 179-184.

Caravaca, M. A., Casali, R. A., & Ponce, C. A. (2011). Macroscopic elastic anisotropy in tough ceramics from the single crystal elastic behaviour. *Procedia engineering , 10*, 2158-2163.

Cervellino, A., Giannini, C., & Guagliardi, A. (2003). *J. Appl. Cryst., 36*(5), 1148-1158.

Cervellino, A., Giannini, C., & Guagliardi, A. (2006). *J. Comp. Chem., 27*(9), 995-1008.

Chandra, S. (1981). Superionic Soilds Principles and Applications. North Holland, Amsterdam.

Cline, J. P., Deslattes, R. D., Staudenmann, J. L., Kessler, E. G., Hudson, L. T., Henins, A., et al. (2000). *Certificate SRM660a.* NIST, Gaithersburg.

De Giudici, G., Biddau, R., D'Incau, M., Leoni, M., & Scardi, P. (2005). *Geochim. Cosmochim. Acta. , 69*(16), 4073-4083.

Debye, P. (1915). *Nachr. Ges. Wiss. Goettingen, Math.-Phys. Kl.*, 70-76.

Dong, S., Zou, G., & Yang, H. (2001). Thermal characteristic of ultrafine-grained aluminum produced by wire electrical explosion. *Scripta Materialia, 44*, 17-23.

Dufour, J., & Huot, J. (2007). Rapid activation enhanced hydrogen sorption kinetics and air resistance in laminated Mg–Pd 2.5 at.%. *J. Alloys Compd., 439*, 5-7.

Durá, O. J., López de la Torre, M. A., Vázquez, L., Chaboy, J., Boada, R., Rivera-Calzada, A., et al. (2010). Ionic conductivity of nanocrystalline yttria-stabilized zirconia: Grain boundary and size effects. *Phys. Rev. B, 81*, 184301-184309.

Eckert, H. (1996). *Current Opin. in Sol. St. and Mater Sci., 1*, 465.

Eckert, H. (2008). Solid state nuclear magnetic resonance:a versatile tool in solid state chemistry and materials science. *Bunsen-Magazin*, 10.

Eckert, J., Holzer, J. C., Krill III, C. E., & Johnson, W. L. (1992). *J. Mater. Res., 7*, 1751.

Every, A. G., & McCurdy, A. K. (1992). *Numerical Data and Functional Relationships in Science and Technology* (Vol. 29). (L. Börnstein, A cura di) Berlin: Springer-Verlag.

Fátay, D., Spassov, T., Delchev, P., Ribárik, G., & Révész, Á. (2007). Microstructural development in nanocrystalline MgH2 during H-absorption/desorption cycling. *Int. J. Hydrogen Energy , 32*, 2914-2919.

Fiala, J., & Snyder, R. L. (1999). *Defect and microstructural analysis by diffraction.* (R. L. Snyder, J. Fiala, & H. J. Bunge, A cura di) Oxford University Press, New York.

Fukabori, A., An, L., Ito, A., Chani, V., Kamada, K., Yoshikawa, A., et al. (2012). Correlation between crystal grain sizes of transparent ceramics and scintillation light yields Ceramics International. *38*(3), 2119-2123.

Fukai, Y. (1993). *The metal–hydrogen system, basic bulk properties.* Berlin: Springer series in materials science.

Fukunaga, T., Itoh, K., Orimo, S., & Fujii, H. (2002). *Physica B: Condensed Matter, 311*(1-2), 95-101.

Gabis, I., Dobrotvorskiy, M., Evard, E., & Voyt, A. (2011). Kinetics of dehydrogenation of MgH2 and AlH3. *J. Alloys Compd., 509*, 671-674.

Garcia, J. M., Leoni, M., & Scardi, P. (2009). Act. Cryst. A. *65*, 109.

Gelisio, L., Azanza Ricardo, C., & Leoni, M. S. (2010). *J. Appl. Cryst., 43*(3), 647-653.

Giudici, G., Biddau, R., D'Incau, M., Leoni, M., & Scardi, P. (2005). *Geochimic. et Cosmochim. Acta, 69*, 4073.

Gleiter, H. (1989). *Prog. Mater. Sci., 33*, 223.

Günther, B., Kumpmann, A., & Kunze, H.-D. (1992). Secondary recrystallization effects in nanostructured elemental metals. *Scripta Metall. Mater., 27*, 833-838.

Guo, A. X., Shang, C., & Zinsou, K. F. (2008). Materials challenges for hydrogen storage. *J. Eur. Ceram. Soc., 28*, 1467-1473.

Guoa, Z. X., Shang, C., & Aguey-Zinsou, K. F. (2008). Materials challenges for hydrogen storage. *Journal of the European Ceramic Society , 28*, 1467-1473.

Hanada, N., Ichikawa, T., & Fujii, H. (2005). Catalytic Effect of Nanoparticle 3d-Transition Metals on Hydrogen Storage Properties in Magnesium Hydride MgH2 Prepared by Mechanical Milling. *J. Phys. Chem. B, 109*, 7188-7194.

Hanada, N., Ichikawa, T., Orimo, S. I., & Fujii, H. (2004). Nanocrystalline titanium-type metal hydride electrodes prepared by mechanical alloying. *J. Alloys Compd., 336*, 269-273.

Heitjans, P., & Indris, S. (2003). *J. Phys. Condens. Mat., 15*, 1257.

Heitjans, P., & Indris, S. (2003). Diffusion and ionic conduction in nanocrystalline ceramics. *J. Phys.: Condens. Matter , 15*, 1257-1289.

Heitjans, P., & Wilkening, M. (2002). *Mrs Bulletin, 34*, 915.

Hu, J., Cai, W., Cuncheng, L. C., Gan, Y., & Chen, L. (2005). In situ x-ray diffraction study of the thermal expansion of silver nanoparticles in ambient air and vacuum. *APPLIED PHYSICS LETTERS, 86*, 151915-151917.

Hull, D., & Bacon, D. J. (1984). *Introduction to dislocation.* Pergnmon Press, Oxford UK.

Huot, J., Liang, G., Boily, S., Van Neste, A., & Schulz, R. (1999). Structural study and hydrogen sorption kinetics of ball-milled magnesium hydride. *J. Alloys Compd., 293*, 495-500.

Imamura, H., Tanaka, K., Kitazawa, I., Sumi, T., Sakata, Y., Nakayama, N., et al. (2009). Hydrogen storage properties of nanocrystalline MgH2 and MgH2/Sn nanocomposite synthesized by ball milling. *J. Alloys Compd. , 484*, 939-942.

Indris, S., & Heitjans, P. (2002). *J. Non Cryst. Sol., 555*, 307.

Jain, I., Lal, C., & Jain, A. (2010). Hydrogen storage in Mg: A most promising material. *Int. J. Hydrogen Energy , 35*, 5133-5144.

Jain, P., Kim, S., Youngman, R. E., & Sen, S. (2010). Direct observation of defect dynamics in nanocrystalline CaF2: Results from 19F MAS NMR spectroscopy. *J. Phys. Chem. Lett., 1*, 1126-1129.

James, T. R., Scates, R., & Martyn, V. T. (2003). X-ray diffraction study of nickel oxide reduction by hydrogen. *Applied Catalysis A, 246*, 137-150.

Janek, J., Martin, M., & Becker, K. D. (2009). Physical chemistry of solids--the science behind materials engineering. *Physical chemistry chemical physics, 11*(17), 3071-3081.

Jin, S., Shim, J., Cho, Y. W., & Yi, K. (2007). Dehydrogenation and hydrogenation characteristics of MgH2 with transition metal fluorides. *J. Power Sources, 172*, 859-862.

Jr, H. L., JF, H., & Wolf W, S. P. (2007). Ab Initio thermodynamic and elastic properties of alkaline-earth metals and their hydrides. *Phys Rev B , 76*, 014121-014138.

Jung, K. S., & Lee, K. (2006). Magnesium-based nano-composite materials for hydrogen storage. *J. Alloys Compd., 424*, 294-298.

Kandhasamy, S., Nallathamby, K., & Minakshi, M. (2012). *Progress in Solid State Chemistry, 40*(1-2), 1-5.

Khawam, A., & Flanagan, D. R. (2006). Basics and Applications of Solid-State Kinetics : A Pharmaceutical Perspective. *95*(3), 472-498.

Kirchner, H. O. (1971). Coarsening of Grain-Boundary Precipitates. *Metall. Trans*, 2861–2864.

Kirsch, B. L., Richman, E. K., Riley, A. E., & Tolbert, S. H. (2004). In-Situ X-ray Diffraction Study of the Crystallization Kinetics of Mesoporous Titania Films. *J. Phys. Chem. B, 108*, 12698-12706.

Klug, H. P., & Alexander, L. E. (1974). *X-ray Diffraction Procedures for Polycrystalline and Amorphous Materials.* New York NY: Wiley.

Koch, C. (1997). Synthesis of nanostructured materials by mechanical milling: Problems and opportunities. *Nanostructured Materials, 9*, 13-22.

Krill III, C. E., Helfen, L., Michels, D., Natter, H., Fitch, A., Masson, O., et al. (2001). Size-Dependent Grain-Growth Kinetics Observed in Nanocrystalline Fe. *Phys. Rev. Lett., 86*, 842–845.

Lausi, A., Busetto, E., Leoni, M., & Scardi, P. (2006). MCX diffraction beamline at ELETTRA . *Synchrotron Radiation in Natural Science, 5*, 1.

Leoni, M., & Scardi, P. (2004). *J. Appl. Cryst., 37*, 629-634.

Leoni, M., Confente, T., & Scardi, P. (2006). *Z. Kristallogr, Suppl., 23*, 249-254.

Leoni, M., De Giudici, G., Biddau, R., D'Incau, M., & Scardi, P. (2006). *Z. Kristallogr Suppl., 23*, 111-116.

Leoni, M., Martinez-Garcia, J., & Scardi, P. (2007). Dislocation effects in powder diffraction. *J. Appl. Cryst., 40*, 719-724.

Leoni, M., Scardi, P., D'incau, M., & Luciani, G. (2012). Annealing Behavior of a Nanostructured Fe1.5Mo Alloy. *Metallurgical and Materials Transactions A, 43*, 1522-1527.

Maehlen, J. P., Yartys, V. A., Fichtner, M., Frommen, C., Bulychev, B. M., Pattison, P., et al. (2007). Thermal decomposition of AlH3 studied by in situ synchrotron X-ray diffraction and thermal desorption spectroscopy. *Journal of Alloys and Compounds, 446–447*, 280-289.

Majumdar, S., Huhtinen, H., Majumdar, H. S., & Paturi, P. (2012). *Journal of Alloys and Compounds, 512*(1), 332-339.

Malka, I. E., Czujko, T., & Bystrzycki, J. (2010). Hydrogen sorption kinetics of MgH2 catalyzed with titanium compounds. *Int. J. Hydrogen Energy, 35*, 3046-3050.

Malkaa, I. E., Czujko, T., & Bystrzycki, J. (2010). Catalytic effect of halide additives ball milled with magnesium hydride. *Int. J. Hydrogen Energy, 35*, 1706-1712.

Martin, M. (2003). Grain boundary ionic conductivity of yttrium stabilized zirconia as a function of silica content and grain size. *Solid State Ionics, 161*(1-2), 67-79.

Mileva, A., Wilsonb, M., Kamali Kannangaraa, G., & Trana, N. (2008). X-ray diffraction line profile analysis of nanocrystalline graphite. *Materials Chemistry and Physics, 111*, 346-350.

Mittemeijer, E. J., & Welzel, U. (2008). The "state of the art" of the diffraction analysis of crystallite size and lattice strain. *Z. Kristallogr., 223*, 552–560.

Moldovan, D., Wolf, D., & Phillpot, S. R. (2002). *Acta Mater., 50*, 3397.

Moldovan, D., Yamakov, V., Wolf, D., & Phillpot, S. R. (2002). *Phys. Rev. Lett., 89*, 206101.

Molinari, a., Libardi, S., Leoni, M., & Scardi, P. (2010). Role of lattice strain on thermal stability of a nanocrystalline FeMo alloy. *Acta Materialia, 58*(3), 963-966.

Morcrette, M., Chabre, Y., Vaughan, G., Amatucci, G., Leriche, J. B., Patoux, S., et al. (2002). In situ X-ray diffraction techniques as a powerful tool to study battery electrode materials. *Electrochimica Acta , 47*, 3137.

Mukherjee, A. K. (2002). Mater. Sci. Eng. A. *322*, 1-22.

Muñoz, A., Domingguez-Rodriguez, A., & Kasstaing, J. (1994). Slip systems and plastic anisotropy in CaF2. *J. Mat. Sci.*(29), 6207–6211.

Nayeb-Hashemi, A. A. (1988). Phase diagrams of binary magnesium alloys. In *Clark, J. B.* Ohio: ASM International, Metals Park.

Niklasson, G. A., & Granqvist, C. G. (2007). Electrochromics for smart windows: thin films of tungsten oxide and nickel oxide, and devices based on these. *J. Mater. Chem.* , 127-156.

Oelerich, W., Klassen, T., & Bormann, R. (2001). Metal oxides as catalysts for improved hydrogen sorption in nanocrystalline materials. *J. Alloys Compd., 315*, 273-242.

Omolfajr, N., Nasser, S., & Mahmood, R. K. (2011). Synthesis and Characterization of CaF2 NPs with Co-precipitation and Hydrothermal Method. *J. Nanomed. Nanotechnol., 2*(5), 2-5.

Patah, A., Takasaki, A., & Szmyd, J. S. (2009). Influence of multiple oxide (Cr2O3/Nb2O5) addition on the sorption kinetics of MgH2. *Int. J. Hydrogen Energy , 34*, 3032-3037.

Peng, X., Wickham, J., & Alivisatos, A. P. (1998). Kinetics of II–VI and III– V Colloidal Semiconductor Nanocrystal Growth: ''Focusing'' of Size Distributions. *J. Am. Chem. Soc., 120*, 5343-5344.

Peterson, N. L. (1986). Diffusion mechanisms and structural effects in grain boundaries. *Journal of Vacuum Science & Technology A, 4*(6), 3066-3070.

Puin, W., Rodewald, S., Ramlau, R., Heitjans, P., & Maier, J. (2000). Local and overall ionic conductivity in nanocrystalline CaF2. *Solid State Ionics, 131*, 159-164.

Puina, W., Ramlau, R., Heitjans, P., & Maier, J. (2000). Local and overall ionic conductivity in nanocrystalline CaF2. *Solid state ionics, 131*, 159-164.

Rabbani, S. R., & Edmonds, D. T. (1994). Nuclear spin-lattice relaxation-time reduction in small particles. *Phys. Rev. B, 50*, 6184-6188.

Ribeiro, C., Lee, E. J., Giraldi, T. R., Aguiar, R., Longo, E., & Leite, E. R. (2005). In situ oriented crystal growth in a ceramic nanostructured system. *JOURNAL OF APPLIED PHYSICS 97, 024313 (2005), 97*, 24313.

Riello, P., Lausi, A., Macleod, J., Plaisier, Z. J., & Fornasiero, P. (2013). In situ reaction furnace for real-time XRD studies. *J. Synchrotron Rad., 20*, 194-196.

Rojas, P., Lavernia, E. J., Sun, F., & Zu, A. (2006). Thermal Stability and Recrystallization of Nanocrystalline Ti Produced by Cryogenic Milling. *Metallurgical and Materials Transactions A, 37*, 2069-2078.

Ruprecht, B., Wilkening, M., Feldhoff, A., Steuernagel, S., & Heitjans, P. (2009). *Phys. Chem. Chem. Phys., 11*, 3071.

Ruprecht, B., Wilkening, M., Steuernagel, S., & Heitjans, P. (2008). Anion diffusivity in highly conductive nanocrystalline BaF2: CaF2 composites prepared by high energy ball milling. *J. Mater. Chem., 18*, 5412-5416.

Sakintuna, B., Darkrim, F. L., & Hirscher, M. (2007). *International Journal of Hydrogen Energy, 32*(9), 1121-1140.

Sakintuna, B., Lamari-Darkrim, F., & Hirscher, M. (2007). Metal hydride materials for solid hydrogen storage: A review. *Int. J. Hydrogen Energy, 32*, 1121-1140.

Scardi, P. (2008). Microstructural properties: lattice defects and domain size effects. In R. Dinnebier, & S. (. Billinge, *Powder Diffraction: Theory and Practice* (p. 376-413). Cambridge (UK): The Royal Society of Chemistry.

Scardi, P. (s.d.). in Powder Diffraction: Theory and Practice. In R. E. Dinnebier, & S. J. Billinge (A cura di). Cambridge: The Royal Society of Chemistry.

Scardi, P., & Leoni, M. (2002). *Acta Cryst. A, 58*, 190-200.

Scardi, P., & Leoni, M. (2004). In E. J. Mittemeijer, & P. Scardi (A cura di), *Diffraction Analysis of the Microstructure of Materials* (p. 51). Springer-Verlag Berlin Heidelberg, Berlin.

Scardi, P., & Leoni, M. (2004). Whole Powder Pattern Modeling: theory and applications. In E. J. Mittemeijer, & P. Scardi (A cura di). Springer Verlag.

Scardi, P., & Leoni, M. (2006). Line profile analysis: pattern modelling versus profile fitting. *J. Appl. Cryst., 39*, 24-31.

Scardi, P., & Leoni, M. (2006). Advances in Line Profile Analysis for the Study of Nanocrystalline Systems. *ECS TRANSACTIONS, 3*, 125-132.

Scardi, P., & Leoni, M. (2006). Line profile analysis: pattern modelling versus profile fitting. *JOURNAL OF APPLIED CRYSTALLOGRAPHY, 39*, 24-31.

Scardi, P., D'incau, M., Leoni, M., & Fais, A. (2009). Dislocation Configurations in Nanocrystalline FeMo Sintered Components. *Metallurgical and Materials Transactions A, 41*(5), 1196-1201.

Scardi, P., Dong, Y. M., & Leoni, M. (2001). Line profile analysis in Rietveld method and Whole Powder Pattern Fitting. *Mat. Sci. Forum, 132*, 378-381.

Scardi, P., Leoni, M., & Dong, Y. H. (2000). Whole diffraction pattern fitting of polycrystalline ffc materials based on microstrucure. *Eur. Phys. J. B, 18*, 23-30.

Scardi, P., Leoni, M., Lamas, D. G., & Cabanillas, E. D. (2005). Grain size distribution of nanocrystalline systems. *POWDER DIFFRACTION, 20*, 353-358.

Scardi, P., Ortolani, M., & Leoni, M. (2010). WPPM: microstructural analysis beyond the Rietveld method. *Mater. Sci. Forum, 651*, 155-171.

Scarlett, N. V., Rowles, M. R., & Wallwork, K. S. (2001). Sample-displacement correction for whole-pattern profile fitting of powder diffraction data collected in capillary geometry. *J. Appl. Cryst. , 44*, 60-64.

Schichtel, N., Korte, C., Hesse, D., Zakharov, N., Butz, B., Gerthsen, D., et al. (2010). On the influence of strain on ion transport: microstructure and ionic conductivity of nanoscale YSZ|Sc2O3 multilayers. *Physical chemistry chemical physics, 12*(43), 14596–14608.

Scholz, G., Dorfel, I., Heidemann, D., Feist, M., & Stosser, R. (2006). Nanocrystalline CaF2 particles obtained by high-energy ball milling. *J. Solid State Chem., 179*, 1119-1128.

Schuler, B. J., Aurora, T. S., Pederson, D., & Day, S. M. (1995). THERMAL EXPANSION DATA FOR LEAD FLUORIDE. *Mat. Res. Soc. Symp. Proc.*, 325-330.

Shen, P., & Lee, W. H. (2001). *Nano Lett., 1*, 707.

Siegel, R. W., Trigg, G. L., Immergut, E. H., & Vera, E. S. (1994). *Nanophase Materials* (Vol. 11). (W. Greulich, A cura di) New York.

Smith, K., & Burum, D. P. (1989). Application of fluorine-19 cramps to the analysis of calcium fluoride/fluoroapatite mixtures. *J. Magn. Reson., 84*, 85-94.

Snyder, R. L., Fiala, J., & Bunge, H. J. (1999). *Defect and Microstructure Analysis by Diffraction.* Oxford, United Kingdom: Oxford University Press.

Starink, M. J. (2003). The determination of activation Energy from linear heating rate experiments: a comparison of the accuracy of isoconversion methods. *Thermochim Acta. , 404*, 163-179.

Starink, M. J. (2007). Activation energy determination for linear heating experiments: deviations due to neglecting the low temperature end of the temperature integral. *J. Mater. Sci., 42*, 483-489.

Sumino, K. (2000). *Materials Science and Engineering B, 72*(2-3), 67-72.

Suranarayana, C. (2001). *Progr. Mater. Sci., 46*, 1-184.

Tong, H. Y., Wang, J. T., Ding, B. Z., Jiang, H. G., & Lu, K. (1992). *J. Non-Cryst. Solids, 150*, 444.

Ungár, T., Dragomir, I., Révész, Á., & Borbély, A. (1999). *J. Appl. Cryst., 32*, 992.

van Kranendonk, J. (1954). Theory of quadrupolar nuclear spin-lattice relaxation. *Physica, 20 (10)*, 781-800.

Varin, R. A., Czujko, T., & Wronski, Z. (2006). Particle size, grain size and γ-MgH2 effects on the desorption properties of nanocrystalline commercial magnesium hydride (MgH2) processed by controlled mechanical milling. *Nanotechnol. , 17*, 3856-3865.

Varin, R. A., Jang, M., Czujko, T., & Wronski, Z. S. (2010). The effect of ball milling under hydrogen and argon on the desorption properties of MgH2 covered with a layer of Mg(OH)2. *J. Alloys Compd., 493*, 29-32.

Vives, S., Gaffet, E., & Meunier, C. (2004). *Materials Science and Engineering, A366*.

Vogel, W., Rosner, B., & Tesche, B. (1993). *J.Phys. Chem., 97*(45), 11611-11616.

Wagner, C. (1961). Theory of Precipitate Change by Redissolution. *Z. Elektrochem, 65*, 581-591.

Wang, F., Fan, X., Pi, D., & Wang, M. (2005). Synthesis and luminescence behavior of Eu3+ -doped CaF2 nano particles. *Solid State Commun. , 133*, 775-779.

Watanabe, H., Yamada, N., & Okaji, M. (2004). Linear Thermal Expansion Coefficient of Silicon from 293 to 1000 K. *International Journal of Thermophysics, 25*.

Wilkening, M., Indris, S., & Heitjans, P. (2003). Heterogeneous lithium diffusion in nanocrystalline Li2O:Al2O3 composites. *Phys. Chem. Chem. Phys., 5*, 2225-2231.

Wilkens, M. (1970). Fundamental Aspects of Dislocation Theory. In J. A. Simmons (A cura di), *Fundamental Aspects of Dislocation Theory* (Vol. 2, p. 1195). Gaithersburg.

Ying, J. Y., & Sun, T. (1997). *J. Electroceram., 1*, 219.

Young, R. (A cura di). (1993). *The Rietveld method.* New York: TNTERNATJONAL UNION OF CRYSTALLOGRAPHY- OXFORD UNIVERSITY PRESS.

Zaluska, A., Zaluski, L., & Ström-Olsen, J. (1999). Nanocrystalline magnesium for hydrogen storage. *J. Alloys Compd. , 228*, 217-225.

Zaranski, Z., & Czujko, T. (2011). The influence of ball milling process on hydrogenation properties of MgH2–FeTiHx composites. *J. Alloys Compd. , 509*, 608-611.

Zhang, H., & Banfield, J. F. (1999). New Kinetic Model for the Nanocrystalline Anatase-to-rutile Transformation Revealing Rate Dependence on Number of Particles. *Am. Mineral., 84*, 528-535.

Zhang, J., Huang, F., & Lin, Z. (2010). Progress of nanocrystalline growth kinetics based on oriented attachment. *Nanoscale, 2*(1), 18-34.

Zhao, Y. H., & Lu, K. (1997). *Phys. Rev., B56*, 14330.

Zhao, Y., Sheng, H., & Lu, K. (2001). Microstructure evolution and thermal properties in nanocrystalline Fe during mechanical attrition. *Acta. mater. , 49*, 365-375.

Zheng, S., Fang, F., Zhang, J., Sun, L., He, B., Wei, S., et al. (2007). Study of the Correlation between the Stability of Mg-Based Hydride and the Ti-Containing Agent. *J. Phys. Chem. C., 111*, 14021-14025.

Scientific production

1. **" Solid state nuclear magnetic resonance and x-ray diffraction line profile analysis of heavily deformed fluorite"**
   M. Abdellatief, M. Abele, M. Leoni, P. Scardi
   Thin Solid Films, Vol. 530 (2013), PP. 44-48
   http://dx.doi.org/10.1016/j.tsf.2012.09.020

2. **"Combined XRD and solid state ^{19}F MAS NMR analysis of defects in nanocrystalline fluorite"**
   Mahmoud Abdellatief, Matthias Abele, Matteo Leoni, Paolo Scardi
   Journal of Applied Crystallography (2013)-Submitted

3. **" Effects of SnO_2 on hydrogen desorption of MgH_2"**
   M. Abdellatief, M. Abele, M. Leoni, P. Scardi
   International Journal of Hydrogen Energy Vol. 38, Issue 11, (2013), PP. 4664-4669
   http://dx.doi.org/10.1016/j.ijhydene.2013.02.016

4. **"Influence of lattice defects on the grain growth kinetics of nanocrystalline fluorite"**
   M. Abdellatief, A. Lausi, J.R. Plaisier and P. Scardi
   Metallurgical and Materials Transactions A (2013) –In press
   DOI: 10.1007/s11661-013-1786-8

5. **"Activation Energy in the Thermal Decomposition of Magnesium Hydride Powders by TG-MS Coupled Measurements"**
   R. Campostrini, M. Abdellatief, M. Leoni & P. Scardi
   Journal of Thermal Analysis, (2013)- Submitted

6. **"Application of ^{19}F techniques in Solid-State NMR" – "In memoriam of Prof. Dr. Klaus Müller"** *M. Abele, M. Abdellatief, M. Leoni and P. Scardi*

   XL National Congress on Magnetic Resonance, Parma (I) 26-28 September 2011

Conference Participations

- **"8th European Conference on Residual Stresses (ECRS8)"**

Riva del Garda- Trento (Italy) – 26.06.2010

- **"Size Strain VI – Diffraction Analysis of the Microstructure of Materials"**

Presqu'Ile de Giens, Hyères (France) – 17.10.2011

Poster: *"*Solid state nuclear magnetic resonance and x-ray diffraction line profile analysis of heavily deformed fluorite*"*

- **"Trento Innovation Conferences in Materials Engineering (TICME)"**

Trento (Italy) – 12.12.2011

Poster: "Effects of SnO_2 on hydrogen desorption of MgH_2"